

## Do the Earth, Jupiter and Mercury cause the sunspot cycles?

Lauri Jetsu <sup>1</sup>••

© The author(s) •••

**Abstract** The mainstream dynamo models predict that the sunspot cycle is stochastic. The official Solar Cycle Prediction Panel forecasts only the ongoing sunspot cycle because any forecast beyond one cycle is considered impossible. We analyse the sunspot data using the Discrete Chi-square Method (DCM). This method can detect many periodic signals superimposed on an arbitrary trend. The DCM detects the extremely significant 10, 11, and 11.86 years signals. Our Discrete Fourier Transform (DFT) cross-check confirms that these signals are certainly real. We connect the detected signals to the Earth and Jupiter. Our deterministic DCM model predictions are longer and more accurate than the official Solar Cycle Prediction Panel forecast. The solar and planetary magnetic fields interact directly during the Flux Transfer Events (FTEs). We describe how these FTEs may cause “toroidal magnetic loops” in the Sun. If some physical mechanism amplifies the magnetic fields in these “toroidal magnetic loops”, their accumulative effect may weaken the poloidal global solar dipole field, until it flips. This would give a relatively simple explanation for the sunspot cycle, the Hale’s law, the sunspot pairs, the solar differential rotation and many other phenomena observed in the Sun. There are, however, three major astrophysical uncertainties. Can Cranmer and Saar (2007, Equation 2) estimate be applied to the FTEs? Can some FTE magnetic flux ropes transform into “toroidal magnetic loops”? Can some physical mechanism amplify the “toroidal magnetic loops”?

**Keywords:** Solar cycle, Observations - Sunspots, Statistics - Magnetic fields, Interplanetary

### 1. Introduction

Schwabe (1844) discovered the 10 years cycle in the number of sunspots. Wolf (1852) revised the cycle period to 11.1 years. This period is not constant but varies between 8 and 17 years (Lassen and Friis-Christensen, 1995). The amplitude of the sunspot number modulation follows a cycle of about 80 years (Gleissberg, 1945). All solar cycles have not been discovered from the sunspots, like the  $P_{\text{Rieger}} = 154$  days Rieger cycle discovered from the solar flares (Rieger et al., 1984) and the 205 years Suess-de Vries cycle discovered from the terrestrial radiocarbon  $^{14}\text{C}$  record (Wagner et al., 2001). These observations indicate that the sunspot data are multiperiodic. Multiple periods have been detected in the sunspot data with different time series analysis methods (Ohtomo et al., 1994; Zhu and Jia, 2018; Jayalekshmi, Pant, and Prince, 2022). There is no “phase-lock” in the observed sunspot cycle minimum and the maximum epochs (Weisshaar,

---

L. Jetsu  
 lauri.jetsu@helsinki.fi

<sup>1</sup> Department of Physics, P.O. Box 64, FI-00014 University of Helsinki, Finland

**Table 1.** Recent prolonged periods of weak sunspot activity.

Minimum	Duration	Reference
Dalton	1790 - 1830	Komitov and Kaftan (2004)
Maunder	1640 - 1720	Usoskin, Solanki, and Kovaltsov (2007)
Spörer	1390 - 1550	Usoskin, Solanki, and Kovaltsov (2007)
Wolf	1270 - 1340	Usoskin, Solanki, and Kovaltsov (2007)
Oort	1010 - 1070	Usoskin, Solanki, and Kovaltsov (2007)

Cameron, and Schüssler, 2023; Biswas et al., 2023). Such a “phase-lock” would not exist, if the sunspot data were multiperiodic.

The solar surface magnetic field is strongest in the sunspots. The polarity of this field is reversed at the beginning of each solar cycle. Therefore, the field geometry returns to its original state during the Hale cycle of about 22 years (Hale et al., 1919). One persistent solar cycle regularity has been the Gnevyshev–Ohl rule: every odd numbered sunspot cycle has had a higher amplitude than the preceding even numbered sunspot cycle (Gnevyshev and Ohl, 1948).

There have been prolonged periods when very few sunspots, or even none at all, were observed. The four most recent prolonged grand sunspot minima were identified by Usoskin, Solanki, and Kovaltsov (2007), who did not classify the Dalton minimum (Komitov and Kaftan, 2004) as a grand sunspot minimum. We give the epochs of these five most recent prolonged activity minima in our Table 1. The Earth’s climate temperature rises during strong solar activity (e.g. Van Geel et al., 1999). Thus, the current prolonged solar activity minimum helps us to cope with the human-induced climate change.

Parker (1955) presented the dynamo model, where the solar magnetic field arises from interaction between internal differential rotation and convection. Babcock (1961) and Leighton (1969) presented the first models of how this dynamo may generate the sunspot cycle. In his review of the current dynamo models of the solar cycles, Charbonneau (2010) stated that all physical mechanisms causing the solar cycles are not yet fully understood. He noted that the physical processes regulating the magnetic amplitude of the solar cycle are still unknown. It is also not known how the sunspot-forming magnetic flux ropes are produced by the dynamo-generated mean magnetic field. Very recently, Vasil et al. (2024) proposed that the solar magnetic cycles are caused by a dynamo resulting from near-surface magneto-rotational instability.

The solar magnetic field is frozen-in the outward-streaming solar wind (Parker, 1958, Figure 6). Dungey (1961) presented the idea that the magnetic reconnection is the primary physical process in the interaction between the solar wind and the Earth’s magnetosphere. The Earth’s and the Sun’s magnetic field lines reconnect intermittently on the dayside of the Earth during Flux Transfer Events (Russell, 2003; Kivelson and Bagenal, 2007, FTEs). These FTEs occur in bursts lasting on average about two minutes and having a repeat period of about eight minutes (Lockwood and Wild, 1993; Russell, 1995, 2003). In an FTE, the high-energy particles flow through the FTE magnetic flux rope, which acts like a portal connecting the Earth and the Sun (Glenn, 2019; Paul, Vaidya, and Strugarek, 2022). These FTE magnetic flux ropes show a tendency to form above the Earth’s equator, from where they roll over the Earth’s pole pointing away from the Sun, the winter pole (Raeder, 2006; Fear, Palmroth, and Milan, 2012; Nakariakov et al., 2016; Zhang et al., 2022). The FTEs are also observed in the magnetic fields of Mercury, Jupiter and Saturn (Sun et al., 2022). Many outstanding studies of the solar dynamo mention only the physical processes inside the Sun and therefore do not even mention the FTEs (e.g. Charbonneau, 2010; Vasil et al., 2024).

The official sunspot number forecast for the ongoing solar cycle 25 was made in the year 2019 by the Solar Cycle Prediction Panel, representing NOAA, NASA and the International Space Environmental Services (ISES). These forecasts are made only for one cycle at the time, because it is widely accepted that this stochastic variability is unpredictable beyond one solar cycle (Petrovay, 2020). Nevertheless, countless sunspot cycle predictions are constantly published (e.g. Asikainen and Mantere, 2023; Javaraiah, 2023; Krasheninnikov and Chumakov, 2023). The physical models for solar cycle prediction were recently reviewed by Bhowmik et al. (2023).

Wolf (1859) already argued that the variations in the sunspot cycle period may depend on Jupiter, Saturn, the Earth and Venus. There have been numerous attempts to find the connection between the planetary motions and the sunspot numbers (e.g. Schuster, 1911; Hantzsch, 1978). Recently, Stefani, Giesecke, and Weier (2019) formulated a solar-dynamo model, where planetary tidal forcing causes the sunspot cycle. Scafetta and Bianchini (2022) showed that the planetary tidal forces may alter the solar structure and cause the sunspot cycle. Charbonneau (2022) argued that the weak periodic tidal interaction signal of planets requires constant amplification because internal solar dynamo mechanisms can otherwise mask this signal.

The problem with the deterministic “planetary-influence-theory” is that long-term sunspot cycle predictions fail. At the moment, in the year 2024, the “solar-dynamo-theory” of a stochastic sunspot cycle is mainstream, while the “planetary-influence-theory” of a deterministic sunspot cycle is not. Here, we present successful deterministic sunspot number predictions, which are more accurate and extend over longer time intervals than the official Solar Cycle Prediction Panel forecast.

Section 2 describes the sunspot data. Section 3 introduces the Discrete Chi-square Method (DCM). Section 4 presents the results of our statistical DCM time series analysis of the sunspot data. We publish all details of this analysis in our DCM-manual.<sup>1</sup> Section 5 describes our Discrete Fourier Transform (DFT) cross-check for the DCM signal detections. We confirm that the DCM and the DFT detect the same extremely significant signals. Section 6 describes the predictability of sunspot data. We discuss our results in Section 7 and draw our conclusions in Section 8. The statistical identification of planetary signals is discussed separately in our Appendix.

## 2. Data

We retrieved the sunspot data from the Solar Influences Data Analysis Center<sup>2</sup> in December 2022. The monthly mean total sunspot number data begin in January 1749 and end to November 2022 (Table 2:  $n = 3287$ ). After January 1818, the monthly mean standard deviation ( $S_i$ ) of the input sunspot numbers from individual stations are available, as well as the total number of observations ( $N_i$ ).

The yearly mean total sunspot number data begin in the year 1700 and end to 2021 (Table 3:  $n = 322$ ). The  $S_i$  and  $N_i$  estimates are available after 1818.

The standard errors

$$\sigma_i = S_i / \sqrt{N_i} \quad (1)$$

---

<sup>1</sup>All analysed data and the DCM Python code are available in <https://zenodo.org/uploads/11503698>. Our DCM-manual gives detailed instructions for repeating the whole DCM analysis.

<sup>2</sup>Source: WDC SILSO, Royal Observatory of Belgium, Brussels

**Table 2.** Times  $t_i$  of monthly mean total sunspot numbers  $y_i$  ( $n = 3287$ ). The standard deviation ( $S_i$ ) and the total number of estimates ( $N_i$ ) are available from January 1818 onward. Values -1 indicate cases having no  $S_i$  and  $N_i$  estimate. This table shows only the first and the last lines, because all data is available in electronic form.

$t_i$ (y)	$y_i$ (-)	$S_i$ (-)	$N_i$ (-)
1749.042	96.7	-1	-1
...	...	...	...
2022.873	77.6	14.1	881

**Table 3.** Yearly mean total sunspot numbers ( $n = 322$ ), otherwise as in Table 2

$t_i$ (y)	$y_i$ (-)	$S_i$ (-)	$N_i$ (-)
1700.5	8.3	-1	-1
...	...	...	...
2021.5	29.6	7.9	15233

for these data give the weights  $w_i = \sigma_i^{-2}$ . The normalised weights are

$$w_{\text{nor},i} = nw_i / \sum_{i=1}^n w_i. \quad (2)$$

If all errors were equal, the normalised weight  $w_{\text{nor},i}$  for every observation would be one. For all monthly data, the normalised weights show that one observation out of  $n = 2458$  observations has the largest weight  $w_{\text{nor},\text{max}} = 381$  (Table 4, Line 1). The four most accurate,  $N_{1/2} = 4$ , observations influence the modeling more than the remaining  $n - 4 = 2454$  observations. These monthly data statistics improve slightly if the more accurate data after the year 2000 are removed, which gives  $N_{1/2} = 64$  for sample size  $n = 2183$ . All yearly data show an extreme case,  $N_{1/2} = 1$ , where the weight  $w_{\text{nor},\text{max}} = 135$  of one observation exceeds the weight of all other  $n - 1 = 203$  observations. Again, the statistics improve slightly if the more accurate data after the year 2000 are removed.

For these biased normalised weights, the period and the amplitude error estimates for the weighted data signals would be dramatically larger than the respective errors for the non-weighted data signals. For example, the bootstrap reshuffling (see Equation 25) of the four  $N_{1/2} = 4$  most accurate monthly values, or the one  $N_{1/2} = 1$  most accurate yearly value, resembles Russian roulette, where the majority of remaining other data values do not seem to need to fit to the model at all. We emphasise that the weighted data itself causes this bias, not our period analysis method.

**Table 4.** Normalised weights  $w_{\text{nor},i}$  for Equation 2. (1) Sample. (2) Sample size. (3,4) Maximum and minimum  $w_{\text{nor},i}$ . (5) Number of largest  $w_{\text{nor},i}$  having a sum exceeding  $n/2$ .

(1) Sample	(2) $n$	(3) $w_{\text{nor},\text{max}}$	(4) $w_{\text{nor},\text{min}}$	(5) $N_{1/2}$
(-)	(-)	(-)	(-)	(-)
Monthly data				
All	2458	381	$2.02 \times 10^{-5}$	4
Before 2000	2183	48.9	$1.83 \times 10^{-3}$	64
Yearly data				
All	204	135	$1.08 \times 10^{-3}$	1
Before 2000	182	21.6	$1.11 \times 10^{-2}$	6

We solve this statistical bias of errors  $\sigma_i$  by using the Sigma-cutoff weights

$$\begin{cases} w'_i = 1, & \text{if } \sigma_i \leq K\bar{\sigma} \\ w'_i = (K\bar{\sigma}/\sigma_i)^x, & \text{if } \sigma_i > K\bar{\sigma}, \end{cases} \quad (3)$$

where  $\bar{\sigma}$  is the mean of all  $\sigma_i$ , and the  $K$  and  $x$  values can be freely chosen (Handler, 2003; Breger et al., 2002). We use the same  $K = 1$  and  $x = 2$  values as Rodríguez et al. (2003), which gives

$$\begin{cases} \sigma'_i = 1, & \text{if } \sigma_i \leq \bar{\sigma} \\ \sigma'_i = \sigma_i/\bar{\sigma} > 1, & \text{if } \sigma_i > \bar{\sigma}. \end{cases} \quad (4)$$

Our chosen  $K$  and  $x$  values are reasonable, because they give 55 percent of monthly data having full weight 1, and 25 percent having weight below 1/2. The respective values for the yearly data are 53 and 24 percent.

There are four exceptional cases. We use the sigma cutoff weights  $w'_i = 1$  for the three exceptional cases  $y_i = 0$ ,  $S_i = 0$  and  $N_i > 0$ , which solves the infinite weight  $w_i = \sigma_i^{-2} = 0^{-2} = \infty$  problem. Finally, we compute no error estimate for the one exceptional case,  $S_i > 0$  and  $N_i = 0$ .

We analyse eight samples. The first four samples are monthly sunspot data drawn from Table 2. The last four samples are yearly sunspot data drawn from Table 3. All eight samples are published only in electronic form. We summarise the sample contents and sample naming abbreviations in Table 5.

## 2.1. Rmonthly and Rmonthly2000

Rmonthly is our largest sample ( $n = 3287$ ,  $\Delta T = 274^y$ ). It contains all  $t_i$  and  $y_i$  values from Table 2. Since the error estimates  $\sigma_i$  are unknown before January 1818, we use an arbitrary error  $\sigma_i = 1$  for all data in this sample. We perform a non-weighted period analysis, which is based on the sum of squared residuals (Equation 11:  $R$ ). Hence, the chosen  $\sigma_i = 1$  value has no effect to our analysis results, because every observation has an equal weight. The particular file name Rmonthly is used because the period analysis is based on a non-weighted  $R$  test statistic.

Rmonthly2000 contains observations from Rmonthly, which were made before the year 2000 ( $n = 3012$ ,  $\Delta T = 251^y$ ). Number “2000” refers to the omitted data after the year 2000.

**Table 5.** Eight sunspot data samples. (1) Table from where sample is drawn. (2) Sample name. (3-4) Sample first and last observing time. (5) Sample time span. (6) Sample size. (7) Sample electronic file name.

(1) Table	(2) Name	(3) $t_1$ (y)	(4) $t_n$ (y)	(5) $\Delta T$ (y)	(6) $n$ (-)	(7) File
Table 2	Rmonthly	1749.0	2022.8	273.8	3287	Rmonthly.dat
Table 2	Rmonthly2000	1749.0	1999.9	250.9	3012	Rmonthly2000.dat
Table 2	Cmonthly	1818.0	2022.8	204.8	2458	Cmonthly.dat
Table 2	Cmonthly2000	1818.0	1999.9	181.9	2182	Cmonthly2000.dat
Table 3	Ryearly	1700.5	2021.5	321.0	322	Ryearly.dat
Table 3	Ryearly2000	1700.5	1999.5	299.0	300	Ryearly2000.dat
Table 3	Cyearly	1818.5	2021.5	203.0	204	Cyearly.dat
Table 3	Cyearly2000	1818.5	1995.5	181.0	182	Cyearly2000.dat

## 2.2. Cmonthly and Cmonthly2000

Cmonthly contains all  $t_i$  and  $y_i$  observations having an error estimate  $\sigma'_i$  computed from Equation 4 ( $n = 2458$ ,  $\Delta T = 205^y$ ). For this sample, we apply the weighted period analysis, which utilises the error  $\sigma'_i$  information (Equation 12:  $\chi^2$ ). The sample name begins with letter “C”, because our analysis is based on the weighted Chi-square test statistic (Equation 18).

Cmonthly2000 contains those Cmonthly observations, which were made before the year 2000 ( $n = 2182$ ,  $\Delta T = 182^y$ ). We refer to the omitted data after the year 2000 by using the number “2000”.

## 2.3. Ryearly and Ryearly2000

Ryearly is our longest sample ( $\Delta T = 321^y$ ) containing  $n = 322$  yearly mean total sunspot number observations over more than three centuries. Since no error estimates are available for observations before 1818, the value  $\sigma_i = 1$  is used for all data. We perform a non-weighted period analysis based on the  $R$  test statistic (Equation 11). Therefore, the sample name begins with the letter “R”.

Ryearly2000 contains observations from Ryearly that were made before the year 2000.

## 2.4. Cyearly and Cyearly2000

Cyearly is the smallest sample ( $n = 204$ ,  $\Delta T = 204^y$ ). It contains all yearly mean total sunspot numbers having an error estimate  $\sigma'_i$  (Equation 4). We perform a weighted period analysis based on the  $\chi^2$  test statistic (Equation 12). Therefore, the sample name begins with the letter “C”.

Cyearly2000 contains all Cyearly data before the year 2000.

## 3. Discrete Chi-Square Method (DCM)

In this section, we give a thorough description the Discrete Chi-Square Method (DCM), because this is essential for understanding the results of our sunspot data analysis. Jetsu (2020, Paper I) formulated this method. He used DCM to discover the periods of a third and a fourth body from the O-C data of the eclipsing binary XZ And. An improved DCM version revealed the presence

of numerous new companion candidates in the eclipsing binary Algol (Jetsu, 2021, Paper II). DCM is designed for detecting many signals superimposed on an arbitrary trend.

The sunspot number data notations are observations  $y_i = y(t_i) \pm \sigma_i$ , where  $t_i$  are the observing times and  $\sigma_i$  are the errors ( $i = 1, 2, \dots, n$ ). The units are  $[y_i] = \text{dimensionless}$ ,  $[\sigma_i] = \text{dimensionless}$  and  $[t_i] = \text{years}$ . The time span of data is  $\Delta T = t_n - t_1$ . The mid point is  $t_{\text{mid}} = t_1 + \Delta T/2$ . Our notations for the mean and the standard deviation of all  $y_i$  values are  $m$  and  $s$ , respectively.

DCM model

$$g(t) = g(t, K_1, K_2, K_3) = h(t) + p(t). \quad (5)$$

is a sum of a periodic function

$$h(t) = h(t, K_1, K_2) = \sum_{i=1}^{K_1} h_i(t) \quad (6)$$

$$h_i(t) = \sum_{j=1}^{K_2} B_{i,j} \cos(2\pi j f_i t) + C_{i,j} \sin(2\pi j f_i t), \quad (7)$$

and an aperiodic function

$$p(t) = p(t, K_3) = \begin{cases} 0, & \text{if } K_3 = -1 \\ \sum_{k=0}^{K_3} p_k(t), & \text{if } K_3 = 0, 1, 2, \dots \end{cases} \quad (8)$$

where

$$p_k(t) = M_k \left[ \frac{2(t - t_{\text{mid}})}{\Delta T} \right]^k. \quad (9)$$

The periodic  $h(t)$  function is a sum of  $K_1$  harmonic  $h_i(t)$  signals having frequencies  $f_i$ .

The signal order is  $K_2$ . For simplicity, we refer to  $K_2 = 1$  order models as “pure sine” models, and to  $K_2 = 2$  order models as “double wave” models. The former category of signal curves are pure sines. The latter category of signal curves can deviate from a pure sine.

The  $h_i(t)$  signals are superimposed on the aperiodic  $K_3$  order polynomial trend  $p(t)$ . Function  $h(t)$  repeats itself in time. Function  $p(t)$  does not repeat itself, except when  $p(t) = 0$  for  $K_3 = -1$  or  $p(t) = M_0 = \text{constant}$  for  $K_3 = 0$ .

DCM model residuals are

$$\epsilon_i = y(t_i) - g(t_i) = y_i - g_i. \quad (10)$$

Our notations for the mean and standard deviation of the residuals are  $m_\epsilon$  and  $s_\epsilon$ . These residuals give the sum of squared residuals

$$R = \sum_{i=1}^n \epsilon_i^2, \quad (11)$$

and also the Chi-square

$$\chi^2 = \sum_{i=1}^n \frac{\epsilon_i^2}{\sigma_i^2}. \quad (12)$$

If the data errors  $\sigma_i$  are known, we use  $\chi^2$  to estimate the goodness of our model. For unknown errors  $\sigma_i$ , we use  $R$ .

Our notation for  $K_1$ ,  $K_2$  and  $K_3$  order DCM model  $g(t)$  is “ $\mathcal{M}_{K_1, K_2, K_3, R}$ ” or “ $\mathcal{M}_{K_1, K_2, K_3, \chi^2}$ ”. The last subscripts “ $R$ ” or “ $\chi^2$ ” refer to the use of Equation 11 or 12 in estimating the goodness of our model, respectively.

The free parameters of model  $g(t)$  are

$$\boldsymbol{\beta} = [\beta_1, \beta_2, \dots, \beta_\eta] = [B_{1,1}, C_{1,1}, f_1, \dots, B_{K_1, K_2}, C_{K_1, K_2}, f_{K_1}, M_0, \dots, M_{K_3}], \quad (13)$$

where

$$\eta = K_1 \times (2K_2 + 1) + K_3 + 1 \quad (14)$$

is the number of free parameters. We divide the free parameters  $\boldsymbol{\beta}$  into two groups

$$\boldsymbol{\beta}_I = [f_1, \dots, f_{K_1}] \quad (15)$$

$$\boldsymbol{\beta}_{II} = [B_{1,1}C_{1,1}, \dots, B_{K_1, K_2}, C_{K_1, K_2}, M_0, \dots, M_{K_3}] \quad (16)$$

The first frequency group  $\boldsymbol{\beta}_I$  makes the  $g(t)$  model non-linear, because all free parameters are not eliminated from all partial derivatives  $\partial g / \partial \beta_i$ . If these  $\boldsymbol{\beta}_I$  frequencies are fixed to the constant known tested numerical values, none of the partial derivatives  $\partial g / \partial \beta_i$  contain any free parameters. In this case, the model becomes *linear*, and the solution for the second group of free parameters,  $\boldsymbol{\beta}_{II}$  is *unambiguous*. Our concepts like “linear model” and “unambiguous result” refer to this type of models and their free parameter solutions.

For every tested frequency combination  $\boldsymbol{\beta}_I = [f_1, f_2, \dots, f_{K_1}]$ , we compute the DCM test statistic

$$z = z(f_1, f_2, \dots, f_{K_1}) = \sqrt{R/n} \quad (17)$$

$$z = z(f_1, f_2, \dots, f_{K_1}) = \sqrt{\chi^2/n} \quad (18)$$

from a linear model least squares fit. We use Equation 17 or Equation 18, for unknown or known  $\sigma_i$  errors, respectively.

For two signal  $K_1 = 2$  model, the sum  $h(t)$  of signals  $h_1(t)$  and  $h_2(t)$  does not depend on the order in which these signals are added. This causes the symmetry  $z(f_1, f_2) = z(f_2, f_1)$  for all tested frequency pairs  $f_1$  and  $f_2$ . The same symmetry applies to any other  $K_1$  number of signals. Therefore, we compute  $z$  test statistic only for all combinations

$$f_{\max} \geq f_1 > f_2 > \dots > f_{K_1} \geq f_{\min}, \quad (19)$$

where  $f_{\min}$  and  $f_{\max}$  are the minimum and maximum tested frequencies, respectively. In the long search, we test an evenly spaced grid of  $n_L$  frequencies between  $f_{\min}$  and  $f_{\max}$ . This gives us the best frequency candidates  $f_{1,\text{mid}}, \dots, f_{K_1,\text{mid}}$ . In the short search, we test a denser grid of  $n_S$  frequencies within an interval

$$[f_{i,\text{mid}} - a, f_{i,\text{mid}} + a], \quad (20)$$

where  $a = c(f_{\min} - f_{\max})/2$  and  $i = 1, \dots, K_1$ . In this study, we use  $c = 0.05$  which means that the tested short search frequency interval represents 5% of the tested long search interval.

We search for periods between  $P_{\min} = 1/f_{\max} = 5$  years and  $P_{\max} = 1/f_{\min} = 200$  years. The reasons for not detecting periods below  $P_{\min} = 5$  years are discussed in Appendix (Section A).

The best linear model for the data gives the global periodogram minimum

$$z_{\min} = z(f_{1,\text{best}}, f_{2,\text{best}}, \dots, f_{K_1,\text{best}}) \quad (21)$$

at the tested frequencies  $f_{1,\text{best}}, f_{2,\text{best}}, \dots, f_{K_1,\text{best}}$ .

The scalar  $z$  periodogram values are computed from  $K_1$  frequency values. For example,  $K_1 = 2$  two signal periodogram  $z(f_1, f_2)$  could be plotted like a map, where  $f_1$  and  $f_2$  are the coordinates, and  $z = z(f_1, f_2)$  is the height. For three or more signals, such a direct graphical presentation becomes impossible, because it requires more than three dimensions. We solve this problem by presenting only the following one-dimensional slices of the full periodogram

$$\begin{aligned} z_1(f_1) &= z(f_1, f_{2,\text{best}}, \dots, f_{K_1,\text{best}}) \\ z_2(f_2) &= z(f_{1,\text{best}}, f_2, f_{3,\text{best}}, \dots, f_{K_1,\text{best}}) \\ z_3(f_3) &= z(f_{1,\text{best}}, f_{2,\text{best}}, f_3, f_{4,\text{best}}, \dots, f_{K_1,\text{best}}) \\ z_4(f_4) &= z(f_{1,\text{best}}, f_{2,\text{best}}, f_{3,\text{best}}, f_4, f_{5,\text{best}}, f_{K_1,\text{best}}) \\ z_5(f_5) &= z(f_{1,\text{best}}, f_{2,\text{best}}, f_{3,\text{best}}, f_{4,\text{best}}, f_5, f_{K_1,\text{best}}) \\ z_6(f_6) &= z(f_{1,\text{best}}, f_{2,\text{best}}, f_{3,\text{best}}, f_{4,\text{best}}, f_{5,\text{best}}, f_6). \end{aligned} \quad (22)$$

Using the above  $K_1 = 2$  map analogy, the slice  $z_1(f_1)$  represents the height  $z$  at a  $f_1$  coordinate when moving along the constant line  $f_2 = f_{2,\text{best}}$  that crosses the global minimum  $z_{\min}$  (Equation 21) at the coordinate point  $(f_{1,\text{best}}, f_{2,\text{best}})$ .

The best frequencies detected in the short search give the initial values for the first group of free parameters  $\beta_{\text{I,initial}} = [f_{1,\text{best}}, \dots, f_{K_1,\text{best}}]$  (Equation 15). The linear model with these constant  $[f_{1,\text{best}}, \dots, f_{K_1,\text{best}}]$  frequency values gives the unambiguous initial values for the second group  $\beta_{\text{II,initial}}$  of free parameters (Equation 16). The final non-linear iteration is performed from

$$\beta_{\text{initial}} = [\beta_{\text{I,initial}}, \beta_{\text{II,initial}}] \rightarrow \beta_{\text{final}}. \quad (23)$$

DCM determines the following parameters for  $h_i(t)$  signals

$$\begin{aligned} P_i &= 1/f_i = \text{Period} \\ A_i &= \text{Peak to peak amplitude} \\ t_{i,\min,1} &= \text{Deeper primary minimum epoch} \\ t_{i,\min,2} &= \text{Secondary minimum epoch (if present)} \\ t_{i,\max,1} &= \text{Higher primary maximum epoch} \\ t_{i,\max,2} &= \text{Secondary maximum epoch (if present)}, \end{aligned}$$

as well the  $M_k$  parameters of the  $p(t)$  trend. For the sunspots, the most interesting parameters are the signal periods  $P_i$ , the signal amplitudes  $A_i$ , and signal primary minimum epochs  $t_{\min,1}$  (DCM-manual: Tables 6-17).

The subtraction

$$y_{i,j} = y_i - [g(t_i) - h_j(t_i)] \quad (24)$$

shows how well all observations  $y_i$  are connected to any signal  $h_j(t)$ , where  $j = 1, \dots, K_1$ . In other words, the full model  $g(t_i)$  is subtracted from the data  $y_i$ , except for the  $h_j(t_i)$  signal itself. We show an example of this subtraction in our DCM-manual (Figure 3). This subtraction resembles the Discrete Fourier Transform de-trending procedure (e.g. Murphy, 2012), but here we remove both the trend and all other signals, except for the  $h_j(t_i)$  signal.

The DCM model parameter errors are determined with the bootstrap procedure (Efron and Tibshirani, 1986). We have previously used this same bootstrap procedure in our TSPA- and CPS-methods (Jetsu and Pelt, 1999; Lehtinen et al., 2011). A random sample  $\epsilon^*$  is selected from the residuals  $\epsilon$  of the DCM model (Equation 10). In this reshuffling of  $\epsilon_i$  residuals, any  $\epsilon_i$  can be chosen as many times as the random selection happens to favour it. This random sample of residuals gives the *artificial* bootstrap data sample

$$y_i^* = g_i + \epsilon_i^*. \quad (25)$$

We create numerous such  $y^*$  random samples. The DCM model for each  $y^*$  sample gives one estimate for every model parameter. The error estimate for each particular model parameter is the standard deviation of all estimates obtained from all  $y^*$  bootstrap samples.

DCM models are nested. For example, a one signal model is a special case of a two signal model. DCM uses the Fisher-test to compare any pair of simple  $g_1(t)$  and complex  $g_2(t)$  models. Their number of free parameters are  $\eta_1 < \eta_2$ . Their sums of squared residuals ( $R_1, R_2$ ) and Chi-squares ( $\chi_1, \chi_2$ ) give the Fisher-test test statistic

$$F_R = \left( \frac{R_1}{R_2} - 1 \right) \left( \frac{n - \eta_2 - 1}{\eta_2 - \eta_1} \right) \quad (26)$$

$$F_\chi = \left( \frac{\chi_1^2}{\chi_2^2} - 1 \right) \left( \frac{n - \eta_2 - 1}{\eta_2 - \eta_1} \right). \quad (27)$$

The Fisher-test null hypothesis is

$H_0$ : “The complex model  $g_2(t)$  does not provide a significantly better fit to the data than the simple model  $g_1(t)$ .”

Under  $H_0$ , both test statistic parameters  $F_R$  and  $F_\chi$  have an  $F$  distribution with  $(\nu_1, \nu_2)$  degrees of freedom, where  $\nu_1 = \eta_2 - \eta_1$  and  $\nu_2 = n - \eta_2$  (Draper and Smith, 1998). The probability for  $F_R$  or  $F_\chi$  reaching values higher than  $F$  is called the critical level  $Q_F = P(F_R \geq F)$  or  $Q_F = P(F_\chi \geq F)$ . We reject the  $H_0$  hypothesis, if

$$Q_F < \gamma_F = 0.001, \quad (28)$$

where  $\gamma_F$  is the pre-assigned significance level. This  $\gamma_F$  represents the probability of falsely rejecting  $H_0$  hypothesis when it is in fact true. If  $H_0$  is rejected, we rate the complex  $g_2(t)$  model better than the simple  $g_1(t)$  model.

The basic idea of the Fisher-test is simple. The  $H_0$  hypothesis rejection probability increases for larger  $F_R$  values having smaller  $Q_F$  critical levels. The complex model  $R_2$  or  $\chi_2^2$  values decrease when the  $\eta_2$  number of free parameters increases. This increases the first  $(R_1/R_2 - 1)$  and  $(\chi_1^2/\chi_2^2 - 1)$  terms in Equations 26 and 27. However, the second  $(n - \eta_2 - 1)/(\eta_2 - \eta_1)$  penalty term decreases at the same time. This second penalty term prevents over-fitting, i.e. accepting complex models having too many  $\eta_2$  free parameters.

The key ideas of DCM are based on the following robust, thoroughly tested statistical approaches

1. The DCM model  $g(t)$  is *non-linear* (Equation 5). This model becomes *linear* when the frequencies  $\beta_I = [f_1, \dots, f_{K_1}]$  (Equation 15) are fixed to their tested numerical values. This linear model gives *unambiguous* results for the other free parameters,  $\beta_{II}$  (Equation 16).
2. The short search  $f_{1,\text{best}} > f_{2,\text{best}} > \dots > f_{K_1,\text{best}}$  grid combination that minimises the  $z$  test statistic gives the best initial  $\beta_{\text{initial}}$  values for the non-linear iteration of Equation 23.

3. DCM tests a dense grid of all possible frequency combinations  $f_{\max} \geq f_1 > f_2 > \dots > f_{K_1} \geq f_{\min}$  (Equation 19). For every frequency combination, the *unambiguous linear* model least squares fit gives the test statistic  $z = \sqrt{\chi^2/n}$  (errors  $\sigma_i$  known) or  $z = \sqrt{R/n}$  (errors  $\sigma_i$  unknown).
4. All model parameter error estimates are determined with the bootstrap method (Equation 25).
5. The best model is identified using the Fisher-test, which compares all different tested  $K_1$ ,  $K_2$  and  $K_3$  order combinations for nested models (Draper and Smith, 1998; Allen, 2004).

DCM has the following restrictions

1. If the frequency grid  $f_1 > f_2 > \dots > f_{K_1}$  contains  $n_L$  values in the long search, then the total number of all tested frequency combinations is

$$\binom{n_L}{K_1} = \frac{n_L!}{K_1!(n_L - K_1)!}. \quad (29)$$

For example, it took about two days for a cluster of processors to compute the four signal DCM model for the Rmonthly2000 sample (DCM-manual: Figures 1-4).

2. An adequately dense tested frequency grid eliminates the possibility that the best frequency combination is missed. The restriction is that denser grids require more computation time. If the tested frequency grid is sufficiently dense, no abrupt periodogram jumps occur, because the  $z$  values for all close tested frequencies correlate. Hence, the frequencies of the minima of these periodograms are accurately determined. There is no need to test an even denser grid, because this would not alter the final result of the non-linear iteration of Equation 23.
3. Some DCM models are unstable. They are simply wrong models for the data, like a wrong  $p(t)$  trend order  $K_3$  or a search for too few or too many  $K_1$  signals (e.g., Paper I: Figures 5-10). This causes model instability. We denote such unstable models with "UM" (DCM-manual: Tables 6-17). The signatures of such unstable models are

"IF" = Intersecting frequencies  
 "AD" = Dispersing amplitudes  
 "LP" = Leaking periods

Intersecting frequencies "IF" occur when the frequencies of two signals are very close to each other. For example, if frequency  $f_1$  approaches frequency  $f_2$ , the  $h_1(t)$  and  $h_2(t)$  signals become essentially one and the same signal. This ruins the least squares fit. It makes no sense to add the same signal twice.

Dispersing amplitudes "AD" also occur when two signal frequencies are close to each other, like in the above-mentioned "IF" cases. The least squares fit uses two high amplitude signals which cancel out. Hence, the sum of these two high amplitude signals is one low amplitude signal that fits to the data.

We take extra care to identify the suspected "IF" and "AD" unstable model cases. The reshuffling of bootstrap  $\epsilon^*$  residuals provides a good test for identifying such unstable models from the DCM analysis of numerous artificial bootstrap data samples  $\mathbf{y}^*$  (Equation 25). If we encounter any signs of instability, we test combinations  $n_L = 100 \& c = 0.05$ ,  $n_L = 100 \& c = 0.10$ ,  $n_L = 120 \& c = 0.05$  and  $n_L = 120 \& c = 0.10$ . If there is instability in any of these combinations, we reject the model as unstable ("UM"). If there is no instability, we take the  $n_L$  and  $c$  combination that gives the lowest value for  $R$  (non-weighted data) or  $\chi^2$  (weighted data).

Leaking periods "LP" instability refers to the cases, where the detected frequency  $f$  is outside the tested frequency interval between  $f_{\min}$  and  $f_{\max}$ , or the period  $P = 1/f$  of this frequency is longer than the time span  $\Delta T$  of the data.

We use the DCM model  $g(t_i, \beta)$  to predict the future and past data. The three samples used in these predictions are the predictive data, the predicted data and all data. We use the following notations for the time points, the observations and the errors of these three samples.

- Predictive data:  $n$  values of  $t_i$ ,  $y_i$  and  $\sigma_i$
- Predicted data:  $n'$  values of  $t'_i$ ,  $y'_i$  and  $\sigma'_i$
- All data:  $n'' = n + n'$  values of  $t''_i$ ,  $y''_i$  and  $\sigma''_i$  from predictive and predicted data

We also compute the monthly or yearly time points during past activity minima of Table 1. Our notations for these time points are

- Activity minimum data:  $n'''$  values of  $t'''_i$

DCM gives the best free parameter  $\beta$  values for the predictive data model  $g_i = g(t_i, \beta)$ , where the “old”  $t_{\text{mid}}$  and  $\Delta T$  values are computed from the predictive data time points  $t_i$ . These “old” predictive data  $t_{\text{mid}}$  and  $\Delta T$  values are used to compute the predicted data model values

$$g'_i = g(t'_i, \beta)$$

In other words, we do not compute “new”  $t_{\text{mid}}$  and  $\Delta T$  values from the predicted data time points  $t'_i$ . There is an obvious reason for this. The predictive data free parameter values  $\beta$  give the correct  $g'_i$  values only for the “old” predictive data  $t_{\text{mid}}$  and  $\Delta T$  values. The residuals

$$\epsilon'_i = y'_i - g'_i$$

of the predicted data give the *predicted test statistic*

$$z_{\text{pred}} = z \text{ test statistic for predicted data (Equation 17 or 18),} \quad (30)$$

which measures how well the prediction obtained from the predictive data works.

The best DCM model  $g(t''_i, \beta)$  for all data uses the “old”  $t_{\text{mid}}$  and  $\Delta T$  values computed from  $t''_i$  time points of all data. We use these “old”  $t_{\text{mid}}$  and  $\Delta T$  values to compute the predicted model values

$$g'''_i = g(t'''_i, \beta) \quad (31)$$

for the monthly or yearly time points  $t'''_i$  during the chosen activity minimum of Table 1. These  $g'''_i$  values give the *predicted mean level*

$$m_{\text{pred}} = \frac{1}{n'''} \sum_{i=1}^{n'''} g'''_i \quad (32)$$

during the selected activity minimum of Table 1.

It is essential to understand how and why the above two predictive parameters of Equations 30 and 32 are computed. The former parameter,  $z_{\text{pred}}$ , is computed from the *known*  $t'_i$ ,  $y'_i$  and  $\sigma'_i$  values of the predicted data. If our predictions are correct, the following regularities should occur

- $z_{\text{pred}}$  decreases, if DCM detects real new signals in the predictive data
- $z_{\text{pred}}$  increases, if DCM detects unreal new signals in the predictive data

For the latter  $m_{\text{pred}}$  parameter, the  $t_i''', y_i'''$  or  $\sigma_i'''$  data values during the past activity minima are *unknown*, but we can create the  $n'''$  monthly or yearly  $t_i'''$  time points during these minima of Table 1. We can then compute the  $g_i'''$  values from these  $t_i'''$  values (Equation 31). This gives us the mean  $m_{\text{pred}}$  value (Equation 32) that can be compared to the mean level  $m$  for all data. If our predictions for the past activity minima of Table 1 are correct, the following regularities should occur

- $m_{\text{pred}}$  falls below  $m$ , if DCM detects real new signals in all data
- $m_{\text{pred}}$  decreases, if DCM detects real new signals in all data
- $m_{\text{pred}}$  increases, if DCM detects unreal new signals in all data

Our model is non-linear (Equations 5 - 9). We find a unique solution for this ill-posed problem. The stages of finding this solution are

1. We fix the numerical values of the tested frequencies  $\beta_I$  (Equation 15). The model becomes linear and the solution for the other free parameters  $\beta_{II}$  is unique (Equation 16).
2. We test all possible  $\beta_I$  frequency combinations (Equation 19). The linear model for every tested frequency combination  $\beta_I$  gives a unique value for the test statistic  $z$  (Equations 17 and 18). We select the best frequency combination  $\beta_{I,\text{best}}$  that minimises  $z$ . The model for this best frequency combination is unique and the free parameter values  $\beta_{\text{initial}} = [\beta_{I,\text{best}}, \beta_{II,\text{best}}]$  of this model are unique.
3. These unique initial free parameter values  $\beta_{\text{initial}}$  are used in the non-linear iteration (Equation 23) that gives the unique final free parameter values  $\beta_{\text{final}}$ . This solution is unique.
4. We use the Fisher-test to compare many different non-linear models against each other. The selection criterion for the best model is unique (Equation 28).

After the selection of the tested non-linear models, these four stages give a unique the solution for this ill-posed problem.

#### 4. DCM period detections between 5 and 200 years

We must introduce the “double sinusoid” concept before comparing our DCM period detections. The shape of these double sinusoid signals resembles that of a pure sinusoid (Figures 1a-g). All seven double sinusoids are highlighted with the notation “ $2\times$ ” in Table 6. For example, we detect only one signal for the double wave  $K_2 = 2$  model of **Cmonthly** sample (Table 6: Column 9, Figure 1a). The period of this  $S_{11y}$  signal is  $P = 21.667 \pm 0.014 = 2 \times (10.834 \pm 0.007)$  years. The period of this double sinusoid signal is about two times longer than the  $S_{11y}$  signal periods detected in all other eleven samples. In other words, including the **Cmonthly** sample, DCM detects this same  $S_{11y}$  signal in all twelve samples.

We analyse twelve samples<sup>3</sup> and detect only nine signals in the period range between 5 and 200 years (DCM-manual: Tables 6-17). This leaves very little room for inconsistency. The periods and the amplitudes of the nine signals are summarised in Table 6, where we introduce the following signal abbreviations  $S_{11y}$ ,  $S_{10y}$ ,  $S_{11.y86}$ ,  $S_{110y}$ ,  $S_{10.y6}$ ,  $S_{8.y4}$ ,  $S_{53y}$ ,  $S_{8y}$  and  $S_{66y}$ . The numerical values in the subscripts of our signal abbreviations refer to the signal period in Earth years. These signals are arranged into the order of decreasing strength, or equivalently, of decreasing amplitude. We use the signal ranking based on the signal amplitudes in the first analysed sample **Rmonthly2000** (DCM-manual: Table 6), because this order for signal amplitudes varies slightly in different samples. For each particular sample, we give the exact signal ranking order in Table 6. Our DCM detects the same signals for

---

<sup>3</sup>All analysed data and the DCM Python code are available in <https://zenodo.org/uploads/11503698>. Our DCM-manual gives detailed instructions for repeating the whole DCM analysis.

**Table 6.:** Signals in monthly and yearly sunspot numbers. (1) Signal abbreviation. (2) Rmonthly2000 sample results for pure sines (DCM-manual: Table 6). All six detected signals are given in order of decreasing peak to peak amplitude  $A$ . (3-13) Results for other samples with chosen  $K_2$  values. Double sinusoid signals are denoted with “ $2\times$ ”. Notes below give an example of how to read this table.

(1)	(2)	(3)	(4)	(5)	(6)	(7)	(8)	(9)	(10)	(11)	(12)	(13)
Signal	Rmonthly2000 $K_2 = 1$	Rmonthly $K_2 = 1$	Rmonthly2000 $K_2 = 2$	Rmonthly $K_2 = 2$	Cmonthly2000 $K_2 = 1$	Cmonthly $K_2 = 1$	Cmonthly2000 $K_2 = 2$	Ryearly2000 $K_2 = 1$	Ryearly $K_2 = 1$	Cyearly2000 $K_2 = 1$	Cyearly $K_2 = 1$	
	Rank (-)	Rank (-)	Rank (-)	Rank (-)	Rank (-)	Rank (-)	Rank (-)	Rank (-)	Rank (-)	Rank (-)	Rank (-)	
	$P$ (y)	$P$ (y)	$P$ (y)	$P$ (y)	$P$ (y)	$P$ (y)	$P$ (y)	$P$ (y)	$P$ (y)	$P$ (y)	$P$ (y)	
	$A$ (-)	$A$ (-)	$A$ (-)	$A$ (-)	$A$ (-)	$A$ (-)	$A$ (-)	$A$ (-)	$A$ (-)	$A$ (-)	$A$ (-)	
$S_{11y}$	(1) 11.0324 $\pm$ 0.0048	(1) 11.0033 $\pm$ 0.0064	(1) 11.0234 $\pm$ 0.0068	(1) 10.9878 $\pm$ 0.0051	(1) 10.8054 $\pm$ 0.013	(1) 10.8585 $\pm$ 0.0048	(1) 10.8074 $\pm$ 0.012	(1) 21.6674 $\pm$ 0.014 $\times$	(1) 11.0064 $\pm$ 0.017	(1) 10.9814 $\pm$ 0.020	(1) 10.8134 $\pm$ 0.029	(1) 10.8634 $\pm$ 0.022
	98.8 $\pm$ 2.6	101.5 $\pm$ 2.5	102.9 $\pm$ 2.7	104.6 $\pm$ 2.3	118.2 $\pm$ 3.7	117.5 $\pm$ 2.9	123.5 $\pm$ 3.0	132.6 $\pm$ 3.4	90.4 $\pm$ 4.7	98.3 $\pm$ 7.8	119.2 $\pm$ 8.5	119.3 $\pm$ 7.5
$S_{10y}$	(2) 9.9842 $\pm$ 0.0075	(2) 10.0001 $\pm$ 0.0081	(2) 9.9882 $\pm$ 0.0061	(2) 20.0062 $\pm$ 0.0088 $\times$	(2) 10.1964 $\pm$ 0.027	(2) 10.0658 $\pm$ 0.0077	(2) 10.1964 $\pm$ 0.017	(2) 9.9804 $\pm$ 0.016	(2) 9.9754 $\pm$ 0.017	(2) 10.1844 $\pm$ 0.064	(2) 10.0584 $\pm$ 0.026	(2) 11.8564 $\pm$ 0.068
	77.4 $\pm$ 2.2	65.5 $\pm$ 2.1	78.6 $\pm$ 2.6	75.2 $\pm$ 2.7	61.9 $\pm$ 3.9	59.3 $\pm$ 2.8	62.1 $\pm$ 3.7	64.6 $\pm$ 7.6	62.8 $\pm$ 6.1	62.3 $\pm$ 6.8	61.0 $\pm$ 9.6	43.8 $\pm$ 7.9
$S_{11,y86}$	(3) 11.8464 $\pm$ 0.012	(3) 11.8074 $\pm$ 0.012	(4) 23.3864 $\pm$ 0.0182 $\times$	(4) 11.7704 $\pm$ 0.11	(4) 11.8634 $\pm$ 0.021	(4) 11.8634 $\pm$ 0.021	(4) 11.8634 $\pm$ 0.027	(5) 11.8624 $\pm$ 0.034	(5) 11.8204 $\pm$ 0.027	(5) 10.3424 $\pm$ 0.034	(5) 10.3424 $\pm$ 0.034	(4) 11.8564 $\pm$ 0.068
	60.0 $\pm$ 2.2	56.4 $\pm$ 2.4	69.4 $\pm$ 2.7	62.7 $\pm$ 2.6	43.3 $\pm$ 2.0	43.3 $\pm$ 2.0	42.6 $\pm$ 4.1	40.5 $\pm$ 3.3	42.6 $\pm$ 4.1	40.5 $\pm$ 3.3	43.8 $\pm$ 7.9	53.8 $\pm$ 5.2
$S_{11,y86}$	(4) 96.2 $\pm$ 1.0	(4) 99.92 $\pm$ 0.57	(3) 104.16 $\pm$ 0.59	(3) 104.23 $\pm$ 0.68	(3) 116.7 $\pm$ 1.3	(3) 100.3 $\pm$ 2.1	(3) 101.4 $\pm$ 2.4	(4) 100.3 $\pm$ 2.1	(4) 101.4 $\pm$ 2.4	(4) 101.4 $\pm$ 2.4	(4) 101.4 $\pm$ 2.4	(3) 115.6 $\pm$ 3.6
	50.1 $\pm$ 2.8	51.8 $\pm$ 2.3	70.4 $\pm$ 3.6	68.1 $\pm$ 2.7	52.9 $\pm$ 2.5	52.4 $\pm$ 6.3	51.7 $\pm$ 4.9	52.4 $\pm$ 6.3	51.7 $\pm$ 4.9	51.7 $\pm$ 4.9	51.7 $\pm$ 4.9	53.8 $\pm$ 5.2
$S_{10,y6}$	(5) 10.5414 $\pm$ 0.014	(5) 10.5694 $\pm$ 0.020	(5) 10.5374 $\pm$ 0.0075	(5) 10.5404 $\pm$ 0.0600	(3) 10.6204 $\pm$ 0.033	(3) 10.6594 $\pm$ 0.031	(3) 10.6594 $\pm$ 0.031	(3) 10.6204 $\pm$ 0.033	(3) 10.6594 $\pm$ 0.031	(3) 10.6594 $\pm$ 0.031	(3) 10.6594 $\pm$ 0.031	(3) 115.6 $\pm$ 3.6
	45.0 $\pm$ 1.8	51.0 $\pm$ 1.8	51.2 $\pm$ 1.8	55.6 $\pm$ 2.3	52.4 $\pm$ 8.5	59.9 $\pm$ 8.6	59.9 $\pm$ 8.6	59.9 $\pm$ 8.6	59.9 $\pm$ 8.6	59.9 $\pm$ 8.6	59.9 $\pm$ 8.6	53.8 $\pm$ 5.2
$S_{8,y4}$			(6) 16.7814 $\pm$ 0.0342 $\times$	(6) 16.7534 $\pm$ 0.0272 $\times$	(7) 41.2 $\pm$ 3.1	(7) 33.0 $\pm$ 4.4	(7) 31.1 $\pm$ 4.8	(7) 8.4604 $\pm$ 0.027	(7) 8.4664 $\pm$ 0.016	(7) 8.4664 $\pm$ 0.016	(7) 8.4664 $\pm$ 0.016	(7) 8.4664 $\pm$ 0.016
			(6) 52.6 $\pm$ 0.27	(6) 33.9 $\pm$ 2.0	(6) 33.0 $\pm$ 4.4	(6) 31.1 $\pm$ 4.8	(6) 33.0 $\pm$ 4.4	(6) 53.244 $\pm$ 0.78	(6) 53.834 $\pm$ 0.76	(6) 53.834 $\pm$ 0.76	(6) 53.834 $\pm$ 0.76	(6) 53.834 $\pm$ 0.76
$S_{5,3y}$								(8) 8.0094 $\pm$ 0.017	(8) 8.0094 $\pm$ 0.017	(8) 8.0094 $\pm$ 0.017	(8) 8.0094 $\pm$ 0.017	(8) 8.0094 $\pm$ 0.017
			(6) 8.1054 $\pm$ 0.0084	(7) 8.1087 $\pm$ 0.0076	(8) 8.1734 $\pm$ 0.011	(8) 8.1094 $\pm$ 0.014	(8) 8.1094 $\pm$ 0.014	(8) 8.0094 $\pm$ 0.017	(8) 8.0094 $\pm$ 0.017	(8) 8.0094 $\pm$ 0.017	(8) 8.0094 $\pm$ 0.017	(8) 8.0094 $\pm$ 0.017
$S_{6,3y}$								(8) 25.6 $\pm$ 2.5	(8) 35.5 $\pm$ 3.3	(8) 35.5 $\pm$ 3.3	(8) 35.5 $\pm$ 3.3	(8) 35.5 $\pm$ 3.3
								(8) 29.0 $\pm$ 4.7	(8) 37.3 $\pm$ 2.7	(8) 37.3 $\pm$ 2.7	(8) 37.3 $\pm$ 2.7	(8) 37.3 $\pm$ 2.7

**Notes.** For example, signal  $S_{11y}$  is detected in sample Rmonthly2000 (Column 2). Rank="(1)" means that this  $S_{11y}$  signal is strongest of all six signals (DCM-manual: Table 6). Signal  $S_{11y}$  has period  $P = 11.0324 \pm 0.0048$  and peak to peak amplitude  $A = 98.8 \pm 2.6$ .

---

- Monthly and yearly data
- Non-weighted and weighted data
- Pure sine and double wave models
- All data samples and their subsets: predictive data samples

The  $S_{11y}$  signal is detected first in every sample. The critical levels for the all other signal detections<sup>4</sup> are  $Q_F < 10^{-16}$  (DCM-manual: Tables 6-17). Therefore, all signal detections are extremely significant, unless the  $S_{11y}$  signal itself is an artefact. The two strongest detected signals in all samples are the  $S_{11y}$  and  $S_{10y}$  signals, and always in this order.

## 5. Discrete Fourier Transform (DFT) cross-check

Zhu and Jia (2018) applied the Discrete Fourier Transform (DFT) to the daily sunspot number data from WDC SILSO (Royal Observatory of Belgium, Brussels). They used the DFT version formulated by Horne and Baliunas (1986). DFT searches for the best pure sine model for the data. Here, we cross-check if a similar DFT analysis of our monthly sunspot number sample  $R_{\text{monthly}}$  gives the same results as our pure sine model DCM analysis (Table 6: Column 3). Before our cross-check, we perform DCM and DFT analysis of simulated data.

### 5.1. DFT detection of two pure sine signals

In these simulations, we compare the performance of DFT and DCM. Let us assume that the data contains the sum signal  $s(t) = s_1(t) + s_2(t)$  of two pure sine signals

$$s_1(t) = a_1 \sin(2\pi f_1 t) \quad (33)$$

$$s_2(t) = a_2 \sin(2\pi f_2 t), \quad (34)$$

where the frequencies fulfil  $f_1 \approx f_2$ . DFT can detect both of the  $s_1(t)$  and  $s_2(t)$  signals, if

$$\Delta f = |f_2 - f_1| \gtrsim f_0, \quad (35)$$

where  $f_0 = 1/\Delta T$  is the distance between independent frequencies (Loumos and Deeming, 1978). We give the  $f/f_0 = \Delta T/P$  ratios for the  $S_{11y}$ ,  $S_{10y}$ ,  $S_{10.y6}$  and  $S_{11.y86}$  signals in Table 7. The  $S_{10y}$  and  $S_{10.y6}$  signal frequencies fulfil the criterion of Equation 35 only in the two longest  $R_{\text{yearly}}$  and  $R_{\text{yearly2000}}$  samples. This criterion is not fulfilled in our DFT cross-check  $R_{\text{monthly}}$  sample (Table 7). Furthermore, many pairs of  $S_{11y}$ ,  $S_{10y}$ ,  $S_{10.y6}$  and  $S_{11.y86}$  signals detected in this sample  $R_{\text{monthly}}$  have frequency differences  $\Delta f$  close to  $1 \times f_0$ .

The interference pattern of the sum  $s(t)$  of the two signals  $s_1(t)$  and  $s_2(t)$  is repeated during the beat period  $P_{\text{beat}} = |P_1^{-1} - P_2^{-1}|^{-1} = |f_1 - f_2|^{-1}$ . The solutions for the frequency, the amplitude and the phase of this sum signal  $s(t)$  are quite complex (Feth, 1974; Aguilar et al., 2012; Rutkowski, 2014; Schwär, Müller, and Schlecht, 2023). For the purposes of our DFT cross-check, it suffices to discuss the frequency  $f(t)$  and the phase  $\phi$  changes of the sum signal  $s(t)$ .

The frequency  $f(t)$  of the  $s(t)$  sum signal is constant

$$f(t) = (f_1 + f_2)/2, \text{ if } a_1 = a_2. \quad (36)$$

---

<sup>4</sup>The highest achievable accuracy for the computational `f.cdf` subroutine in `scipy.optimize` python library is  $10^{-16}$ .

**Table 7.** Independent frequency limitation (Equation 35). Ratios  $f/f_0 = \Delta T/P$  in order of decreasing sample time interval  $\Delta T$ . Arrows above numerical values indicate cases where  $\Delta f < f_0$ .

Sample	$\Delta T$ (y)	$S_{10y}$ $\Delta T/P$ (-)	$S_{10,y6}$ $\Delta T/P$ (-)	$S_{11y}$ $\Delta T/P$ (-)	$S_{11,y86}$ $\Delta T/P$ (-)
Ryearly	321.0	32.10	30.28	29.18	27.07
Ryearly2000	299.0	29.90	28.21	27.18	25.21
Rmonthly	273.8	27.38	25.83	24.89	23.09
Rmonthly2000	250.9	25.09	23.67	22.81	21.16
Cmonthly	204.8	20.48	19.32	18.62	17.27
Cyearly	203.0	20.30	19.15	18.45	17.12
Cmonthly2000	181.9	18.19	17.16	16.54	15.34
Cyearly2000	181.0	18.10	17.07	16.45	15.25

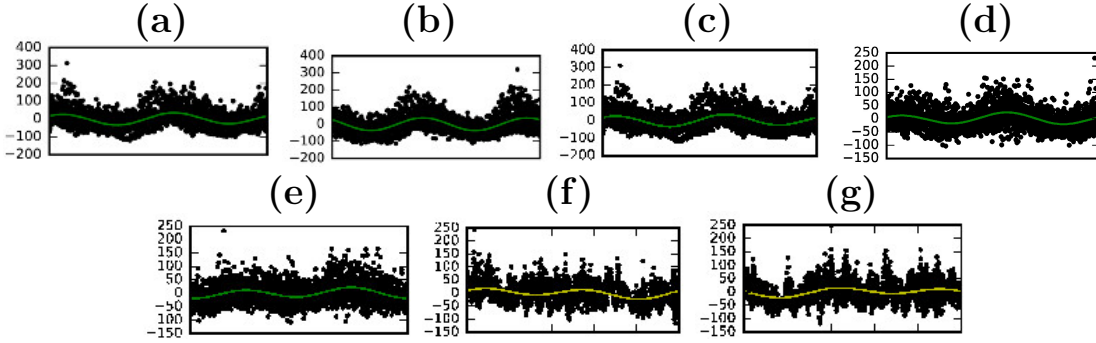


**Figure 1.** Double sinusoids $^{2\times}$  (Table 6). (a) Cmonthly:  $S_{11y}$  signal period  $21.667 \pm 0.014 = 2 \times (10.834 \pm 0.007)$ . (b) Rmonthly:  $S_{10y}$  signal period  $20.0062 \pm 0.0088 = 2 \times (10.0031 \pm 0.0044)$ . (c) Rmonthly2000:  $S_{11,y86}$  signal period  $23.686 \pm 0.018 = 2 \times (11.843 \pm 0.009)$ . (d) Rmonthly2000:  $S_{8,y4}$  signal period  $16.781 \pm 0.034 = 2 \times (8.390 \pm 0.017)$ . (e) Rmonthly:  $S_{8,y4}$  signal period  $16.753 \pm 0.027 = 2 \times (8.376 \pm 0.014)$ . (f) Rmonthly2000:  $S_{66y}$  signal period  $136.43 \pm 0.99 = 2 \times (68.22 \pm 0.50)$ . (g) Rmonthly:  $S_{66y}$  signal period  $143.39 \pm 0.99 = 2 \times (71.70 \pm 0.50)$ . Numbers and labels for x-axis phases  $\phi$  between 0 and 1 are missing, because these figures are extracts from larger figures, like Figure 3 in the DCM-manual. Period units are years. Figure units are x-axis  $[\phi]$  = dimensionless and y-axis  $[y]$  = dimensionless.

This frequency  $f(t)$  varies between the lower and upper limits given below

$$f_2 - \frac{a_1(f_1 - f_2)}{a_2 + a_1} \leq f(t) \leq f_2 + \frac{a_1(f_1 - f_2)}{a_2 + a_1}, \text{ if } a_2 > a_1. \quad (37)$$

In this case, the  $f(t)$  frequency changes are dominated by the stronger  $f_2$  signal.

The sum signal  $s(t)$  amplitude  $a_s$  is constantly changing. An abrupt instantaneous phase shift

$$\Delta\phi = [\arcsin(a_1/a_2)]/\pi \quad (38)$$

occurs at the epoch of  $a_s$  minimum. This shift is the largest,  $\Delta\phi = 0.5$ , for equal amplitudes  $a_1 = a_2$ .

The limitation of Equation 35 can *prevent* the DFT detection of both  $f_1$  and  $f_2$  values. The effects of Equations 36, 37 and 38 can *mislead* the DFT detection of the correct  $f_1$  and  $f_2$  values.

The units of time intervals and periods in all our simulations are years. The amplitude unit is dimensionless. These units are therefore no longer mentioned in the simulations below. We simulate  $y_i^*$  data, where the monthly sunspot number time points  $t_i^*$  are computed for four alternative time intervals of  $\Delta T = 70, 90, 110$  and  $274$ . These time intervals begin from the year 1749 at the beginning of sample **Rmonthly**. The longest  $\Delta T = 274$  simulation has the same time span and the same time points as **Rmonthly**. The  $s_1(t_i^*)$  and  $s_2(t_i^*)$  signal periods are  $P_1 = 1/f_1 = 10$ ,  $P_2 = 1/f_2 = 11$ . They are equal to the periods of the two strongest  $S_{10y}$  and  $S_{11y}$  signals detected in sample **Rmonthly**. This gives the beat period  $P_{\text{beat}} = 110$ . We simulate data for two alternative amplitude combinations  $a_1 = a_2 = 50 \Rightarrow f(t) = \text{constant}$  (Equation 36) and  $a_1 = 25 < a_2 = 50 \Rightarrow f(t) = \text{variable}$  (Equation 37). Hence, the total number of simulated samples is  $4 \times 2 = 8$ . The tested period interval between 5 and 200 years is the same as in our earlier DCM analysis of **Rmonthly** sample.

For the **Rmonthly** sample, the DCM five pure sine signal  $\mathcal{M}=5$  model gives the residuals  $\epsilon_i$ , which have a standard deviation  $s_\epsilon = 42$ . We assume that after the detection of these five pure sine signals, these remaining  $\epsilon_i$  residuals represent the noise in the original data. Therefore, the errors  $\sigma_i^*$  for the simulated data are drawn from a Gaussian distribution having a mean  $m = 0$  and a standard deviation  $s = s_\epsilon = 42$ . The simulated data are

$$y_i^* = m^* + s_1(t_i^*) + s_2(t_i^*) + \sigma_i^*, \quad (39)$$

where  $m^* = 81.6$  is the mean of all  $y_i$  values in **Rmonthly**. The selected  $m^*$  value has no impact on our results, because it is subtracted from the simulated  $y_i^*$  data before the computation of DFT periodogram. The DCM two sine wave model  $\mathcal{M}_{2,1,0,R}$  solves this  $M_0 = m^*$  value.

We analyse the  $2 \times 4 = 8$  simulated data samples using the same DFT approach as Zhu and Jia (2018). They used the pre-whitening technique, where DFT detects one signal at the time (Scargle, 1982; Reegen, 2007). We apply DFT to the original simulated data. This gives us the first  $P_1$  period. The least squares fit is then made to the original simulated data, where the pure sine model has the  $P_1$  period. This “first DFT model” gives the first sample of residuals. DFT is applied to this first sample of residuals, which gives the second  $P_2$  period. The next least squares fit is made to the first sample of residuals using a pure sine model having a period  $P_2$ . The model for this sample is called “the second DFT model”. This gives the second sample of residuals.

The DFT pre-whitening technique has its limitations. The DFT *can only* be used to cross-check the DCM pure sine model analysis results for non-weighted data. DFT *can not* be used to cross-check the DCM double wave model analysis results, nor the DCM weighted data analysis results.

In the next Sections 5.2 and 5.3, we perform the DCM and DFT analyses of the  $2 \times 4 = 8$  simulated data samples, and compare the results. The results for each individual simulated sample are presented in one vertical column of Figures 2 and 3, where the dashed vertical lines intersecting the periodograms denote the *simulated frequencies*  $1/P_1 = 1/10$  and  $1/P_2 = 1/11$ . The diamonds at the DFT periodogram maxima and the DCM periodogram minima denote the *detected frequencies*. Hence, the vertical dashed lines intersect the diamonds only if the method detects the correct frequencies.

## 5.2. Results for two equal amplitude signals

We present the results for equal amplitudes  $a_1 = a_2 = 50$  in Figure 2.

The results for the shortest simulated time interval,  $\Delta T = 70$ , are shown in Figures 2a-2f. The DFT periodogram  $z_{\text{DFT}}(f)$  shows only one peak at  $P_1 = 10.44$  (Figure 2a). The limitation of Equation 35 prevents the detection of two peaks. The effect  $[(f_1 + f_2)/2]^{-1} = 10.48$  (Equation 36) explains the detected wrong period  $P_1 = 10.44$  value. The first DFT model residuals have

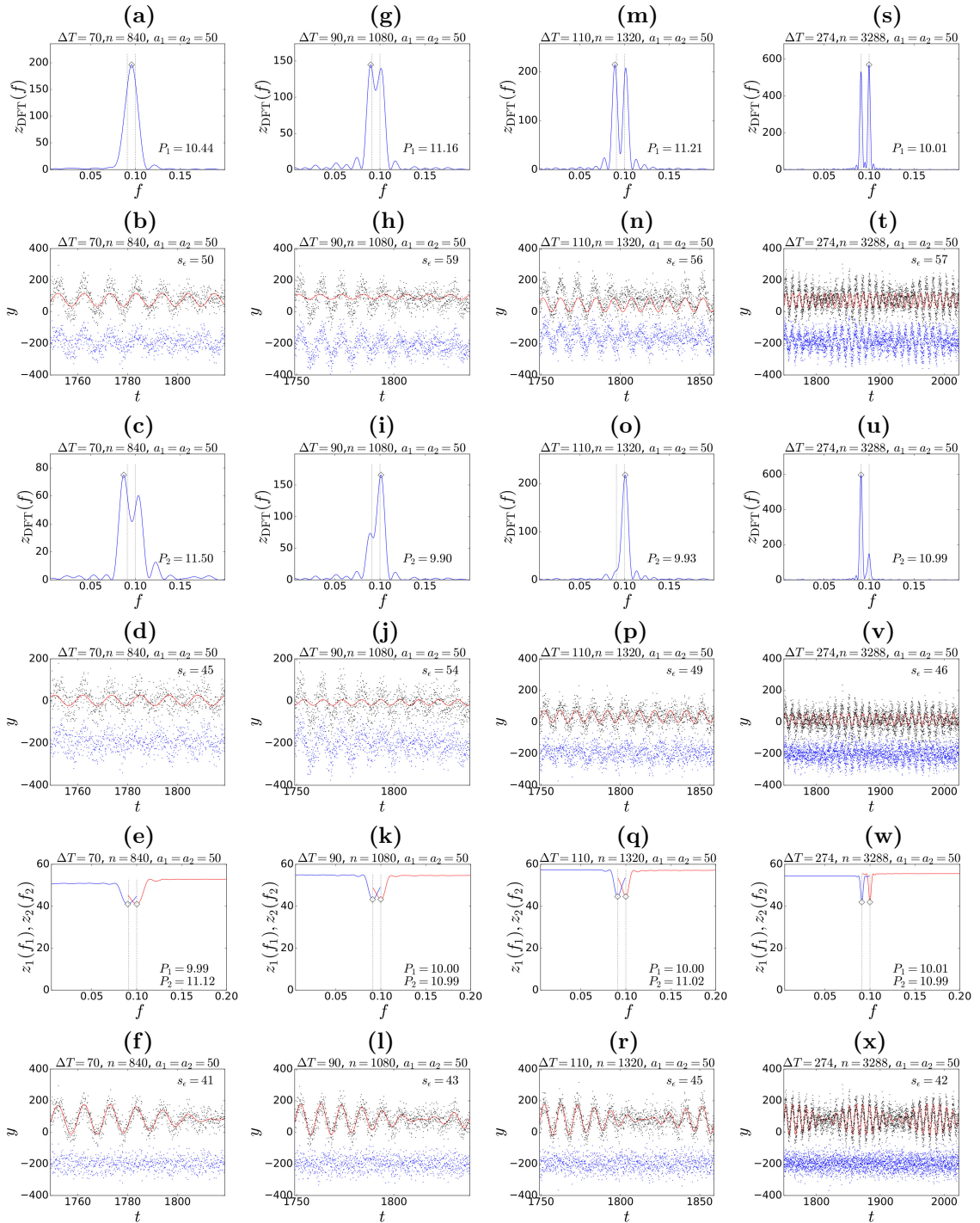


**Figure 2.** Equal amplitude  $a_1 = a_2 = 50$  simulations for signal periods  $P_1 = 10$  and  $P_2 = 11$  (Equations 33 and 34). (a) DFT periodogram  $z_{\text{DFT}}(f)$ . Period  $P_1 = 10.44$  is detected from  $y_i^*$  data simulated with  $n = 840$ ,  $\Delta T = 70$ ,  $P_1 = 10$ ,  $a_1 = 50$ ,  $P_2 = 11$  and  $a_2 = 50$ . Units are  $[f] = 1/y$  and  $[z_{\text{DFT}}] = \text{dimensionless}$ . Vertical dashed black lines denote locations of simulated frequencies  $f_1 = 1/P_1$  and  $f_2 = 1/P_2$ . Diamond denotes location of detected frequency. (b) Model for simulated data. Black dots denote simulated  $y_i^*$  data. Red curve denotes pure sine model having period  $P_1 = 10.44$ . Black dots denote  $\epsilon_i$  residuals offset to level -200. Standard deviation of residuals is  $s_\epsilon = 50$ . Units are  $[t] = \text{year}$  and  $[y] = [\epsilon] = \text{dimensionless}$ . (c-d) DFT results for first sample of residuals. Otherwise as in a-b. (e) DCM periodograms  $z_1(f_1)$  and  $z_2(f_2)$ . Periods  $P_1 = 9.99$  and  $P_2 = 11.12$  are detected from  $y_i^*$  data simulated with  $n = 840$ ,  $\Delta T = 70$ ,  $P_1 = 10$ ,  $a_1 = 50$ ,  $P_2 = 11$  and  $a_2 = 50$ . Diamonds denote locations of detected frequencies. Units are  $[f] = 1/y$  and  $[z_1] = [z_2] = \text{dimensionless}$ . (f) Model for simulated data. Black dots denote simulated  $y_i^*$  data. Red curve shows two pure sine signal DCM model. Blue dots denote  $\epsilon_i$  residuals offset to level -200. Standard deviation of residuals is  $s_\epsilon = 41$ . Units are  $[t] = \text{year}$  and  $[y] = [\epsilon] = \text{dimensionless}$ . (g-l) Data simulated for longer time interval  $\Delta T = 90$ . Otherwise as in a-f. (m-r) Data simulated for longer time interval  $\Delta T = 110$ . Otherwise as in a-f. (s-x) Data simulated for longer time interval  $\Delta T = 274$ . Otherwise as in a-f.

a standard deviation  $s_\epsilon = 50$ , and show regular periodic variation (Figure 2b). The DFT periodogram for these residuals shows the highest peak at  $P_2 = 11.50$  (Figure 2c). The second DFT model residuals have a standard deviation of  $s_\epsilon = 45$  and show some regular periodic variation (Figure 2d). DCM detects the  $P_1 = 9.99$  and  $P_2 = 11.12$  periods, which are close to, but not exactly equal to the simulated 10 and 11 values (Figure 2e). The DCM model residuals show no periodic variation and follow a straight line (Figure 2f). This residual distribution resembles a random distribution. The DCM model residuals  $s_\epsilon = 41$  standard deviation is much smaller than the DFT model residuals  $s_\epsilon = 45$  standard deviation. In this  $\Delta T = 70$  simulation, DFT fails and DCM succeeds.

Both DFT periodograms are double-peaked in the longer  $\Delta T = 90$  simulation (Figures 2g and 2i). DFT detects the  $P_1 = 11.16$  and  $P_2 = 9.90$  periods, which are closer to the simulated values. The residuals of both DFT models show periodic variability (Figures 2h and 2j). The mean residual  $s_\epsilon = 59$  and 54 values are larger than in the earlier shorter  $\Delta T = 70$  simulation, because there is a  $\Delta\phi = 0.5$  phase shift (Equation 38) in the simulated  $y_i^*$  data at the year 1804. DCM detects the correct  $P_1 = 10.00$  and  $P_2 = 10.99$  periods (Figure 2k). The distribution of DCM model residuals resembles that of a random distribution, and there is no periodic variability (Figure 2l). The  $s_\epsilon = 43$  value of DCM model is much smaller than the  $s_\epsilon = 54$  value of DFT model, because the DCM can handle the  $\Delta\phi = 0.5$  phase shift (Equation 38). Again, DCM performs better than DFT.

In the next  $\Delta T = 110$  simulation, the criterion of Equation 35 is fulfilled, and therefore the first DFT periodogram is clearly double-peaked (Figure 2m). DFT detects the  $P_1 = 11.21$  and  $P_2 = 9.93$  periods, which differ from the simulated periods. Both DFT model  $s_\epsilon = 56$  and 49 mean residual values are large (Figures 2n and 2p). These DFT residuals show periodic variability. DCM detects the correct  $P_1 = 10.00$  and  $P_2 = 11.02$  periods (Figure 2q). The distribution of DCM model residuals appears random, and its standard deviation is  $s_\epsilon = 45$  (Figure 2r). The abrupt phase shift in the simulated  $y_i^*$  data (Equation 38) at the year 1804 misleads DFT, but it does not mislead DCM.

Two abrupt phase shifts, in the years 1804 and 1914, occur in the last  $\Delta T = 274$  simulation (Equation 38). Finally, DFT succeeds in finding the correct  $P_1 = 10.01$  and  $P_2 = 10.99$  periods (Figures 2s and 2u). However, the residuals of both DFT models still show periodic variability (Figures 2t and 2v). DCM detects the correct  $P_1 = 10.01$  and  $P_2 = 10.99$  periods (Figures 2w). The DCM model residuals show no periodic variability, and their distribution resembles a random distribution (Figures 2x). The standard deviation  $s_\epsilon = 46$  of the DFT model clearly exceeds the  $s_\epsilon = 42$  value of DCM model. In short, DCM performs better than DFT.

### 5.3. Results for two unequal amplitude signals

We present the results for unequal amplitudes  $a_1 = 25$  and  $a_2 = 50$  in Figure 3.

All details are not discussed, as in the case of Figure 2. We concentrate only on the general results in Figure 3, because they are the same for all  $\Delta T = 70, 90, 110$  and 274 simulations.

If the relation of Equation 35 is not fulfilled, DFT can not detect the correct period values, but DCM can. If this relation is fulfilled, DFT can also succeed.

The relation of Equation 37 predicts that the frequency  $f_2 = 1/P_2 = 1/11$  of the stronger signal dominates in the frequency  $f(t)$  of the  $s(t)$ . Therefore, DFT always detects this  $P_2 = 11$  period signal first. DCM detects both signals simultaneously, neither one of them being “the first”.

DFT can not model the amplitude changes or the abrupt phase shifts (Equation 38). For this reason, the DFT model residuals always show periodic variability, while the DCM model residuals do not. DCM residuals have a random distribution concentrated on a straight line,

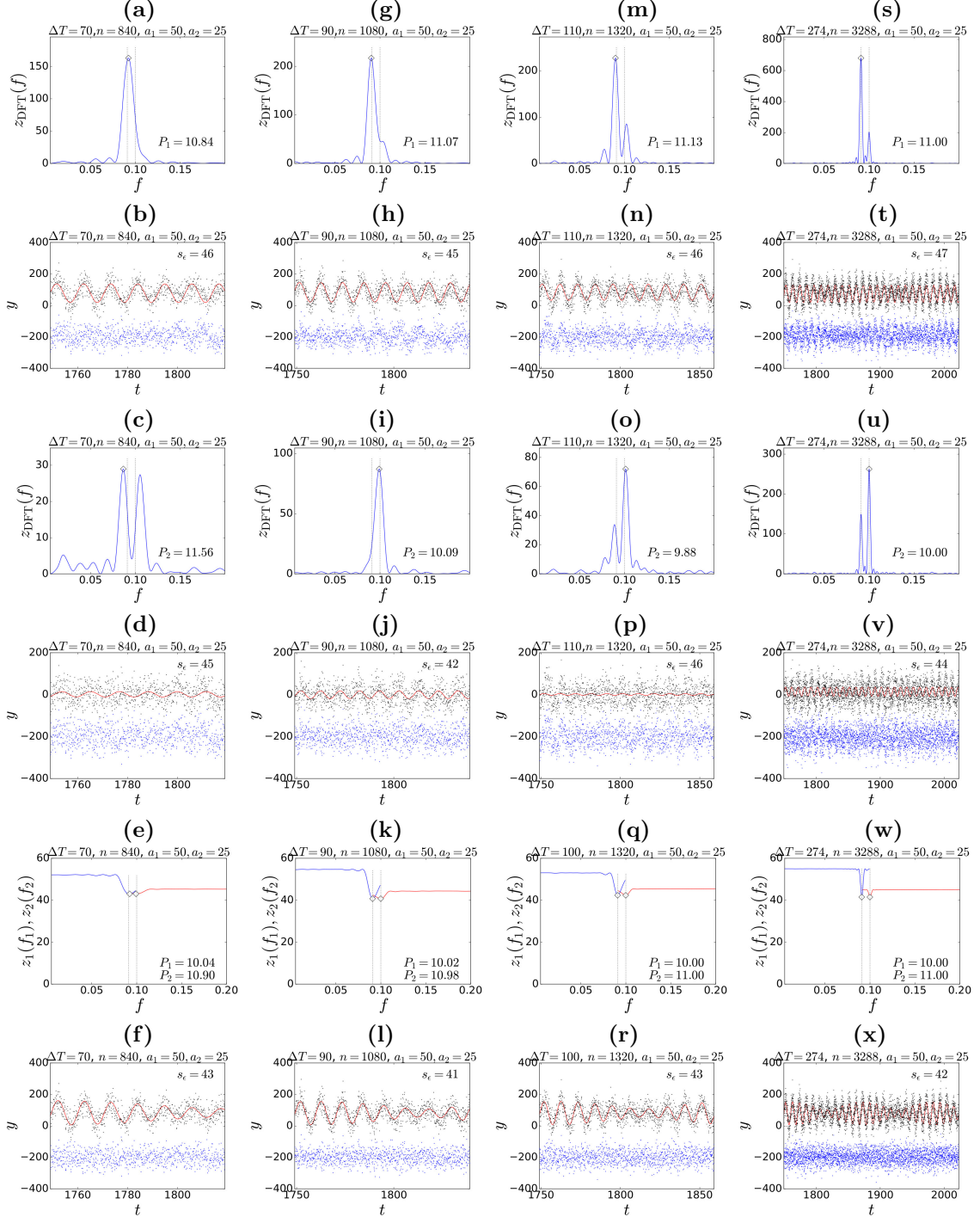


**Figure 3.** Unequal amplitude  $a_1 = 25$  and  $a_2 = 50$  simulations for signal periods  $P_1 = 10$  and  $P_2 = 11$  (Equations 33 and 34). Otherwise as in Figure 2.

which is a signature of a good model. DFT model  $s_\epsilon$  values are always larger than DCM model  $s_\epsilon$  values. This means that some information is always lost at every DFT pre-whitening stage, where one pure sine signal is detected at the time. Both methods reach  $s_\epsilon$  levels that are close to the standard deviation  $s = 42$  of the random errors  $\sigma_i^*$ , which are added as noise to the simulated data (Equation 39). This means that both methods can also detect the second, weaker  $P_1 = 10$  signal, which has the peak to peak amplitude  $A_1 = 2a_1 = 50$  that has the same order of magnitude as  $s = 42$ . However, only DCM can reach this  $\sigma_\epsilon \approx s = 42$  level for all  $2 \times 4 = 8$  simulations.

#### 5.4. Discrete Fourier Transform (DFT) analysis of `Rmonthly`

We simulate data arising from the interference between two sine waves having frequencies  $f_1 \approx f_2$  (Equation 39). Our DFT and DCM analyses of these simulated data reveal the performance differences between these two methods. We encounter the same five DFT drawbacks for equal and unequal amplitude sine waves (Sections 5.2 and 5.3).

1. Detection of close frequencies: DFT suffers from the limitation of Equation 35, but DCM does not.
2. Wrong frequency detection: DFT suffers from the misleading effects of Equations 36 and 37, but DCM does not.
3. Abrupt phase shifts: DFT can not model the abrupt phase shifts of Equation 38, but DCM can.
4. Biased residuals: DFT pre-whitening model residuals do not have a random distribution, but DCM model residuals do. The mean residual  $s_\epsilon$  values of DFT models are always larger than those of DFT models, which means that some information is lost at every DFT pre-whitening stage.
5. Detection accuracy: The difference between the detected and the simulated period values is larger for DFT than for DCM. This difference decreases as the samples become longer. For real data, this means that DCM detects the correct period values more probably than DFT.

When DFT analysis fails, DCM analysis can succeed. We can safely state that DCM performs better than DFT. The two strongest  $S_{11y}$  and  $S_{10y}$  signals in the real data sample `Rmonthly` are exactly the same as in our simulations. When we use DFT pre-whitening to search for more than two signals in this real data sample `Rmonthly`, it is logical to assume that the above DFT drawbacks become more pronounced.

The DFT pre-whitening results for the sample `Rmonthly` are shown in Figure 4. The first five  $S_{11y}$ ,  $S_{10y}$ ,  $S_{11.y86}$ ,  $S_{110y}$  and  $S_{10.y6}$  signals detected using DFT pre-whitening (Figure 4 a-j) are the same as those detected using the five pure sine signal DCM model (Table 6: Column 3). The only minor difference is that DCM detects signal  $S_{10.y6}$  before signal  $S_{110y}$ . Both methods give nearly the same amplitudes for these five strongest signals. The sixth-strongest detected signals are different: the  $S_{53y}$  signal for DCM (Table 6: Column 3) and the  $S_{8.y4}$  signal for DFT (Figure 4 k-l). The seventh-strongest detected signals are also different, the  $S_{8y}$  signal for DCM and the  $S_{53y}$  signal for DFT. DCM detects only seven signals from sample `Rmonthly`, because the unstable  $M=8$  model is rejected (DCM-manual: Table 7, “UM”). DCM analysis of predictive data sample `Rmonthly2000`, which is a subsample of all data sample `Rmonthly`, indicates that the correct number of real signals is six (Section 6.2.2: Figure 6). We conclude that DCM and DFT detect the same five strongest signals from sample `Rmonthly`.

These five strongest signals are clearly connected to each other (Table 8). Their  $\pm 1$  round synodic period difference connections

$$P_\pm = [P_1^{-1} \pm P_2^{-1}]^{-1} \quad (40)$$

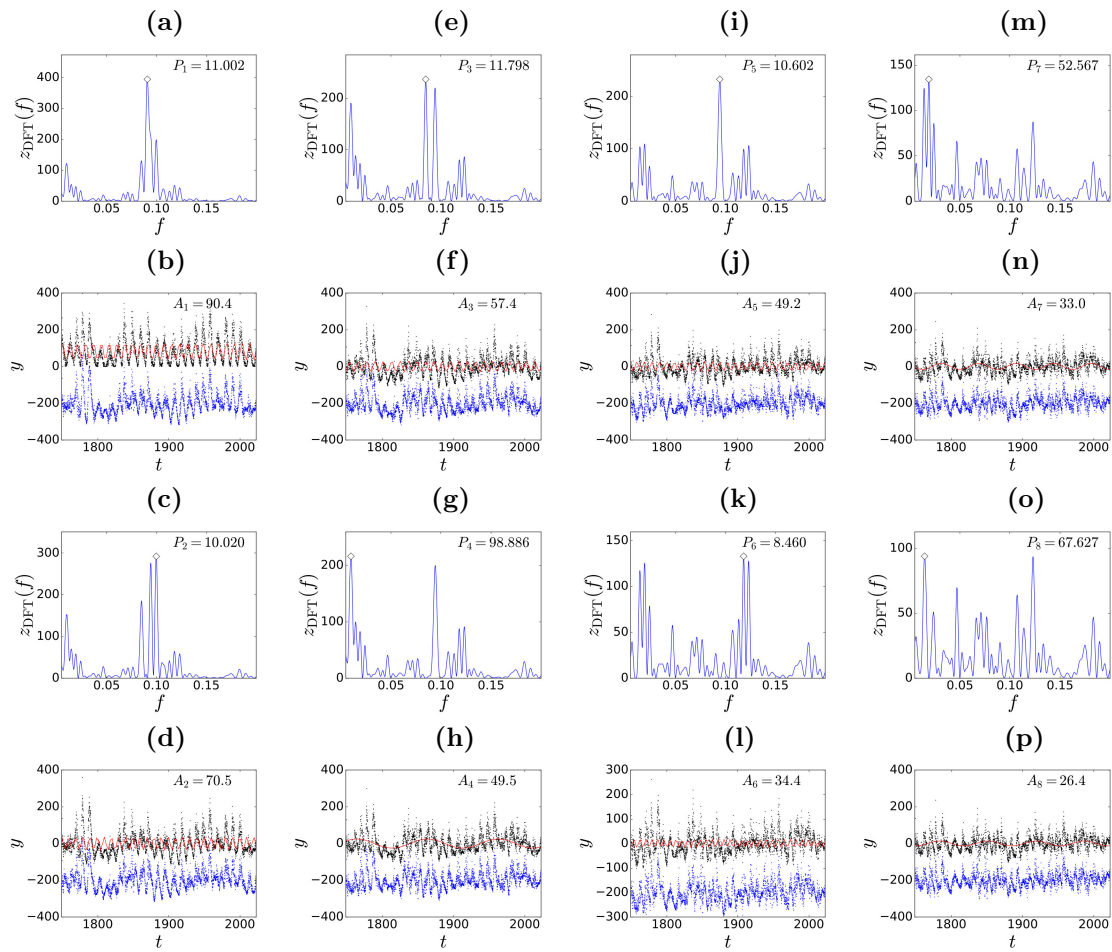


**Figure 4.** DFT pre-whitening analysis results for Rmonthly sample. (a) DFT periodogram for original data. Diamond denotes peak of periodogram at frequency of best period  $P_1 = 11.002$  years. Units are  $[f] = 1/y$  and  $[z_{DFT}] = \text{dimensionless}$ . (b) Pure sine model for original data. Black dots denote original  $y_i$  data. Red curve denotes sine model with period  $P_1 = 11.002$ . Its peak to peak amplitude is  $A_1 = 90.4$ . Blue dots denote residuals  $\epsilon_i$  offset to level -200. Units are  $[t] = \text{years}$  and  $[y] = [\epsilon] = [A] = \text{dimensionless}$ . (c-d) Second signal detected from first sample of residuals. (e-f) Third signal detected from second sample of residuals. (g-h) Fourth signal detected from next sample of residuals. (i-j) Fifth signal. (k-l) Sixth signal. (m-n) Seventh signal. (o-p) Eighth signal. Notations for all panel pairs from “c-d” to “o-p” are same as in panel pair “a-b”.

are given in Table 8. These five strongest signals can, and inevitably do, interact through these one round differences. This means that the interference of these five signals is repeated indefinitely.

It is essential to understand, why the DFT pre-whitening analysis of Rmonthly sample does succeed, regardless of all DFT drawbacks discussed above? The limitation of Equation 35 is encountered, because the difference between the  $S_{10,y6}$  and  $S_{11,y}$  signal frequencies is smaller than  $f_0$  (Table 7). All four  $S_{10,y}$ ,  $S_{10,y6}$ ,  $S_{11,y}$  and  $S_{11,y86}$  signal frequencies are closely packed within an interval of  $(27.38 - 23.09)f_0 = 4.29f_0$  independent frequencies. The interference of these four signals enhances the misleading effects of Equations 36 and 37. The amplitudes of  $S_{10,y}$ ,  $S_{10,y6}$  and  $S_{11,y86}$  signals are nearly equal. This causes many abrupt large  $\Delta\phi \approx 0.5$  phase shifts during  $\Delta T = 274$  (Equation 38). Nevertheless, the DFT pre-whitening analysis succeeds, because signal  $S_{11,y}$  amplitude  $A_1 = 90.4$  is crucially larger than signal  $S_{10,y}$ ,  $S_{10,y6}$  and  $S_{11,y86}$  amplitudes. As

**Table 8.** Synodic period connections. (1)  $P_1$  period. (2-5)  $P_2$  period. Next lines:  $P_{\pm}$  periods for  $P_1$  and  $P_2$  combinations (Equation 40). Signals  $S_{10y}$  and  $S_{11y}$  connect to signal  $S_{110y}$ . Signals  $S_{11,y86}$  and  $S_{110y}$  connect to signal  $S_{10,y6}$ . Signal  $S_{10,y6}$  has no direct connection to signals  $S_{10y}$  or  $S_{11y}$ .

(1)	(2)	(3)	(4)	(5)
	$P_2 = S_{10,y6}$	$P_2 = S_{11y}$	$P_2 = S_{11,y86}$	$P_2 = S_{110y}$
$P_1 = S_{10y}$	$P_- = 177$ $P_+ = 5.15$	$P_- = 110$ $P_+ = 5.24$	$P_- = 63.8$ $P_+ = 5.42$	$P_- = 11.0$ $P_+ = 9.17$
$P_1 = S_{10,y6}$		$P_- = 292$ $P_+ = 5.40$	$P_- = 99.8$ $P_+ = 5.60$	$P_- = 11.7$ $P_+ = 9.67$
$P_1 = S_{11y}$			$P_- = 152$ $P_+ = 5.71$	$P_- = 12.2$ $P_+ = 10.0$
$P_1 = S_{11,y86}$				$P_- = 13.3$ $P_+ = 10.7$

predicted by Equation 37, this  $S_{11y}$  signal is detected first. After the pre-whitening subtraction of this strongest signal, the remaining  $S_{10y}$ ,  $S_{10,y6}$  and  $S_{11,y86}$  signals no longer suffer from the  $f_0$  limitation of Equation 35. The two highest amplitude  $A_2 = 70.5$  and  $A_3 = 57.4$  signals  $S_{10y}$  and  $S_{11,y86}$  are now “comfortably separated” by  $(27.38 - 23.09)f_0 = 4.29f_0$  independent frequencies. As predicted by the relation of Equation 37, these two signals are detected next (Figure 4c-f). The frequency difference between the remaining  $S_{10,y6}$  and  $S_{110y}$  signals is so large that DFT can easily detect them. Our DFT pre-whitening analysis of sample **Rmonthly** succeeds, because one strong  $S_{11y}$  signal dominates, and the remaining signals are detected in a suitable order. This successful DFT analysis also confirms that the data does not contain any misleading long-term trends.

Our Table 9 gives the significance estimates for the DCM and DFT period detections from the **Rmonthly** sample. The DCM gives no direct significance estimate for the first detected 11.032 year period, which has certainly been detected for more than million times from the sunspot data. The DCM detections for the next six periods are extremely significant because the Fisher-test always rejects the  $H_0$  hypothesis at critical levels  $Q_F < 10^{-16}$  (Equation 28). The DCM model for the eighth 8.456 year period is unstable (DCM-manual: Table 7,  $\mathcal{M}=8$ ).

For the DFT analysis, our Table 9 gives the values for the term

$$E_{\text{DFT}} = e^{-(n/2)(1+\xi^{-1})^{-1}}, \quad (41)$$

which is used to compute the false alarm probability  $Q_{\text{DFT}}$  (Horne and Baliunas, 1986, their Equation 22). All  $E_{\text{DFT}}$  values are so close to zero that all false alarm probabilities  $Q_{\text{DFT}}$  are practically equal to zero, which means that all DFT period detections are extremely significant.

Unless the solar cycle, the first detected 11 year signal, is an artefact, the DCM detections of all other signals are extremely significant ( $Q_F < 10^{-16}$ ). In short, all DCM and DFT period detections in Table 9 are absolutely certain, if the data contain only white noise. One could argue that our significance estimates can be unreliable because we do not consider the possibility that the data contains red noise (Vaughan, 2005). We test the  $H_0$  hypothesis in our DCM analysis with the Fisher-method (Equation 28). If the data contained red noise, it would influence both the simple model and the complex model of the Fisher-test. Hence, our the DCM analysis results are correct with or without the red noise. We admit that the red noise could contaminate our

**Table 9.** Significance estimates for DCM and DFT period detections from `Rmonthly` sample. (1) Detection order. (2) DCM period  $P$ . (3) DCM critical level  $Q_F$  (Equation 28). (4) DFT period  $P$ . (5) DFT term  $E_{DFT}$  (Equation 41). (6) DFT false alarm probability  $Q_{DFT}$  (Horne and Baliunas, 1986, their Equation 22).. Note that DCM model for period 8.456 is unstable (“UM”).

(1)	DCM		DFT		
	$P$	$Q_F$	$P$	$E_{DFT}$	$Q_{DFT}$
	(2)	(3)	(4)	(5)	(6)
(-)	(y)	(-)	(y)	(-)	(-)
1	11.0324	—	11.002	$1.8 \times 10^{-162}$	0
2	10.0001	$<10^{-16}$	10.020	$5.5 \times 10^{-128}$	0
3	11.807	$<10^{-16}$	11.798	$1.7 \times 10^{-103}$	0
4	99.92	$<10^{-16}$	98.886	$1.7 \times 10^{-90}$	0
5	10.569	$<10^{-16}$	10.602	$4.0 \times 10^{-102}$	0
6	52.66	$<10^{-16}$	8.460	$2.2 \times 10^{-58}$	0
7	8.1087	$<10^{-16}$	52.567	$8.9 \times 10^{-59}$	0
8	8.456UM	$<10^{-16}$	67.627	$4.0 \times 10^{-41}$	0

DFT analysis significance estimates, but then again we detect the same periods with the DCM and the DFT. For some reason, the extreme significance estimates for the DFT period detections from the sunspot data have not caught the attention that they would have deserved in the earlier studies (e.g. Zhu and Jia, 2018).

We conclude that the DCM and DFT detect the same periods from the sunspot data. Both methods give extreme significance estimates. These period detections are absolutely certain.

## 6. Predictions

The two alternative theories for the origin of the sunspot cycle are the stochastic solar-dynamo-theory and the deterministic planetary-influence-theory. The easiest way to refer to these two alternative theories is to formulate these hypotheses:

$H_{\text{Dynamo}}$ : “*The solar dynamo is a stochastic process. Therefore, deterministic sunspot number predictions longer than one solar cycle fail.*”

$H_{\text{Planet}}$ : “*Planetary motions are deterministic. Therefore, deterministic sunspot number predictions longer than one solar cycle can succeed.*”

### 6.1. Solar Cycle Prediction Panel prediction

It is crucial to check what level of predictability has already been reached. In the year 2019, the Solar Cycle Prediction Panel representing NOAA, NASA and the International Space Environmental Services (ISES) made the official forecast for solar cycle 25. The red curve in Figure 5 shows the synthesis of about 50 different forecasts received from the scientific community. During the current sunspot cycle 25, the maximum difference between the smoothed monthly sunspot number and the predicted values has been

$$s_{\text{ISES}} = \pm(117.0 - 66.3) \approx \pm50 \quad (42)$$

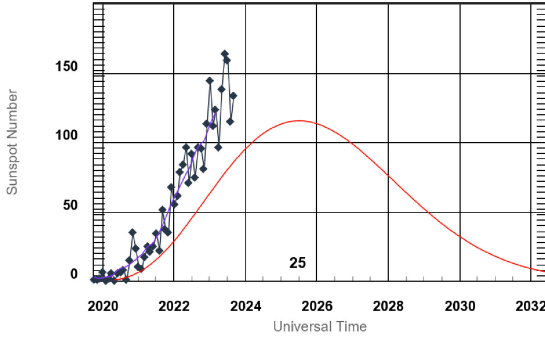


**Figure 5.** Solar Cycle Prediction Panel forecast for solar cycle 25. Red curve shows predicted monthly sunspot numbers after December 2019. Grey shaded area shows prediction error. Black curve denotes observed monthly sunspot number up to September 2024. Blue line denotes observed smoothed 13 months mean.

on March 2024.<sup>5</sup> This gives an estimate for the accuracy that could be achieved in sunspot number predictions for the past four years after 2019. We do not argue that this is the best achievable accuracy, but this is the current best official published forecast. However, this accuracy would certainly be worse if this forecast covered more than one solar cycle. The  $s_{\text{ISES}}$  parameter of Equation 42 is hereafter referred as the four year “ISES limit”. If our model prediction deviates less than  $s_{\text{ISES}}$  from the predicted observations, we state that the prediction is “within the ISES limit”. In such cases, our prediction deviates less than  $s_{\text{ISES}}$  from the the smoothed thirteen monthly sunspot data.

We evaluate predictivity  $z_{\text{pred}}$  for the six pairs of predictive and predicted data (Equation 30). The six all data samples are used to predict  $m_{\text{pred}}$  for the past prolonged activity minima (Equation 32). We use the red continuous and dotted lines to denote the model and the model errors, respectively. The sliding thirty years mean of this model and the sliding mean error are denoted with the green continuous and dotted curves. We will show many predictions extending to time intervals before and after the analysed samples (Figures 6, 7, 8, 9 and 10). The thirty years sliding mean predictions are always more accurate than the model predictions (Figures 6-10: red curves). Therefore, the green curve errors (dotted green lines) are always smaller than the red curve errors (dotted red lines). The red model curve predictions are shown only for the first few cycles after the newest, most accurate sunspot data. Since the oldest sunspot data are sparse and inaccurate, we show no red curve predictions before these data. The thirty years sliding mean green curve predictions are shown for the time intervals before and after the sunspot data. To ensure easy readability of all Figures 6-10, we surround the realm of our predictions with black dash-dotted rectangles. We also use long black horizontal arrows to highlight the direction of these predictions in time. The dash-dotted cyan lines in all model residuals  $\epsilon_i$  plots denote the four year ISES limits  $\pm s_{\text{ISES}}$  (Equation 42).

## 6.2. Non-weighted monthly sunspot data

### 6.2.1. Pure sines

Sample `Rmonthly2000` contains the predictive data. The predicted data are the `Rmonthly` sample observations after the year 2000. The whole `Rmonthly` sample represents all data.

<sup>5</sup>Space Weather Prediction Center on October 2nd, 2024.

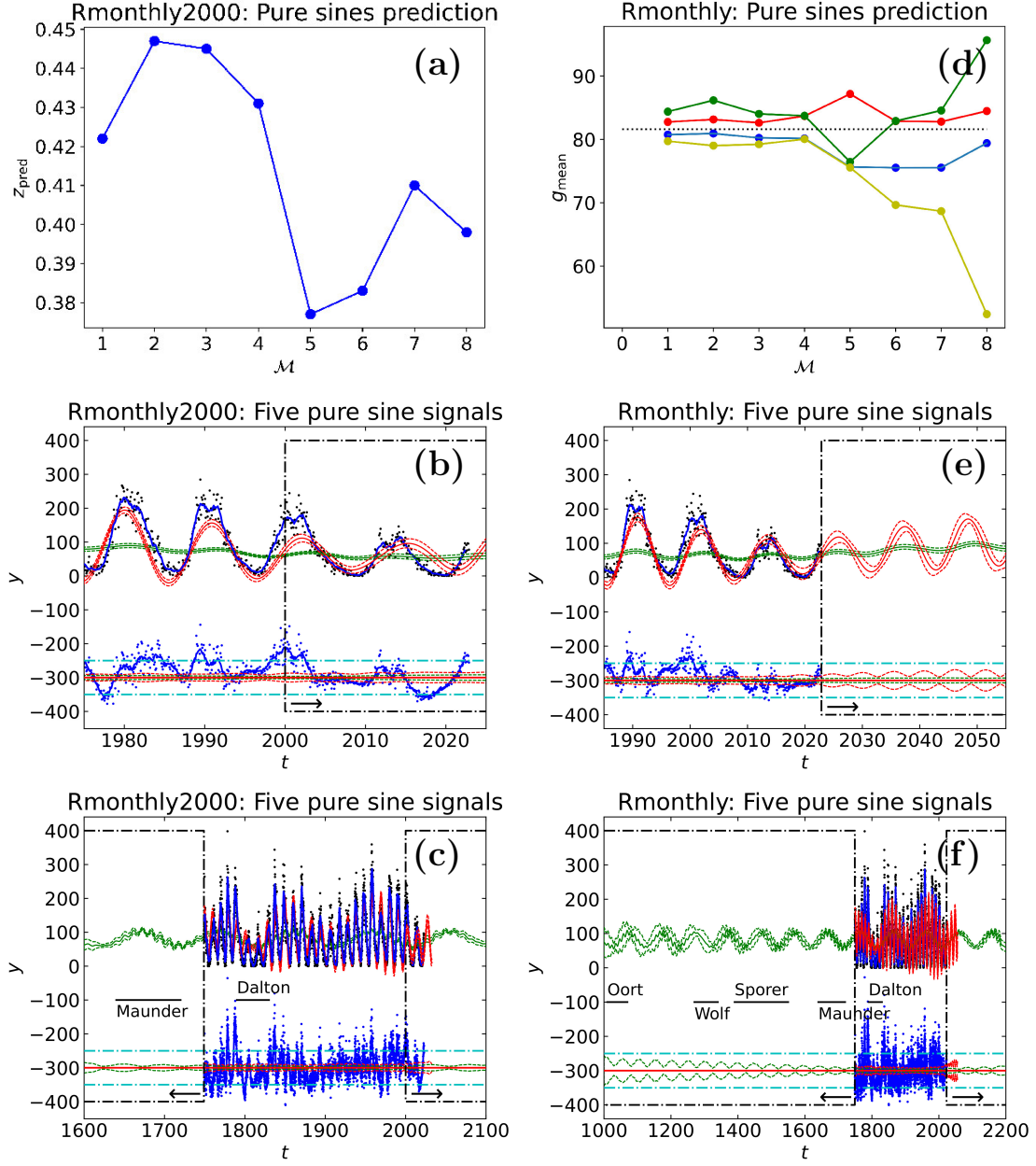


**Figure 6.** (a) Rmonthly2000 predictions for pure sines (DCM-manual: Table 6). (a) Predicted test statistic  $z_{\text{pred}}$  (Equation 30) for pure sine models  $M=1\text{--}8$ . Best model  $M=5$  minimises  $z_{\text{pred}}$ . Units are x-axis  $[M]=\text{dimensionless}$  and y-axis  $[z_{\text{pred}}]=\text{dimensionless}$ . (b) Black dots denote data  $y_i$ . Blue continuous line denotes 13 month smoothed data. Red continuous line denotes  $g(t)$  model  $M=5$ . Dotted red lines denote  $\pm 3\sigma$  model error limits for  $g(t)$ . Green continuous line denotes model  $g(t)$  thirty years sliding mean. Dotted green lines show  $\pm 3\sigma$  error limits for this sliding mean. Predictive data ends at vertical dash-dotted black line. Predicted data, predicted model and predicted thirty years mean are surrounded by this black dash-dotted line. Black arrow shows prediction direction in time. Blue dots denote residuals  $\epsilon_i$  offset to level -300, which is outlined with red continuous line. Dash-dotted cyan lines denote ISES prediction SIES error limit (Equation 42). Units are x-axis  $[t]=\text{years}$  and y-axis  $[y]=\text{dimensionless}$ . (c) Horizontal black continuous lines outline time intervals of Dalton and Maunder minima. Except for a longer time span, otherwise as in “b”. (d) Rmonthly predictions for pure sines (DCM-manual: Table 7): Predicted mean level  $m_{\text{pred}}$  (Equation 32) for pure sine  $M=1\text{--}8$  models during Maunder (red), Sporer (blue), Wolf (green) and Oort (yellow) minima. Dotted black line shows the mean  $m=81.6$  for all  $y_i$  data. Units are x-axis  $[M]=\text{dimensionless}$  and y-axis  $[m_{\text{pred}}]=\text{dimensionless}$ . (e)  $M=5$  model for modern times and its prediction after year 2022. Otherwise as in “b”. (f)  $M=5$  model for long-term past and future. Otherwise as in “c”

The smallest predicted test statistic  $z_{\text{pred}}$  (Equation 30) value is achieved for the five pure sines  $\mathcal{M}=5$  model (Figure 6a). Predictability is better for one signal than for two signals. Then, this  $z_{\text{pred}}$  predictability improves for three, four and five signals. This  $z_{\text{pred}}$  improvement trend indicates that these five first signals are deterministic, not stochastic. Six signals give nearly the same predictability. For more than six signals, predictability becomes worse. Furthermore, the seven and eight signal models are unstable (DCM-manual: Table 6, “UM” models  $\mathcal{M}=7$  and 8). We compute  $z_{\text{pred}}$  values also for these unstable models, just to verify, if predictability stops improving due to instability.

For the predictive `Rmonthly2000` data sample, the five signal prediction after 2000 succeeds quite well until a clear deviation from the data occurs in the year 2013 (Figure 6b). Most of the blue dots denoting the predictive model residuals are within the horizontal cyan dash dotted lines of ISES limit (Equation 42).

The five pure sines model can reproduce the Dalton minimum because it is inside the predictive data (Figure 6c). There is a dip at the end of the Maunder minimum, but the prediction for the duration of the Maunder minimum fails.

The DCM pure sine model analysis results for `Rmonthly` are given in the DCM-manual (Table 7). This all data sample gives the predicted mean level  $m_{\text{pred}}$  (Equation 32) values for the past activity minima. These predictions are not convincing (Figure 6d). Only the blue and yellow circles denoting Sporer and Oort minima are below the black horizontal dotted line denoting the mean level  $m = 81.6$  of all sunspot numbers. `Rmonthly` sample pure sines prediction indicates that the current prolonged low solar activity level has just ended (Figure 6e: green curve). The long-term past and future predictions are shown in Figure 6f.

### 6.2.2. Double waves

The predictive data sample is `Rmonthly2000`. All data sample is `Rmonthly`. The `Rmonthly` sample values after the year 2000 are the predicted data.

The DCM double wave model results for `Rmonthly2000` and `Rmonthly` samples are given in the DCM-manual (Tables 8 and 9, respectively). For both samples, the periods and amplitudes of the eight strongest double wave signals are summarised in Table 6 (Columns 4 and 5).

The prediction test statistic  $z_{\text{pred}}$  (Equation 30) decreases until six signals are detected. Then,  $z_{\text{pred}}$  begins to increase for seven and eight signals (Figure 7a). This indicates that the first six detected signals are real, but the next seventh and eighth signals are not.

The prediction obtained from the predictive data `Rmonthly2000` sample begins after the black vertical dash-dotted line at the year 2000 (Figure 7b). For twenty years, the majority of predictive model residuals (blue dots) are within the ISES limit (Equation 42: cyan dash dotted lines). The six signal double wave DCM model can reproduce the Dalton minimum inside `Rmonthly2000`. The thirty years sliding mean shows a dip at the end of the Maunder minimum. This dip outside sample `Rmonthly2000` does not cover the whole Maunder minimum era (Figure 7c: green curve).

The predictive data `Rmonthly2000` sample  $z_{\text{pred}}$  (Equation 30) values indicate the presence of six signals (Figure 7a). The all data `Rmonthly` sample mean level prediction  $m_{\text{mean}}$  (Equation 32) for the Maunder minimum supports this result. The predicted mean level  $m_{\text{mean}}$  curve for the Maunder minimum shows an expected dip (Figure 7d: red curve). For the first three  $\mathcal{M}=1-3$  signals, this red  $m_{\text{pred}}$  curve is above the all data mean level  $m$  denoted with dotted black line. For the next three  $\mathcal{M}=4-6$  signals, the  $m_{\text{pred}}$  values fall below the  $m$  mean level. Finally, these  $m_{\text{mean}}$  values for  $\mathcal{M}=7$  and 8 signals rise again above the mean level  $m$ .

The Maunder minimum is outside all data sample `Rmonthly`. It is the closest activity minimum before the beginning of this sample. This could explain why only this particular deterministic activity minimum prediction succeeds. The  $m_{\text{pred}}$  predictions fail for the other activity minima,

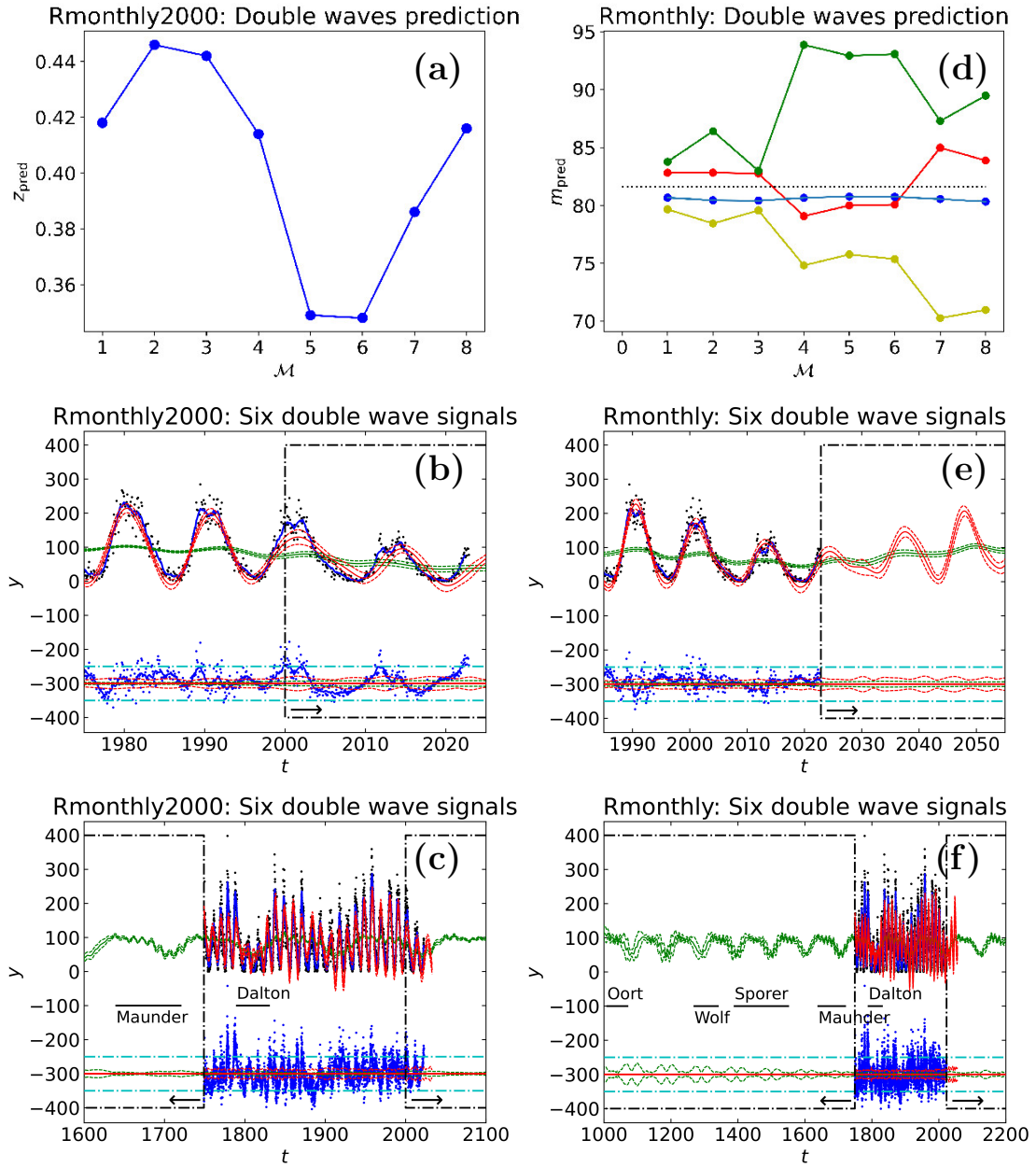


**Figure 7.** Rmonthly2000 predictions for double waves (DCM-manual: Table 8). (a-c) Best double wave model  $M=6$  minimises  $z_{\text{pred}}$  (Equation 30). Otherwise as in Figures 6a-c. (d-f) Rmonthly predictions for double waves (DCM-manual: Table 9). Otherwise as in Figures 6d-f.

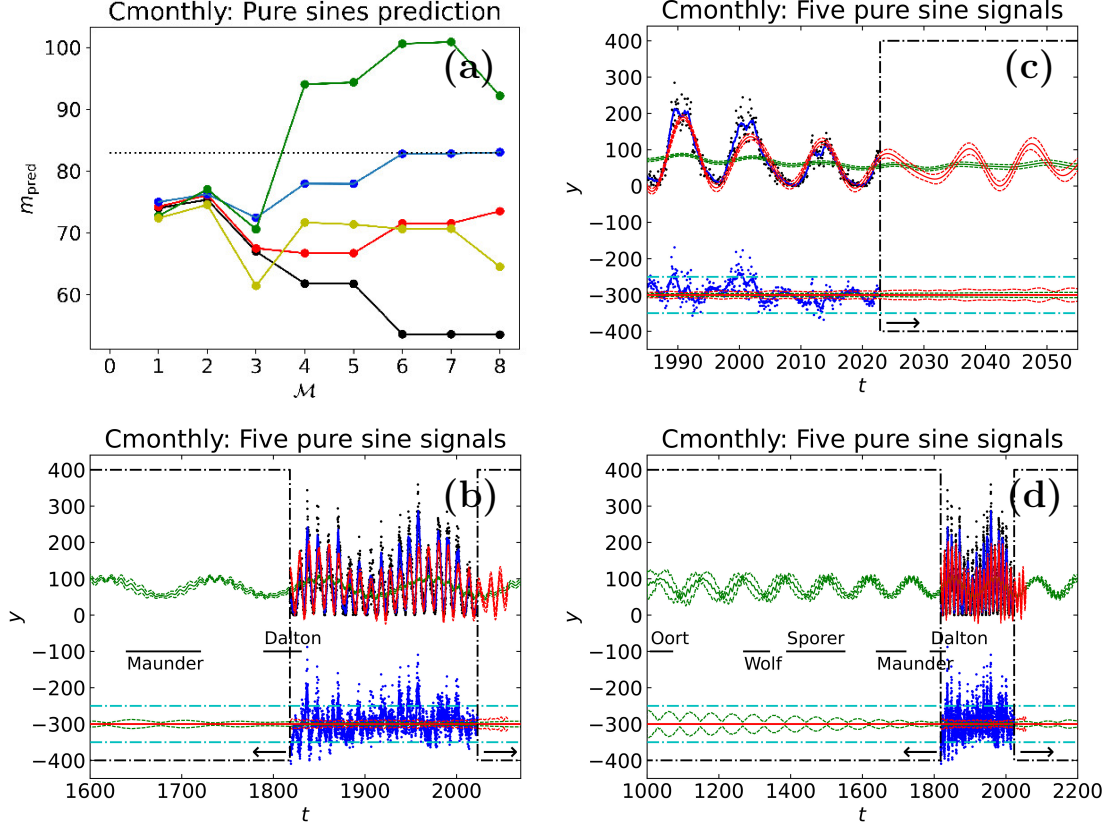


**Figure 8.** Cmonthly predictions for pure sines (DCM-manual: Table 11). (a) Pure sine  $M=1-8$  model predictions for  $m_{\text{pred}}$  (Equation 32) during Dalton (black), Maunder (red), Sporer (blue), Wolf (green) and Oort (yellow) minima. Otherwise as in Figure 6d. (b) Model  $M=5$  pure sine prediction for near past. Otherwise as in Figure 6c. (c) Model  $M=5$  pure sine prediction for near future. Otherwise as in Figure 6e. (d) Model  $M=5$  pure sine long-term predictions. Otherwise as in Figure 6f.

probably because these minima are further away in the past than the Maunder minimum. The decreasing Oort minimum  $m_{\text{mean}}$  trend deserves to be mentioned (Figure 7d: yellow curve).

The six double wave DCM model for all data Rmonthly sample predicts that the mean level of solar activity begins to rise in the near future (Figure 7e: green curve). This model predicts a turning point at 2029, which does not necessarily represent the beginning of a new activity cycle (Figure 7e: red curve). The long-term thirty years sliding mean shows a clear dip during the end of Maunder minimum (Figure 7f: green curve).

### 6.3. Weighted monthly sunspot data

The Cmonthly2000 sample contains the predictive data. The Cmonthly sample contains all data, where the observations after the year 2000 are the predicted data.

For the predictive data Cmonthly2000 sample, both pure sine and double wave models are unstable for more than two signals (DCM-manual: Tables 10 and 12, “UM”). The detected signals are given in Table 6 (Columns 6 and 8). It is of no use to study predictivity for only two detected signals in sample Cmonthly2000.

For all data sample **Cmonthly**, all double wave models for two or more signals are unstable (DCM-manual: Table 13, “UM”). The only detected signal is given in Table 6 (Column 9). It would make no sense to study predictivity for only one signal detected in sample **Cmonthly**.

Fortunately, we can detect five pure sine signals in all data sample **Cmonthly** (DCM-manual: Table 11). These signals are given in Table 6 (Column 7). The predicted mean level  $m_{\text{pred}}$  (Equation 32) curves are promising (Figure 8a). The  $m_{\text{pred}}$  curves for all activity minima in Table 1 show a dip at model  $M=3$ . This dip is clearly below the dotted black line denoting the mean  $m = 81.6$  of all monthly sunspot numbers. Except for the green Wolf minimum curve, all  $m_{\text{pred}}$  curves stay below this mean  $m$ . The predicted mean level  $m_{\text{pred}}$  curve for the Dalton minimum is convincing (Figure 8a: black curve), most probably because this activity minimum between 1790 and 1830 partly overlaps the **Cmonthly** sample between 1818 and 2022. Furthermore, the predicted mean level  $m_{\text{pred}}$  curve for the second closest Maunder minimum is good (Figure 8a: red curve).

The deterministic predictions for the Dalton and the Maunder minima are illustrated in Figure 8b (green curve). These curves can reproduce the duration of these activity minima, but not the low values of sunspots. The errors for the predicted model (red dotted lines) and the predicted sliding 30 years mean (green dotted lines) are far smaller than the ISES limit (Equation 42: dashed dotted cyan lines). This deterministic prediction is obtained for the two past centuries before the beginning of data. The time span of this successful prediction is about twenty times longer than the one sunspot cycle limit of stochastic  $H_{\text{Dynamo}}$  hypothesis predictions. Since this model can predict the time intervals of past weak activity, it should also be able to predict the time intervals of future weak activity. The same five pure sine signal prediction for the next decades is shown in Figure 8c (red curve). The long-term prediction confirms the result already obtained earlier for other samples: the activity level of the Sun increases during the next half a century (Figure 8d: green curve).

#### 6.4. Non-weighted yearly sunspot data

The four and eight signal DCM double wave models have  $\eta = 21$  and  $\eta = 21 + 20$  free parameters, respectively. The yearly sunspot data sample **Ryearly2000** contains only  $n = 300$  observations. To avoid over-fitting, we analyse these yearly data only with the four and eight signal DCM pure sine models having  $\eta = 13$  and  $\eta = 13 + 12$  free parameters.

The **Ryearly** sample contains all data, where observations after 2000 are the predicted data. The **Ryearly2000** sample observations are the predictive data.

The predictive data sample **Ryearly2000** DCM analysis gives the predicted test statistic  $z_{\text{pred}}$  (Equation 30) values shown in Figure 9a. The best six signal model gives the smallest  $z_{\text{pred}}$  value. The  $z_{\text{pred}}$  values for the seven and eight signal models are larger.

This six signal model gives an amazingly accurate prediction for the twenty years of predicted data after the year 2000 (Figure 9b: red curve after the vertical black dash-dotted line). *All* predicted data values are between the dotted red lines denoting  $\pm 3\sigma$  prediction error limits. About half of these black dots denoting the predicted data overlap the continuous red line denoting the predicted model. *All* residuals of predicted data (blue dots) are significantly smaller than the ISES limit (Equation 42: cyan dash dotted lines). Had we been able to apply DCM to the **Ryearly2000** sample in the year 2000, we could have predicted the yearly sunspots number for the next two decades! The time span of this successful deterministic prediction is about two times longer than the stochastic one sunspot cycle prediction limit of  $H_{\text{Dynamo}}$  hypothesis.

For **Ryearly2000** sample, the six signal model can reproduce the Dalton minimum inside the predictive data, but not the Maunder minimum, which is outside this sample (Figure 9c: green curve).

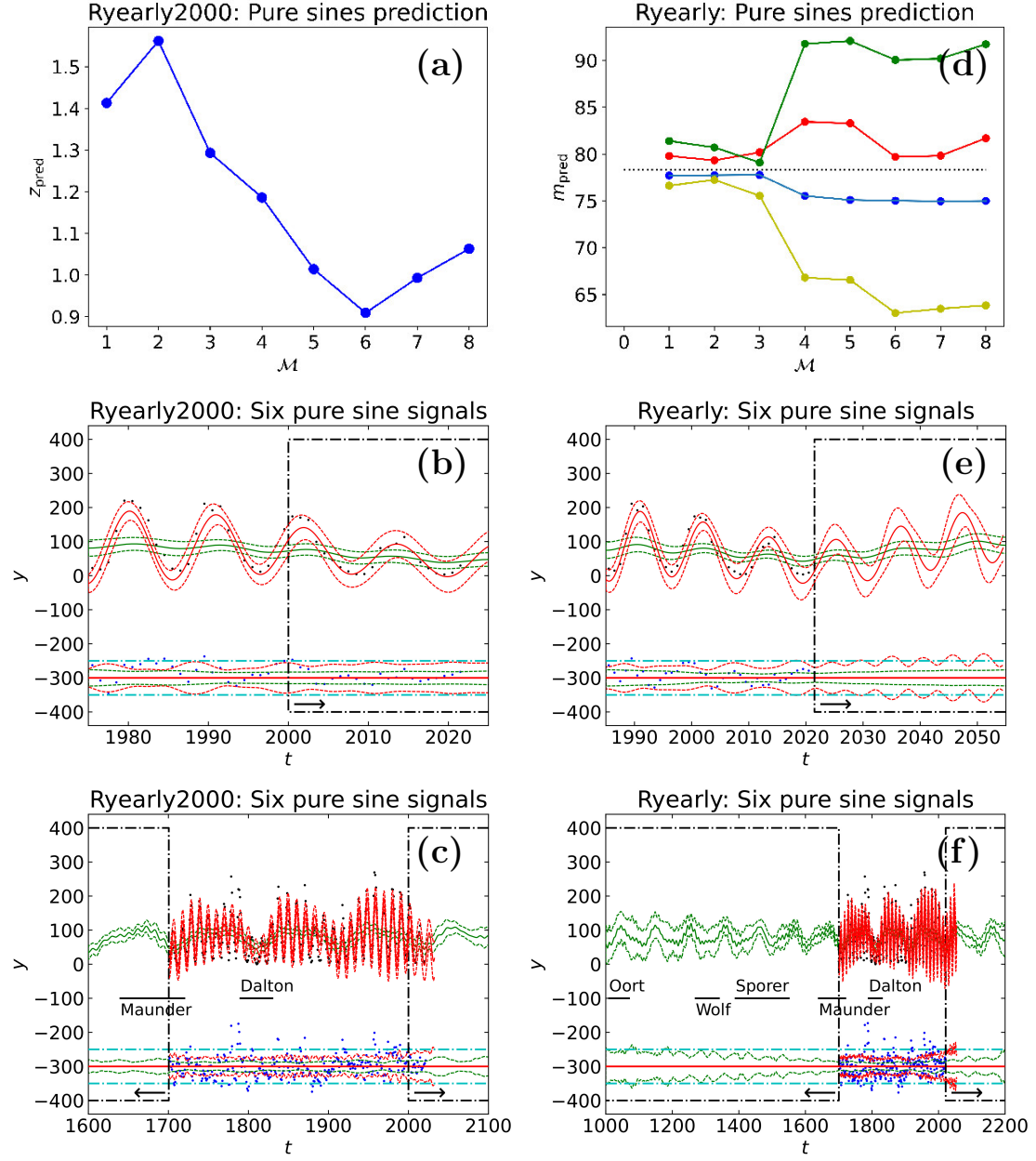


**Figure 9.** (a-c) Ryearly2000 predictions for pure sines (DCM-manual: Table 14). Otherwise as in Figure 6a-c. Ryearly predictions for pure sines (DCM-manual: Table 15). Otherwise as in Figure 6d-f.

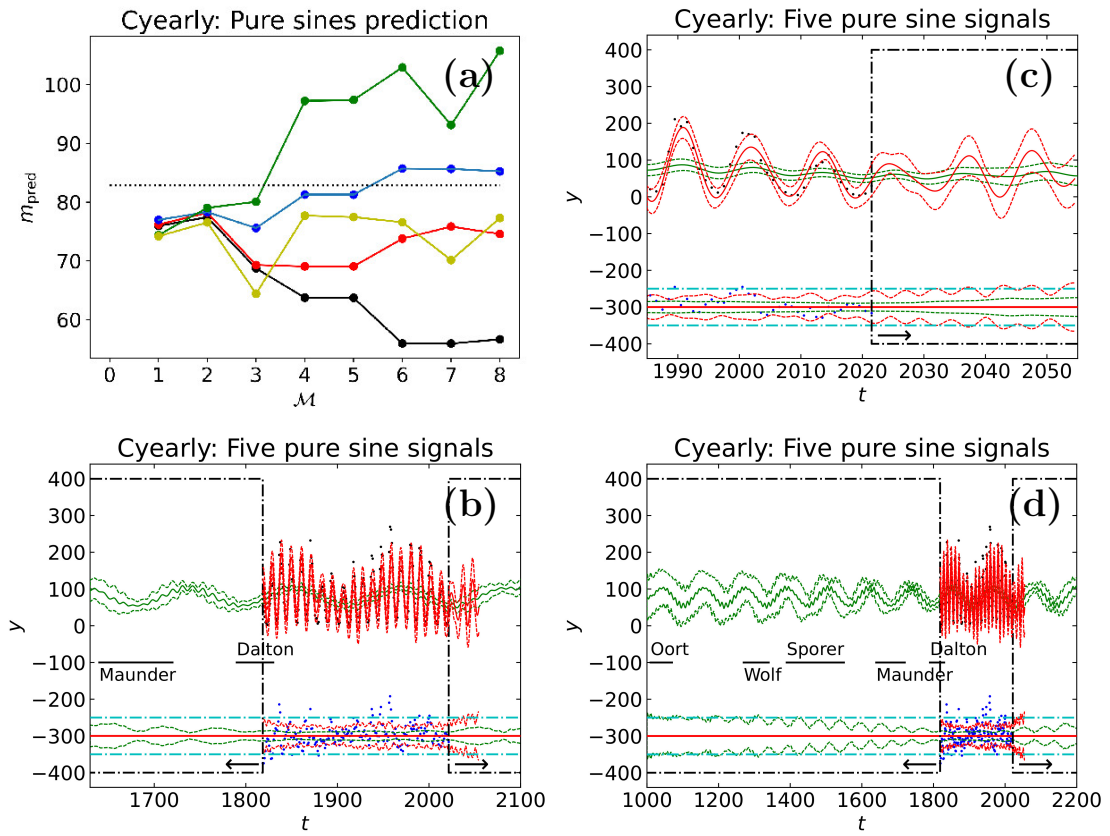


**Figure 10.** (a-d) Cyearly predictions (DCM-manual: Table 17). Otherwise as in Figure 8a-d.

The predicted mean levels  $m_{\text{pred}}$  (Equation 32) for the all data sample **Cyearly** are shown in Figure 9d. Even the red curve for the Maunder minimum, which is closest to the beginning of this **Cyearly** sample, stays above the mean level  $m = 78.4$  of all data. These predicted mean level  $m_{\text{pred}}$  estimates for the past activity minima do not succeed. The six pure sine signal model for the next decades predicts rising solar activity (Figure 9e: green line).

### 6.5. Weighted yearly sunspot data

The predictive data sample is **Cyearly2000**. Sample **Cyearly** is all data, where the observations after the year 2000 are the predicted data. We study only the pure sine DCM models, because the **Cyearly** and **Cyearly2000** samples are both too small ( $n = 204$  and  $182$ ) for the DCM double wave model analysis.

We detect only two pure sine signals in the predictive data sample **Cyearly2000**. Additional signals give unstable models (DCM-manual: Table 16, “UM”). Therefore, no prediction is made.

Five pure sine signals are detected in all data sample **Cyearly** (DCM-manual: Table 17). We give the periods and amplitudes of these five signals in Table 6 (Column 13).

The pure sine signal DCM models  $M=1-8$  give the predicted mean level  $m_{\text{pred}}$  (Equation 32) values shown in Figure 10a. The black and red  $m_{\text{pred}}$  curves for the Dalton and the Maunder minima fall clearly below the mean level  $m = 82.8$  of all yearly sunspot data. After this, these two

**Table 10.** Predictions for next three sunspot cycles. (1) Sample: Figure showing predictions. (2-3) Maximum and minimum  $t$  and  $y$  of cycle 25. (4-5) Sunspot cycle 26. Otherwise as in “2-3”. (6-7) Sunspot cycle 27. Otherwise as in “2-3”. Line below each group of five estimates gives their weighted mean.

	(1)	(2)	(3)	(4)	(5)	(6)	(7)
Sample: Figure		Maximum 25		Maximum 26		Maximum 27	
		$t$ (y)	$y$ (-)	$t$ (y)	$y$ (-)	$t$ (y)	$y$ (-)
Rmonthly: Figure 6e	$2025.86 \pm 0.16$	$118.4 \pm 5.9$	$2037.40 \pm 0.20$	$148.7 \pm 5.7$	$2048.41 \pm 0.22$	$170.9 \pm 5.4$	
Rmonthly: Figure 7e	$2024.42 \pm 0.20$	$88.6 \pm 4.8$	$2037.6 \pm 4.9$	$146 \pm 30$	$2047.9 \pm 5.1$	$207 \pm 18$	
Cmonthly: Figure 8c	$2024.07 \pm 0.19$	$89.4 \pm 4.1$	$2037.39 \pm 0.13$	$102.8 \pm 5.3$	$2047.48 \pm 0.15$	$116.6 \pm 5.4$	
Ryearly: Figure 9e	$2025.28 \pm 0.39$	$106 \pm 14$	$2036.62 \pm 0.41$	$145 \pm 16$	$2047.40 \pm 0.41$	$185 \pm 15$	
Cyearly: Figure 10c	$2024.36 \pm 0.78$	$90 \pm 10$	$2037.4 \pm 1.3$	$112 \pm 22$	$2047.5 \pm 2.0$	$126 \pm 21$	
Weighted mean:	$2024.94 \pm 0.79$	$95 \pm 12$	$2037.34 \pm 0.19$	$125 \pm 22$	$2047.72 \pm 0.41$	$148 \pm 30$	
		Minimum 25		Minimum 26		Minimum 27	
Rmonthly: Figure 6e	$2031.57 \pm 0.18$	$16.8 \pm 6.1$	$2042.82 \pm 0.20$	$22.4 \pm 5.5$	$2053.76 \pm 0.23$	$34.0 \pm 5.0$	
Rmonthly: Figure 7e	$2032.7 \pm 5.0$	$25 \pm 10$	$2043.4 \pm 5.0$	$6 \pm 15$	$2054.1 \pm 5.4$	$39.4 \pm 6.8$	
Cmonthly: Figure 8c	$2031.77 \pm 0.28$	$19.2 \pm 4.4$	$2042.35 \pm 0.14$	$0.3 \pm 4.4$	$2052.58 \pm 0.18$	$28.8 \pm 5.2$	
Ryearly: Figure 9e	$2030.77 \pm 0.38$	$-15 \pm 15$	$2041.79 \pm 0.38$	$16 \pm 16$	$2052.62 \pm 0.41$	$38 \pm 17$	
Cyearly: Figure 10c	$2031.8 \pm 1.1$	$16 \pm 13$	$2042.3 \pm 2.0$	$-1 \pm 19$	$2052.7 \pm 2.2$	$28 \pm 17$	
Weighted mean:	$2031.52 \pm 0.31$	$17.4 \pm 7.4$	$2042.44 \pm 0.29$	$9 \pm 10$	$2052.98 \pm 0.56$	$33.0 \pm 4.3$	

curves also stay below this  $m$  level. These results are not unexpected because the Dalton and the Maunder minima are the closest activity minima before the beginning of the **Cyearly** sample.

The all data sample **Cyearly** prediction for the time intervals of the Dalton and the Maunder minima is excellent (Figure 10b: green curve). However, the prediction can not reproduce the low number of sunspots during the Maunder minimum. The green dotted lines denoting the error of the predicted 30 years sliding mean stay well below the ISES limit denoted with cyan dash-dotted lines (Equation 42). This successful deterministic prediction for the Maunder minimum time interval covers two centuries backwards, before the beginning of the analysed data sample **Cyearly**. This time interval is about twenty times longer than the stochastic  $H_{\text{Dynamo}}$  hypothesis predictability limit of only one solar cycle. It is actually quite unexpected that only about 200 years of data can predict so well the activity mean level for the past 200 years without any data. This can succeed only if the model is correct and deterministic. It also means that our prediction for the future can be considered reliable. This **Cyearly** sample future prediction for the next decades is shown in Figure 10c. The long-term prediction indicates rising solar activity during the next half a century (Figure 10d).

Our best predictive models are very consistent because the number of signals in all models is either five (Figures 6a, 8a and 10a) or six (Figures 7a and 9a). We conclude that the results presented in Sections 6.2-6.5 confirm the predictability of sunspot numbers.

## 6.6. Future sunspot maxima and minima predictions

We give the predictions for the next three sunspot cycle maxima and minima in Table 10.

The lowest possible real sunspot number is zero. We can not prevent DCM from utilising negative model  $g(t)$  values. For this reason, two predicted cycle minimum sunspot number estimates out of all fifteen estimates,  $y = -15 \pm 15$  and  $y = -1 \pm 19$ , are negative (Table 10). However, in these two exceptional cases the sunspot number can be zero within  $\pm 1\sigma$ .

The ISES prediction for the cycle 25 maximum epoch was  $t = \text{July } 2025 \pm 8.0$  months =  $2025.54 \pm 0.67$ . Their smoothed maximum sunspot number prediction was  $y = 115$ . Our

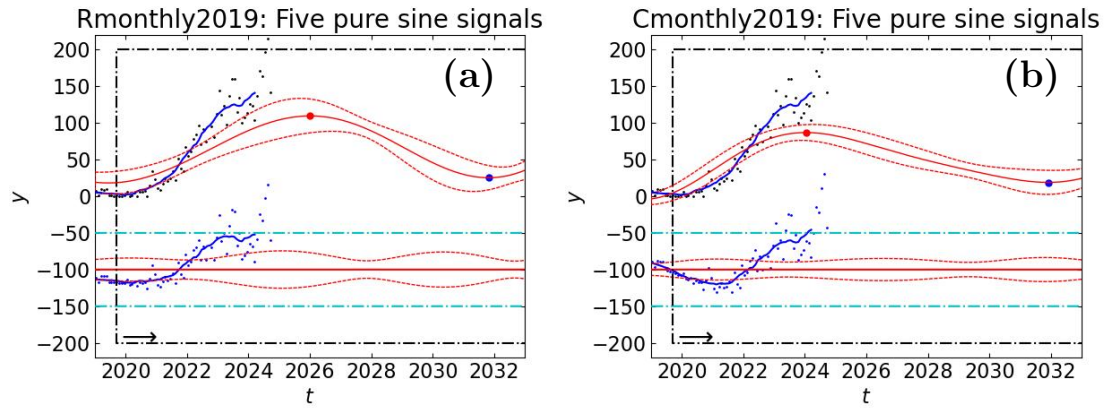


**Figure 11.** DCM predictions for cycle 25. (a) Nonweighted five pure sines prediction for sample **Rmonthly2019** has maximum  $y = 109.6 \pm 7.7$  at  $2026.0 \pm 0.3$  (red circle) and minimum  $y = 25.3 \pm 6.1$  at  $2031.8 \pm 4.8$  (blue circle). Otherwise as in Figure 6. (b) Weighted five pure sines prediction for sample **Cmonthly2019** has maximum  $y = 86.9 \pm 3.8$  at  $t = 2024.04 \pm 0.24$  and minimum  $y = 18.9 \pm 5.3$  at  $t = 2031.92 \pm 0.22$ . Otherwise as in “a”.

predictions  $t = \text{December } 2024 \pm 9.5 \text{ months} = 2024.94 \pm 0.79$  and  $y = 95 \pm 12$  differ  $0.76\sigma$  and  $1.67\sigma$  from the ISES prediction.

Our prediction error  $\pm 0.^y79$  for the cycle 25 maximum epoch is much larger than our prediction errors  $\pm 0.^y19$  and  $\pm 0.^y41$  for the next two maximum epochs (Table 10). This is a real statistical effect. The predicted peak of this next cycle 25 maximum is lower than, and not so sharp as, the predicted peaks of the next cycle 26 and 27 maxima (Figures 6e, 7e, 8c, 9e, and 10c).

The six double wave model predictions for the largest **Rmonthly** sample are not very accurate in Table 10 (**Rmonthly**: Figure 7e). The probable reason for this inaccuracy is the large number  $\eta = 21 + 10$  of the free parameters (DCM-manual: Table 9, model  $M=6$ ). This is also the only model that has a turning point in the year 2029 (Figure 7e).

We predict that the mid-point of the next prolonged grand sunspot minimum is approximately in the year 2100 (Figures 6f, 7f, 8d, 9f and 10d: green curve).

## 6.7. Prediction for current sunspot cycle 25

After the analysis of all eight samples summarised in Table 5, we were requested to give our own prediction for the ongoing cycle 25. All data after September 2019 are removed from the samples **Rmonthly** and **Cmonthly**. This gives us all data before the beginning of cycle 25 (DCM-manual: samples **Rmonthly2019** and **Cmonthly2019**).

Our DCM five pure sine signal prediction for the **Rmonthly2019** sample of non-weighted monthly sunspot numbers is shown in Figure 11a. Our prediction for the smoothed monthly mean (continuous blue curve) is within the ISES limit (dash dotted magenta line). The next predicted minimum and maximum epochs are January, 2026 and September, 2031, respectively.

For the weighted **Rmonthly2019** sample, we show the DCM five pure sine signal prediction in Figure 11b. The last smoothed monthly mean value exceeds the ISES limit. The predicted maximum for this monthly mean is at January, 2024, which means that the monthly mean sunspot number should start decreasing soon. The next predicted minimum is November, 2031.

The panel’s prediction for the next sunspot minimum is far from exact because the activity fades extremely slowly from the year 2034 to 2037 (Figure 5). This fading period begins about three years after our predicted minima at the end of the year 2031.

**Table 11.** Three strongest signals in all data samples. (1) Sample:  $K_2 = 1$  or 2 model. (2) Signal  $S_{11y}$ : Period  $P_{11y}$  and amplitude  $A_{11y}$ . (3-4) Same for  $S_{10y}$  and  $S_{11.y86}$  signals. (5)  $R_{\text{Signal}}$  (Equation 43). (6)  $R_{\text{Signal}}$  (Equation 44). Lowest line gives period, amplitude, and  $R_{\text{Signal}}$  weighted means. Note that  $S_{10y}$  signal in  $\text{Rmonthly}$ :  $K_2 = 2$  is a double sinusoid<sup>2×</sup>.

(1)	(2)	(3)	(4)	(5)	(6)
Sample: $K_2$	$S_{11y}$ $P_{11} (\text{y})$ $A_{11} (-)$	$S_{10y}$ $P_{10} (\text{y})$ $A_{10} (-)$	$S_{11.y86}$ $P_{11.y86} (\text{y})$ $A_{11.y86} (-)$	$R_{\text{Signal}} (-)$	$R_{\text{Signal}} (-)$
$\text{Rmonthly: } K_2 = 1$	$11.0033 \pm 0.0064$ $101.5 \pm 2.5$	$10.0001 \pm 0.0081$ $65.5 \pm 2.1$	$11.807 \pm 0.012$ $56.4 \pm 2.4$	$0.338 \pm 0.016$	$0.861 \pm 0.046$
$\text{Rmonthly: } K_2 = 2$	$10.9878 \pm 0.0051$ $104.6 \pm 2.3$	$10.0031 \pm 0.0044^{2\times}$ $75.2 \pm 2.7$	$11.770 \pm 0.011$ $62.7 \pm 2.6$	$0.349 \pm 0.016$	$0.834 \pm 0.046$
$\text{Cmonthly: } K_2 = 1$	$10.8585 \pm 0.0048$ $117.5 \pm 2.9$	$10.0658 \pm 0.0077$ $59.3 \pm 2.8$	$11.863 \pm 0.021$ $43.3 \pm 2.0$	$0.245 \pm 0.013$	$0.730 \pm 0.048$
$\text{Ryearly: } K_2 = 1$	$10.981 \pm 0.020$ $98.3 \pm 7.8$	$9.975 \pm 0.017$ $62.8 \pm 6.1$	$11.820 \pm 0.027$ $40.5 \pm 3.3$	$0.251 \pm 0.026$	$0.645 \pm 0.081$
$\text{Cyearly: } K_2 = 1$	$10.863 \pm 0.022$ $119.3 \pm 7.5$	$10.058 \pm 0.026$ $61.0 \pm 9.6$	$11.856 \pm 0.068$ $43.8 \pm 7.9$	$0.243 \pm 0.047$	$0.718 \pm 0.17$
Weighted mean	$10.938 \pm 0.066$ $107.0 \pm 6.8$	$10.014 \pm 0.026$ $66.3 \pm 5.8$	$11.799 \pm 0.031$ $50.5 \pm 8.6$	$0.294 \pm 0.048$	$0.739 \pm 0.072$

## 7. Discussion

In time series analysis, the detected periods are usually considered real if they have an accepted physical cause, like in the DCM analysis by Jetsu (2021). Here, such a widely accepted cause for the detected strictly periodic, extremely significant and predictive signals is missing. There must be an astrophysical mechanism that causes these signals in the sunspot data, unless both DCM and DFT give the same misleading results. Whatever this astrophysical mechanism may be, why would both of these statistical methods detect the same unreal signals? What other solar system physical mechanism can cause these signals, except the planets? This would mean that the solar cycle is not generated only by the physical mechanisms inside the Sun. We consider two alternative external causes: the planetary gravitational forces and the planetary magnetic forces.

The  $S_{11y}$ ,  $S_{10y}$ ,  $S_{11.y86}$ ,  $S_{110y}$  and  $S_{10.y6}$  signals are the strongest ones (Table 6). Since these five signals are clearly connected (Table 8), their interference is repeated indefinitely, as long as the orbital periods of the involved planets remain constant. For example, the  $\text{Rmonthly}$  sample  $n = 3287$  observations have  $m = 81.6$  and  $s = 67.7$ . Only twenty  $y_i$  values exceed  $m + 3s = 285$ . The best model for this sample, the sum of five pure sine signals, has the mean level  $M_0 = 81.3 \pm 0.8$ . The sum of the peak to peak amplitudes for these five strongest  $S_{11y}$ ,  $S_{10y}$ ,  $S_{11.y86}$ ,  $S_{110y}$  and  $S_{10.y6}$  signals is  $A_{11y} + A_{10y} + A_{11y.86} + A_{110y} + A_{10y.6} = 331$  (Table 6: column 2). These five signals alone can reproduce the whole range of observed  $y_i$  changes. No additional signals are needed. The interference of  $S_{11y}$  and  $S_{10y}$  signals can cause the  $S_{110y}$  signal (Table 8). After this, the interference of  $S_{11.y86}$  and  $S_{110y}$  signals can cause the  $S_{10.y6}$  signal. Hence, the  $S_{11y}$ ,  $S_{10y}$  and  $S_{11.y86}$  signals may be the only real ones. We give the weighted mean periods and amplitudes of these three strongest signals in Table 11.

The weighted mean  $P_{11y} = 10.938 \pm 0.066$  years period of the strongest  $S_{11y}$  signal differs  $0.94\sigma$  from  $11 \times P_{\text{Earth}}$ . The  $0.26\sigma$  difference from  $10 \times P_{\text{EJ}} = 10.921$  years is even smaller, where is the  $P_{\text{EJ}} = 1.0921$  years synodic period of the Earth and Jupiter. The Earth may cause this strongest  $S_{11y}$  signal alone, or together with Jupiter.

**Table 12.** Relative tidal forces of planets (Equation 45). (1) Planet. (2) Major axis. (3) Mass. (4) Relative tidal force.

Planet	(1) a ( $a_{\text{Earth}}$ )	(2) m ( $m_{\text{Earth}}$ )	(4) $R_{\text{Tidal}}$ (-)
Mercury	0.39	0.055	0.95
Venus	0.72	0.82	2.16
Earth	1.00	1.00	1.00
Mars	1.52	0.11	0.030
Jupiter	5.20	318	2.26
Saturn	9.53	95.3	0.11
Uranus	19.2	14.5	0.0020
Neptune	30.1	17.3	0.00063

The weighted mean  $P_{10y} = 10.014 \pm 0.026$  years period of the second strongest  $S_{10y}$  signal differs  $0.54\sigma$  from  $10 \times P_{\text{Earth}}$ . This signal is probably connected only to the Earth, because the closest synodic period multiple  $9 \times P_{\text{EJ}} = 9.829$  years is  $7.1\sigma$  away.

The third strongest  $S_{11,y86}$  signal has  $P_{11,y86} = 11.799 \pm 0.031$  years weighted mean period. It differs  $1.9\sigma$  from the  $P_{\text{Jupiter}} = 11.857$  years period. Since the closest  $11 \times P_{\text{EJ}} = 12.013$  years synodic period multiple is  $5.0\sigma$  away, this  $S_{11,y86}$  signal is probably connected only to Jupiter.

If the  $S_{11,y86}$  signal is connected only to Jupiter, and the  $S_{11y}$  and  $S_{10y}$  signals are connected only to the Earth, the weighted mean of Jupiter's and the Earth's signal amplitude ratio is

$$R_{\text{Signal}} = A_{11y.86} / (A_{11y} + A_{10y}) = 0.294 \pm 0.048. \quad (43)$$

If the  $S_{11y}$  signal is connected both to the Earth and Jupiter, the weighted mean signal amplitude ratio is

$$R_{\text{Signal}} = A_{11y.86} / A_{10y} = 0.739 \pm 0.07. \quad (44)$$

In this relation, we assume that Jupiter's and the Earth's amplitude ratio is equal to  $R_{\text{Signal}}$  also in the  $S_{11y}$  signal.

The mass  $m_{\text{Earth}}$  and the major axis  $a_{\text{Earth}}$  of Earth give the dimensionless relative tidal force

$$R_{\text{Tidal}} = \frac{m}{m_{\text{Earth}}} \left( \frac{a_{\text{Earth}}}{a} \right)^3, \quad (45)$$

exerted by each planet to the Sun, where the planet's mass is  $m$  and its major axis is  $a$ . The tidal forces of Venus and Jupiter are much stronger than those of the Earth and Mercury (Table 12). The tidal forces of Mars, Saturn, Neptune and Uranus are negligible.

Recently, several attempts have been made to model an internal solar dynamo influenced by external gravitational tidal forces of planets. Stefani, Giesecke, and Weier (2019) presented a solar dynamo, where the planetary tidal forcing causes periodic 11.07 and 22.14-year magnetic field oscillations. Scafetta and Bianchini (2022) reviewed the possible physical mechanisms that could explain how the weak planetary tidal forces can alter the solar structure and cause the sunspot cycle. Charbonneau (2022) showed that if the external planetary signal is not constantly amplified, the internal solar dynamo mechanism fluctuations can mask this external signal. More recently, Cionco, Kudryavtsev, and Soon (2023) argued that the combined tidal forcing of Venus,

the Earth and Jupiter can not cause the 11-years solar cycle. For both of our  $R_{\text{Signal}}$  values (Equations 43 and 44), the Earth's gravitational tidal forces would dominate over those of Jupiter. Since this is not true, we can exclude the alternative that the external planetary tidal forces cause the sunspot cycle.

Parker (1955) formulated the dynamo model, where the interaction of differential rotation and convective motion drives the solar magnetic field. The first models for a dynamo generated sunspot cycle were presented by Babcock (1961) and Leighton (1969). All dynamo model physical mechanisms causing the solar cycle are not yet fully understood (Charbonneau, 2010). As stated in our  $H_{\text{Dynamo}}$  hypothesis, it is widely accepted that the solar cycle is stochastic and unpredictable beyond one solar cycle (Petrovay, 2020). For example, the ISES panel predictions cover only the ongoing cycle (Figure 5). If these predictions were made for several cycles in a row, the prediction errors would certainly exceed the four year ISES limit (Equation 42).

The electromagnetic force is  $10^{40}$  times stronger than the gravitational force (Gillies, 1997). For a proton at the distance of Earth, the force due to the solar magnetic field is 60 000 stronger than the solar gravitational force (Alfvén, 1942). Jupiter and the Earth have the strongest planetary magnetic fields in the solar system (Schubert and Soderlund, 2011, their Table 2). Mercury has only a weak magnetic field, and Venus has none. Hansson (2022) and Muñoz, Wagemakers, and Sanjuán (2023) have formulated models, where the solar dynamo and the planetary magnetic fields interact, and cause the solar cycle. A similar interaction of magnetic fields has also been modelled for "hot Jupiter" exoplanets, but the results are uncertain, because the stellar magnetic field geometry is unknown (Ip, Kopp, and Hu, 2004; Cranmer and Saar, 2007). As for the solar magnetic field geometry, Parker (1958) first showed that at certain distances this field falls inverse squared  $r^{-2}$  due to the solar wind, and then he finally noted that the observations support the existence of a more complicated field structure. Our strongest  $S_{11y}$ ,  $S_{10y}$  and  $S_{11,y86}$  signals, could indeed be connected to the Earth and Jupiter, having the strongest magnetic fields. This would support the magnetic field interaction alternative, but does not prove it, because Mercury's and Venus' signal detection is statistically more difficult than the Earth's and Jupiter's signal detection (Appendix: Equations 53 and 57).

The interaction between stellar and exoplanet magnetic fields has been estimated by Cranmer and Saar (2007, Equation 2, hereafter CS-estimate). The solar magnetic field interacts directly with the planetary magnetic field during every FTE (Dungey, 1961; Nakariakov et al., 2016; Paul, Vaidya, and Strugarek, 2022; Sun et al., 2022). We assume that the CS-estimate is valid during FTEs because the closed magnetic field lines connect the planet and the Sun in a conductive environment. However, this estimate may be invalid due to the presence of solar wind.

Here, we assume that CS-estimate is valid during solar system FTEs. Our notations for a solar system planet are  $a$  = semi-major axis of orbit,  $v$  = orbital velocity,  $R$  = radius, and  $B_{\text{Planet}}$  = magnetic field strength given in Schubert and Soderlund (2011). The connection between the CS-estimate parameters and our parameters are  $B_{\star} \equiv B_{\text{Sun}}(a)$  = solar magnetic field strength at distance  $a$ ,  $B_{\text{P}} \equiv B_{\text{Planet}}$ ,  $r_{\text{mag}} \propto R$  and  $V_{\text{rel}} \equiv v$ . Our dimensionless parameters are  $a' = a/a_{\text{Earth}}$ ,  $v' = v/v_{\text{Earth}}$ ,  $R' = R/R_{\text{Earth}}$ ,  $B'_{\text{Sun}} = B_{\text{Sun}}(a)/B_{\text{Sun}}(a_{\text{Earth}})$  and  $B' = B_{\text{Planet}}/B_{\text{Earth}}$ . We assume that  $B'_{\text{Sun}} \propto a'^{-n_{\text{Sun}}}$ , where the unknown value can be  $n_{\text{Sun}} = -1, -2$ , or  $-3$ . Cranmer and Saar (2007) assumed that the magnetic interaction is proportional to the exoplanet disk area  $\propto R'^{n_{\text{Planet}}}$ , where  $n_{\text{Planet}} = 2$ . We test other  $R'^{n_{\text{Planet}}}$  alternatives, where the unknown  $n_{\text{Planet}}$  value can also be 0 (point source), 1 (planet's diameter), or 3 (planet's volume). Kepler's third law gives us  $v' \propto a'^{-1/2}$  for circular orbits. Under all the above assumptions, the CS-estimate gives the relative magnetic interaction parameter

$$R_{\text{Magnetic}} \propto a'^{(n_{\text{Sun}}-1/2)} R'^{n_{\text{Planet}}} B'. \quad (46)$$

**Table 13.** Relative magnetic interaction parameters of planets. (1) Combination number (Com). (2-3)  $n_{\text{Sun}}$  and  $n_{\text{Planet}}$  (Equation 46). (4)  $R_{\text{Magnetic}}$  values for  $a' = 0.387$ ,  $R' = 0.351$  and  $B' = 0.00789$  of Mercury (Equation 46). (5-11)  $R_{\text{Magnetic}}$  values for other planets.

(1)	(2)	(3)	(4)	(5)	(6)	(7)	(8)	(9)	(10)	(11)
Com	$n_{\text{Sun}}$	$n_{\text{Planet}}$	Mercury $a' = 0.387$ $R' = 0.351$	Venus $a' = 0.723$ $R' = 0.099$	Earth $a' = 1$ $R' = 1$	Mars $a' = 1.524$ $R' = 0.533$	Jupiter $a' = 5.202$ $R' = 11.2$	Saturn $a' = 9.562$ $R' = 9.45$	Neptune $a' = 19.304$ $R' = 4.01$	Uranus $a' = 30.278$ $R' = 3.88$
(-)	(-)	(-)	$B' = 0.00789$	$B' = 0$	$B' = 1$	$B' = 0.00263$	$B' = 14.5$	$B' = 0.737$	$B' = 0.842$	$B' = 0.710$
1	-1	0	0.033	0	1	0.0014	1.2	0.025	0.0099	0.0043
2	-2	0	0.085	0	1	0.00092	0.23	0.0026	0.00051	0.00014
3	-3	0	0.22	0	1	0.0006	0.045	0.00027	0.000027	0.0000047
4	-1	1	0.012	0	1	0.00074	14.0	0.24	0.04	0.017
5	-2	1	0.03	0	1	0.00049	2.6	0.025	0.0021	0.00055
6	-3	1	0.077	0	1	0.00032	0.51	0.0026	0.00011	0.000018
7	-1	2	0.004	0	1	0.0004	150.0	2.2	0.16	0.064
8	-2	2	0.01	0	1	0.00026	29.0	0.23	0.0083	0.0021
9	-3	2	0.027	0	1	0.00017	5.7	0.024	0.00043	0.000070
10	-1	3	0.0014	0	1	0.00021	1700.0	21.0	0.64	0.25
11	-2	3	0.0037	0	1	0.00014	330.0	2.2	0.033	0.0082
12	-3	3	0.0095	0	1	0.000091	63.0	0.23	0.0017	0.00027

We compute the  $R_{\text{Magnetic}}$  values for all  $n_{\text{Sun}} = -1, -2, -3$  and  $n_{\text{Planet}} = 0, 1, 2, 3$  combinations (Table 13). Note that all twelve  $n_{\text{Sun}}$  and  $n_{\text{Planet}}$  combinations give  $R_{\text{Magnetic}} = 1$  for the Earth. No one knows the correct  $n_{\text{Sun}}$  and  $n_{\text{Planet}}$  values, but we can test which combinations would support our  $R_{\text{Signal}}$  values (Equations 43 and 44). For example, Parker (1958) arrived at the value  $n_{\text{Sun}} = -2$  for the Sun, while Cranmer and Saar (2007) used  $n_{\text{Planet}} = 2$  for an exoplanet.

Jupiter dominates in nine  $n_{\text{Sun}}$  and  $n_{\text{Planet}}$  combinations (Table 13). Our results indicate that the Earth should dominate (Equations 43 and 44). The Earth, having  $F_{\text{magnetic}} = 1$ , does dominate in the three remaining possible combinations.

The Earth dominates in the Com=2 combination, where the  $n_{\text{Sun}} = -2$  and  $n_{\text{Planet}} = 0$  values give  $R_{\text{Magnetic}} = 0.23$  for Jupiter, which differs only  $1.3\sigma$  from  $R_{\text{Signal}} = 0.294 \pm 0.048$  (Equation 43). In this case, the  $S_{11y}$  and  $S_{10y}$  signals are caused only by the Earth, and the  $S_{11,y86}$  signal is caused only by Jupiter. This  $n_{\text{Sun}} = -2$  and  $n_{\text{Planet}} = 0$  combination would support the solar magnetic field relation  $r^{-2}$  in Parker (1958), and it also indicates that the planets can be treated as point sources.

The Earth dominates in the Com=3 combination  $n_{\text{Sun}} = -3$  and  $n_{\text{Planet}} = 0$ , which gives  $R_{\text{Magnetic}} = 0.045$  for Jupiter. This result contradicts both  $R_{\text{Signal}} = 0.294$  (Equation 43) and  $R_{\text{Signal}} = 0.793$  (Equation 44) because Jupiter's influence is underestimated.

In the Com=6 combination, the Earth dominates because the  $n_{\text{Sun}} = -3$  and  $n_{\text{Planet}} = 1$  values give  $R_{\text{Magnetic}} = 0.51$  for Jupiter. This value differs  $4.5\sigma$  from  $R_{\text{Signal}} = 0.294 \pm 0.048$  (Equation 43) and  $3.2\sigma$  from  $R_{\text{Signal}} = 0.739 \pm 0.072$  (Equation 44). However, the numerical  $R_{\text{Magnetic}} = 0.51$  value is  $0.013$  closer to  $R_{\text{Signal}} = 0.294$  than  $R_{\text{Signal}} = 0.739$ . The  $n_{\text{Sun}} = -3$  value would support the  $r^{-3}$  relation between two dipole magnetic fields (Ku et al., 2016, their Equation 1). The value  $n_{\text{Planet}} = 1$  means that the interaction in Equation 46 is proportional to the planet's diameter  $R'$ .

The geomagnetic field dominates the sunspot cycle in the two remaining possible Com=2 and 6 combinations. This would explain the strongest  $S_{11y}$  and  $S_{10y}$  signals. Jupiter's contribution would be weaker, and cause the third strongest  $S_{11,y86}$  signal. The interference of these three signals would cause the other  $S_{10,y6}$  and  $S_{110y}$  signals (Table 8). Mercury would have a weak contribution. The contributions of Venus, Mars, Saturn, Neptune and Uranus would be insignificant.

The FTEs are the only known physical mechanisms, where the planetary magnetic fields can interact *directly* with the solar magnetic field. At the Earth, these FTE reconnections occur at the dayside and the FTE magnetic flux ropes roll from low latitudes towards the winter pole (Raeder, 2006; Fear, Palmroth, and Milan, 2012; Nakariakov et al., 2016; Zhang et al., 2022). Hence, the FTE magnetic flux ropes are switching between the N and S poles of the terrestrial magnetic field. Due to the Earth's orbital motion, this rolling repeats a strict regular magnetic FTE pole switch period

$$P_{\text{FTE}} = P_{\text{Earth}} = 1^{\text{y}}. \quad (47)$$

For example, Hansson (2022) and Muñoz, Wagemakers, and Sanjuán (2023) have presented models, where this kind of repetitive strictly periodic magnetic perturbations may cause the solar cycle. If the relation in Equation 46 is valid, the geomagnetic field could have the strongest influence on the solar magnetic field (Table 13: Com=2 and 6). In this case, the ten and the eleven year multiples of the FTE pole switch periods  $P_{\text{FTS}} = P_{\text{Earth}}$  may cause the strongest  $S_{11^{\text{y}}}$  and  $S_{10^{\text{y}}}$  sunspot cycles. If the relation  $P_{\text{FTS}} = P_{\text{Jupiter}}$  (Equation 47) also holds for the dipole magnetic field of Jupiter, it may cause the third strongest  $S_{11.5^{\text{y}}86}$  cycle. The typical separation between the FTEs is 8 minutes (Lockwood and Wild, 1993, the Earth) and 12 minutes (Russell, 1995, Jupiter). Over a million toroidal FTE magnetic flux ropes of these two planets weaken the global solar poloidal dipole magnetic field during each 11 year solar cycle. And even if the CS-estimate were invalid, these toroidal FTE magnetic flux ropes may constantly perturb the Sun, until its poloidal dipole magnetic field repetitively flips after about 11 years. At the sunspot cycle minimum, the solar magnetic field also becomes a dipole (Parker, 1955).

Russell (1995) analysed the Pioneer 10 and 11, Voyager 1 and 2 and Ulysses satellite observations of Jupiter's FTEs. The FTE durations and temporal separations were similar for the Earth and Jupiter. However, the Earth's FTE amplitudes were about four times larger than the Jupiter's FTE amplitudes when scaled by the planetary magnetic field inside the magnetopause. We use the same scaling for the dimensionless magnetic field parameter  $B'$  in Equation 46. If the relative FTEs amplitude ratio between Jupiter and Earth is denoted  $R_{\text{FTE}} = 1/4$ , we have

$$R_{\text{Signal}} = 0.294 \pm 0.048 \text{ (Equation 43)} \approx R_{\text{Magnetic}} = 0.23 \text{ (Table 8: Com=2)} \approx R_{\text{FTE}} = 0.25. \quad (48)$$

This relation indicates there may be a connection between the sunspot cycles and the FTEs.

The  $P_{\text{R}} = 155 - 160$  days Rieger cycle in the solar flares was discovered by Rieger et al. (1984). This cycle has been later discovered in many other solar activity indices, including the sunspots, and the full periodicity range is between 155 and 190 days (Gurgenashvili et al., 2017). These periods are about half of the 365 days FTE pole switch period (Equation 47). Numerous  $P_{\text{R}}$  period subharmonics have also been detected (Dimitropoulou, Moussas, and Strintzi, 2008). The FTEs are most frequent during periods of southward interplanetary magnetic field (IMF) when the magnetic shear between the IMF and the geomagnetic field is strongest (Phan et al., 1994; Scurry, Russell, and Gosling, 1994). Since the shear changes are strictly periodic, the 27.4 days IMF rotation period (Xiang, Ning, and Li, 2020) could cause the Rieger  $P_{\text{R}}$  period subharmonics, and the 26.7 days period in the major solar flares (Bai, 1987; Jetsu et al., 1997). However, the Jupiter's and Mercury's FTEs would not be connected to the Rieger periods.

There might be a way where the FTEs create structures that follow the Hale's law. Since there are no earlier definitions for such structures, we shall refer to them as the "toroidal magnetic loops". A single FTE can not cause a sunspot, but maybe it can cause such a toroidal magnetic loop. The polarity of the global solar poloidal dipole magnetic field is marked by  $P_{\text{Sun}}$ . This  $P_{\text{Sun}}$  polarity is opposite on the northern and southern solar hemispheres. Let us presume that the toroidal FTE magnetic flux rope connects to the poloidal field  $P_{\text{Sun}} = \text{N}$  of an arbitrary solar hemisphere. The following stages might be involved in the formation of a toroidal magnetic loop.

---

1. The polarity at FTE magnetic flux rope footpoint on solar surface is  $P_{\text{rope}} = P_{\text{Sun}} = \text{N}$ .
2. This causes  $P_{\text{toroidal}} = \text{N}$  polarity of the leading toroidal magnetic loop footpoint.
3. The magnetic flux through the FTE magnetic flux rope weakens poloidal  $P_{\text{Sun}} = \text{N}$ .
4. The polarity at the planetary end of the FTE magnetic flux rope is  $P_{\text{rope}} = \text{S}$ .
5. The FTE magnetic flux rope reconnects to the Sun when the FTE ends.
6. This causes  $P_{\text{toroidal}} = \text{S}$  polarity of the trailing toroidal magnetic loop footpoint.
7. This toroidal magnetic loop footpoint trails because the Parker spiral trails.
8. The trailing toroidal magnetic loop footpoint  $P_{\text{toroidal}} = \text{S}$  polarity weakens poloidal  $P_{\text{Sun}} = \text{N}$ .

At both solar hemispheres, the constantly forming toroidal magnetic loops weaken the solar poloidal dipole field, until it flips, and a new sunspot cycle begins. The dipole magnetic fields of planets do not flip. After the flip of the solar poloidal dipole field, these planetary dipole fields proceed to break up the new opposite polarity solar poloidal dipole field.

The stage 5 is the most critical one in our toroidal magnetic loop formation idea. The FTE magnetic flux rope is not “outside the Sun”, although it extends to the planet. Every FTE magnetic flux rope is inside the conductive plasma surrounding the Sun. Hence, the spiralling charged particles in the FTE magnetic flux rope are not “cut off” from the Sun at the end of an FTE. There are two alternatives at the end of every FTE. In the first alternative, the FTE magnetic flux rope reconnects to the solar magnetic field and does not release its spiralling charged particles, as described in stage 5. In the second alternative, the FTE magnetic flux rope does not reconnect to the solar magnetic field and releases its spiralling charged particles, like in the solar flares. Both alternatives can be realised in the Sun. There is no third alternative. This means that some FTE magnetic flux ropes can transform to toroidal magnetic loops. The first reconnection alternative becomes less probable during sunspot maximum, which would explain why the second alternative (flares) occurs more frequently during those periods.

Our toroidal magnetic loop idea requires an answer to the following amplification problem. The magnetic fields in the sunspots are many orders larger than those in the FTEs. Some physical mechanism must amplify the weak magnetic fields in these toroidal magnetic loops. There are such possible mechanisms, where these weak magnetic fields could act as “seeds” for the sunspots (e.g. Khomenko et al., 2017; Tzeferacos et al., 2018). Perhaps the feeble toroidal magnetic loops caused by FTEs can evolve into strong sunspot pair structures that exhaust the global poloidal dipole solar magnetic field. Regardless of the amplification problem, our toroidal magnetic loop idea could qualitatively explain the geometry of Hale’s law.

The planets move against the trailing Parker spiral. If the dragging of Parker spiral FTE magnetic flux ropes transfers some kinetic energy from the planet motion to the solar convective zone, this effect is strongest at the solar equator. It may have accumulated during the lifetime of the Sun, and explain the solar differential rotation.

The diameters of the sunspots, the Earth, Jupiter, and Mercury share some interesting connections that may not be accidental. The sunspot diameters are between 16 km and to 160 000 km (Birch and Bromage, 2022). The FTE magnetic flux rope diameters of the Earth, Jupiter and Mercury are comparable to the diameters of these three planets (Table 14). Our results indicate that the Earth may have the strongest influence on the sunspot cycle (Table 13: Com=2 and 6). The average diameter of sunspots is about same as the diameter of the Earth (Macdonald,

**Table 14.** Observed flux rope diameter upper limits. (1-3) Mercury: Diameter ( $D$ ), Number of FTEs ( $n_{\text{FTE}}$ ), Reference. (4-6) Same for the Earth. (7-9) Same for Jupiter. Notation “-” means that  $n_{\text{FTE}}$  is unknown.

Mercury			Earth			Jupiter		
(1) $D$ ( $R_{\text{Mercury}}$ )	(2) $n_{\text{FTE}}$ (-)	(3) Reference	(4) $D$ ( $R_{\text{Earth}}$ )	(5) $n_{\text{FTE}}$ (-)	(6) Reference	(7) $D$ ( $R_{\text{Jupiter}}$ )	(8) $n_{\text{FTE}}$ (-)	(9) Reference
1.04	5	2	2	152	1	3*	4	4
0.61	-	3	0.47	1	5	0.19	2	8
1.48	16	6	1.25	55	7	0.24	1	9

References: (1) Rijnbeek et al. (1984), (2) Slavin et al. (2010), (3) Slavin et al. (2012), (4) Vogt et al. (2014), (5) Hasegawa et al. (2015), (6) DiBraccio et al. (2015), (7) Akhavan-Tafti et al. (2018), (8) Sarkango et al. (2021), (9) Sarkango et al. (2022).

\*Mean diameter of 43 plasmoids: Only 4 of these plasmoids were classified as flux ropes.

2012; Luminița, Laurențiu, and Constantina, 2023). The largest sunspot diameters are close to Jupiter’s 140 000 km diameter. About  $8.1 \pm 0.5\%$  of all sunspots do not obey the Hale’s law (Li, 2018). If these smaller and weaker “anti-Hale” sunspots were connected to Mercury, their fraction would agree with  $R_{\text{Magnetic}} = 0.085$  for Mercury (Table 13: Com=2). Mercury is close to the Sun, where the Parker spiral trailing is small. Therefore, this trailing does not necessarily determine the order of the leading and trailing footpoints of all toroidal magnetic loops caused by Mercury’s FTEs. All these planetary diameter details fit to the strongest influence of the Earth, Jupiter and Mercury, and especially in this particular order (Table 13: Com=2 and 6).

We performed an extensive ADS database<sup>6</sup> literature search for studies connecting the FTEs to the sunspots. Only two studies proposed that the FTEs may be connected to the formation of sunspots (Pease and Glenn, 2016) and to the sunspot cycles (Glenn, 2019). We present direct observational evidence that the signals in the sunspot data may be connected to the planetary motions and the FTEs. It is possible that the planetary motions can influence the solar cycle, but it is impossible that the solar magnetic field can influence the planetary motions. As far as we know, ours would be the first *direct* detection of the Earth and Jupiter from the sunspot data. The possible detections of Venus and Mercury are uncertain due to physical reasons (Equation 46), as well as for statistical reasons (Appendix: Equations 53 and 57)

Even if the CS-estimate (Cranmer and Saar, 2007) and our relative magnetic interaction estimate (Equation 46) were invalid, every toroidal FTE magnetic flux rope distorts the poloidal solar dipole field. This field is also weakened by the magnetic flux through the FTE magnetic flux ropes. If the above two estimates are valid, the Earth, due to its iron core (Jephcoat and Olson, 1987), is an exceptional planet in the solar system. Direct observations of Earth-like exoplanets are difficult (Jenkins et al., 2015). If Earth-like planets can cause stellar activity cycles, innumerable indirect detections of such exoplanets have already been made (e.g. Baliunas and Vaughan, 1985). This would mean that the planets can cause the starspots, which in turn can prevent the detection of these planets (Korhonen et al., 2015). There may indeed also be a connection between stellar activity and exoplanets (e.g. Cuntz, Saar, and Musielak, 2000).

Astrophysical theories are used to construct models of astronomical phenomena. Observations are used to test these models. Statistical methods are not confined to any particular phenomenon.

<sup>6</sup>[NASA ADS-database](#).

The same statistical method can be applied to different phenomena. No phenomenon can fool statistics. Our statistical DCM can detect combinations of phenomena that are repeated (Equation 6:  $h(t)$ ) and not repeated (Equation 8:  $p(t)$ ). Phenomena are not stochastic only because they appear unpredictable. Phenomena may appear stochastic because we can not yet predict them. Both DCM and DFT detect the same extremely significant signals that can predict sunspot data. This does not support the mainstream dynamo-influence-theory  $H_{\text{Dynamo}}$  hypothesis of a stochastic sunspot cycle. From the time series analysis point of view, this is a clear-cut case. Our results support the deterministic planetary-influence-theory  $H_{\text{Planet}}$  hypothesis.

## 8. Conclusions

As for time series analysis, our planetary signal detections from the sunspot data are absolutely certain. However, our astrophysical results suffer from these three major uncertainties:

1. Is Cranmer and Saar (2007, Equation 2) estimate valid during Flux Transfer Events (FTEs)?
2. Do some FTE magnetic flux ropes transform into toroidal magnetic loops?
3. Does some physical mechanism amplify the fields of toroidal magnetic loops?

We present evidence that the accumulated effect of the Earth's, Jupiter's and Mercury's FTEs may cause the sunspot cycle. This might also explain the Hale's law, the formation of sunspot pairs, the solar differential rotation and many other phenomena observed in the Sun, as well as in other chromospherically active stars.

If we are correct, not a lot will remain of the current mainstream dynamo theory.

The predictability of solar activity will allow us to prepare better for the climate change on the Earth and the catastrophic geomagnetic storms, like the Carrington event in the year 1859.

## Appendix

### A. Statistics for planetary signal identification

In Section 4, we applied the DCM to search for periods between 5 and 200 years. The periods of the inner planets Mercury ( $P_{\text{Mercury}}$ ), Venus ( $P_{\text{Venus}}$ ), the Earth ( $P_{\text{Earth}}$ ) and Mars ( $P_{\text{Mars}}$ ) are outside this interval. We can not search for these planets in the yearly sunspot data, because their periods are close to, or below, the one-year window period.

The monthly sunspot data can be used to search for these shorter planetary periods. Our DCM analysis in the period range between 0.1 and 5 years reveals no signs of inner planet periods (DCM-manual: Section A). We can conclude that the periods of Mercury, Venus, the Earth and Mars can not be found *directly* from the monthly sunspot data. This does not, however, mean that we can not search for multiples of these periods above the five year limit  $P_{\text{max}} = 5$ . These periods  $iP_{\text{Planet}}$  are called "integer multiple periods", where  $P_{\text{Planet}}$  is planet's orbital period and  $i = 1, 2, 3, \dots$  is an integer. The aim is to find those integers that fit the detected signal periods, like  $i = 11$  for the strongest  $S_{11y}$  signal.

This Appendix describes the statistics of integer multiple period identification. We will show that it is difficult to identify the integer multiple periods of Mercury and Venus from the sunspot data. These identifications are easier for the Earth and Jupiter. The connections between these integer multiple periods and the planetary motions are also discussed.

Before we begin the search for integer multiple periods, the following possible misunderstandings must be corrected. Firstly, all detected signals are already given in Table 6. We are not fitting

multiples of planetary signals into the data. Secondly, the identification of these multiples is not numerology. We are only trying to identify the most obvious multiples that could be connected to the planets.

We have introduced the following nine signal abbreviations  $S_{11y}$ ,  $S_{10y}$ ,  $S_{11.y86}$ ,  $S_{110y}$ ,  $S_{10.y6}$ ,  $S_{8.y4}$ ,  $S_{53y}$ ,  $S_{8y}$  and  $S_{66y}$  in Table 6, where these signals were arranged in the order of decreasing strength, or equivalently, decreasing signal amplitude. The numerical value given in the signal subscript refers to the approximate signal period in Earth years.

These nine signals are now rearranged into the order of increasing periods  $S_{8y}$ ,  $S_{8.y4}$ ,  $S_{10y}$ ,  $S_{10.y6}$ ,  $S_{11y}$ ,  $S_{11.y86}$ ,  $S_{53y}$ ,  $S_{66y}$  and  $S_{110y}$  in our next Tables 15 and 16. We study only the signals detected in all data samples, because we get the same results for the predictive data samples (i.e., the subsets of all data samples). We select only those all data samples, where DCM detects more than two signals. The period ( $P$ ), the primary minimum epoch ( $t_{\min,1}$ ) and the primary maximum epoch ( $t_{\max,1}$ ) of all  $S_{8y}$ ,  $S_{8.y4}$ ,  $S_{10y}$ ,  $S_{10.y6}$ ,  $S_{11y}$ ,  $S_{11.y86}$ ,  $S_{53y}$ ,  $S_{66y}$  and  $S_{110y}$  signals are given in Table 15. The units of these three parameters are Earth years.

We are accustomed to measuring time and periodicity in Earth years. The Earth year signal periods detected in all data samples are transformed into Mercury, Venus and Jupiter year signal periods in Tables 15 and 16. It is easier to identify integer multiple periods from these values. We use the known planet period  $P_{\text{Planet}}$  in Earth years to compute four dimensionless parameters

$$\mathcal{P} = P/P_{\text{Planet}} \quad (49)$$

$$\sigma_{\mathcal{P}} = \sigma_P/P_{\text{Planet}} \quad (50)$$

$$\Delta\mathcal{P} = \mathcal{P} - \mathcal{P}_0 \quad (51)$$

$$\Delta\mathcal{P}_{\text{rel}} = \frac{|\Delta\mathcal{P}|}{\sigma_{\mathcal{P}}}, \quad (52)$$

where  $\mathcal{P}_0$  is the integer value closest to  $\mathcal{P}$ . The two first parameters  $\sigma_{\mathcal{P}}$  and  $\mathcal{P}$  are hereafter called “rounds error” and “rounds” (number of planet revolutions around the Sun). The next two parameters  $\Delta\mathcal{P}$  and  $\Delta\mathcal{P}_{\text{rel}}$  are called “rounds deviation” and “relative rounds deviation”. Note that we introduce a new letter “ $\mathcal{P}$ ” to highlight the difference from the period letter “ $P$ ”.

For any detected period  $P \pm \sigma_P$ , the rounds error is  $\sigma_{\mathcal{P}} \propto \sigma_P/P_{\text{Planet}}$ . This rounds error  $\sigma_{\mathcal{P}}$  is larger for the inner planets Mercury and Venus having  $P_{\text{Planet}} < P_{\text{Earth}} = 1$ , and smaller for Jupiter having  $P_{\text{Planet}} > P_{\text{Earth}} = 1$ . For example, the period  $P = 8.1087 \pm 0.0076$  gives the following  $\sigma_{\mathcal{P}} = 0.032$  (Mercury),  $\sigma_{\mathcal{P}} = 0.012$  (Venus),  $\sigma_{\mathcal{P}} = 0.0076$  (Earth) and  $\sigma_{\mathcal{P}} = 0.000064$  (Jupiter) rounds error values (Table 15: Rmonthly,  $K_2 = 1$  model, signal  $S_{8y}$ ). This means that the period of Jupiter is easiest to identify from the  $\mathcal{P}$  rounds values. On the other hand, the identifications of Mercury and Venus from the  $\mathcal{P}$  rounds values are the most difficult ones, and especially in this order. Furthermore, the correct  $\mathcal{P}_0$  rounds value becomes uncertain, if the round error  $\sigma_{\mathcal{P}}$  exceeds  $1/2$ , i.e. half a revolution around the Sun. This complication effect is strongest for the longest detected periods  $P$ , which have the largest  $\sigma_{\mathcal{P}}$  errors in Tables 15 and 16.

The larger rounds error  $\sigma_{\mathcal{P}}$  values of Mercury and Venus cause another effect that makes the identification of their signals even more difficult. If the rounds deviation  $\Delta\mathcal{P}$  values are drawn from a Gaussian distribution having a mean  $\mathcal{P}_0$  and a standard deviation  $\sigma_{\mathcal{P}}$ , the probability

$$P(|\Delta\mathcal{P}| \geq |\Delta\mathcal{P}'|) \quad (53)$$

for  $|\Delta\mathcal{P}|$  exceeding any fixed large rounds deviation  $|\Delta\mathcal{P}'|$  value increases for larger rounds error  $\sigma_{\mathcal{P}}$  values. In other words, large  $|\Delta\mathcal{P}|$  values are more probable for Mercury and Venus than for the Earth and Jupiter. This increases the probability of stronger mean anomaly migration  $\Delta M$  for Mercury and Venus (see Equation 57).

**Table 15.** Signals detected in all data samples. (1) Signal parameters. (2-6) Samples: pure sine model ( $K_2 = 1$ ) and double wave models ( $K_2 = 2$ ). Three double sinusoid signals are denoted with “ $2\times$ ”. Notes below give detailed instructions of how to read column (1) signal parameters.

(1)	(2) Rmonthly: $K_2 = 1$	(3) Rmonthly: $K_2 = 2$	(4) Cmonthly: $K_2 = 1$	(5) Ryearly: $K_2 = 1$	(6) Cyearly: $K_2 = 1$
Signal $S_{8y} \cong 13 \times P_{Venus} \cong 8 \times P_{Earth}$					
Rank	(7)	(8)	(5)	(5)	
$P$	$8.1087 \pm 0.0076$	$8.169 \pm 0.014$	$8.009 \pm 0.017$	$8.005 \pm 0.058$	
$t_{\min,1}$	$1751.29 \pm 0.14$	$1750.90 \pm 0.51$	$1818.07 \pm 0.24$	$1826.09 \pm 0.68$	
$t_{\max,1}$	$1755.34 \pm 0.14$	$1754.37 \pm 0.26$	$1822.08 \pm 0.24$	$1822.09 \pm 0.70$	
$P/P_{Mercury}$	$33.674 \pm 0.032$	$33.924 \pm 0.058$	$33.260 \pm 0.070$	$33.24 \pm 0.24$	
$P/P_{Venus}$	$13.180 \pm 0.012$	$13.279 \pm 0.023$	$13.018 \pm 0.028$	$13.012 \pm 0.094$	
$P/P_{Jupiter}$	$0.68359 \pm 0.00064$	$0.6887 \pm 0.0012$	$0.6752 \pm 0.0014$	$0.6748 \pm 0.0049$	
Signal $S_{8,y,4} \cong 35 \times P_{Mercury}$					
Rank	(6)	(7)			
$P$	$16.753 \pm 0.027$ <sup>2×</sup>		$8.466 \pm 0.016$		
$t_{\min,1}$	$1759.19 \pm 0.23$		$1707.10 \pm 0.35$		
$t_{\max,1}$	$1754.70 \pm 0.26$		$1702.86 \pm 0.35$		
$P/P_{Mercury}$	$69.57 \pm 0.11$ <sup>2×</sup>		$35.158 \pm 0.066$		
$P/P_{Venus}$	$27.232 \pm 0.044$ <sup>2×</sup>		$13.761 \pm 0.026$		
$P/P_{Jupiter}$	$1.4123 \pm 0.0023$ <sup>2×</sup>		$0.7137 \pm 0.0013$		
Signal $S_{10y} \cong 41.5 \times P_{Mercury} \cong 10 \times P_{Earth}$					
Rank	(2)	(2)	(2)	(2)	
$P$	$10.0001 \pm 0.0081$	$20.0062 \pm 0.0088$ <sup>2×</sup>	$10.0659 \pm 0.0077$	$9.975 \pm 0.017$	$10.058 \pm 0.026$
$t_{\min,1}$	$1754.16 \pm 0.11$	$1754.284 \pm 0.063$	$1823.52 \pm 0.12$	$1704.63 \pm 0.35$	$1823.55 \pm 0.25$
$t_{\max,1}$	$1749.16 \pm 0.11$	$1749.282 \pm 0.067$	$1818.48 \pm 0.12$	$1709.62 \pm 0.34$	$1818.52 \pm 0.26$
$P/P_{Mercury}$	$41.529 \pm 0.034$	$83.082 \pm 0.036$ <sup>2×</sup>	$41.802 \pm 0.032$	$41.424 \pm 0.070$	$41.77 \pm 0.11$
$P/P_{Venus}$	$16.255 \pm 0.013$	$32.520 \pm 0.014$ <sup>2×</sup>	$16.362 \pm 0.012$	$16.214 \pm 0.028$	$16.349 \pm 0.042$
$P/P_{Jupiter}$	$0.84304 \pm 0.00068$	$1.68658 \pm 0.00074$ <sup>2×</sup>	$0.84858 \pm 0.00065$	$0.8409 \pm 0.0014$	$0.8479 \pm 0.0022$
Signal $S_{10,y,6} \cong 44 \times P_{Mercury}$					
Rank	(5)	(5)	(3)		
$P$	$10.569 \pm 0.020$	$10.5407 \pm 0.0060$	$10.659 \pm 0.031$		
$t_{\min,1}$	$1753.03 \pm 0.27$	$1754.40 \pm 0.13$	$1709.27 \pm 0.44$		
$t_{\max,1}$	$1758.31 \pm 0.26$	$1758.307 \pm 0.091$	$1703.94 \pm 0.46$		
$P/P_{Mercury}$	$43.891 \pm 0.083$	$43.774 \pm 0.025$	$44.26 \pm 0.13$		
$P/P_{Venus}$	$17.180 \pm 0.032$	$17.1338 \pm 0.0098$	$17.326 \pm 0.050$		
$P/P_{Jupiter}$	$0.89100 \pm 0.0017$	$0.88861 \pm 0.00050$	$0.8986 \pm 0.0026$		
Signal $S_{11y} \cong 11 \times P_{Earth}$					
Rank	(1)	(1)	(1)	(1)	
$P$	$11.0033 \pm 0.0064$	$10.9878 \pm 0.0051$	$10.8585 \pm 0.0048$	$10.981 \pm 0.020$	$10.863 \pm 0.022$
$t_{\min,1}$	$1755.897 \pm 0.076$	$1756.678 \pm 0.077$	$1823.580 \pm 0.053$	$1700.86 \pm 0.24$	$1823.56 \pm 0.20$
$t_{\max,1}$	$1750.395 \pm 0.078$	$1750.262 \pm 0.087$	$1818.150 \pm 0.055$	$1706.35 \pm 0.23$	$1828.99 \pm 0.19$
$P/P_{Mercury}$	$45.695 \pm 0.026$	$45.630 \pm 0.021$	$45.093 \pm 0.020$	$45.602 \pm 0.083$	$45.112 \pm 0.091$
$P/P_{Venus}$	$17.886 \pm 0.010$	$17.8605 \pm 0.0083$	$17.6504 \pm 0.0078$	$17.849 \pm 0.032$	$17.658 \pm 0.036$
$P/P_{Jupiter}$	$0.92761 \pm 0.00054$	$0.92630 \pm 0.00043$	$0.91540 \pm 0.00040$	$0.9257 \pm 0.0017$	$0.9158 \pm 0.0018$
Signal $S_{11,y,86} \cong 49 \times P_{Mercury} \cong 1 \times P_{Jupiter}$					
(3)	(4)	(4)	(5)	(4)	
$P$	$11.806 \pm 0.012$	$11.770 \pm 0.011$	$11.863 \pm 0.021$	$11.820 \pm 0.027$	$11.856 \pm 0.068$
$t_{\min,1}$	$1760.33 \pm 0.13$	$1749.51 \pm 0.15$	$1818.92 \pm 0.20$	$1701.01 \pm 0.41$	$1818.95 \pm 0.69$
$t_{\max,1}$	$1754.42 \pm 0.14$	$1754.40 \pm 0.21$	$1824.85 \pm 0.19$	$1706.92 \pm 0.41$	$1824.88 \pm 0.66$
$P/P_{Mercury}$	$49.028 \pm 0.050$	$48.879 \pm 0.046$	$49.265 \pm 0.087$	$49.09 \pm 0.11$	$49.24 \pm 0.28$
$P/P_{Venus}$	$19.190 \pm 0.020$	$19.132 \pm 0.018$	$19.283 \pm 0.034$	$19.213 \pm 0.044$	$19.27 \pm 0.11$
$P/P_{Jupiter}$	$0.9953 \pm 0.0010$	$0.99224 \pm 0.00093$	$1.0001 \pm 0.0018$	$0.9964 \pm 0.0023$	$0.9995 \pm 0.0057$
Signal $S_{53y} \cong 4.5P_{Jupiter}$					
Rank	(6)		(6)		
$P$	$52.66 \pm 0.27$		$53.83 \pm 0.76$		
$t_{\min,1}$	$1759.63 \pm 0.70$		$1704.5 \pm 2.7$		
$t_{\max,1}$	$1785.94 \pm 0.60$		$1731.4 \pm 2.3$		
$P/P_{Mercury}$	$218.7 \pm 1.1$		$223.5 \pm 3.2$		
$P/P_{Venus}$	$85.60 \pm 0.44$		$87.5 \pm 1.2$		
$P/P_{Jupiter}$	$4.439 \pm 0.023$		$4.538 \pm 0.064$		
Signal $S_{66y} \cong 5.5 \times P_{Jupiter}$ or $6.0 \times P_{Jupiter}$					
Rank	(7)		(8)		
$P$	$143.39 \pm 0.99$ <sup>2×</sup>		$66.7 \pm 1.4$		
$t_{\min,1}$	$1887.84 \pm 0.80$		$1753.0 \pm 3.8$		
$t_{\max,1}$	$1784.2 \pm 1.1$		$1719.6 \pm 4.4$		
$P/P_{Mercury}$	$595.5 \pm 4.1$ <sup>2×</sup>		$277.0 \pm 5.8$		
$P/P_{Venus}$	$233.1 \pm 1.6$ <sup>2×</sup>		$108.4 \pm 2.3$		
$P/P_{Jupiter}$	$12.088 \pm 0.083$ <sup>2×</sup>		$5.62 \pm 0.12$		
Signal $S_{110y} \cong$ Synodic periods of Equation 40 (Table 8)					
(4)	(3)	(3)	(4)	(3)	
$P$	$99.92 \pm 0.57$	$104.23 \pm 0.68$	$116.7 \pm 1.3$	$101.4 \pm 2.4$	$115.6 \pm 3.6$
$t_{\min,1}$	$1811.99 \pm 0.84$	$1811.37 \pm 0.68$	$1911.02 \pm 0.74$	$1710.5 \pm 3.4$	$1910.4 \pm 2.1$
$t_{\max,1}$	$1762.0 \pm 1.1$	$1844.00 \pm 0.48$	$1852.7 \pm 1.1$	$1761.2 \pm 2.5$	$1852.6 \pm 2.6$
$P/P_{Mercury}$	$415.0 \pm 2.4$	$432.8 \pm 2.8$	$484.6 \pm 5.4$	$421 \pm 10$	$480 \pm 15$
$P/P_{Venus}$	$162.42 \pm 0.93$	$169.4 \pm 1.1$	$189.7 \pm 2.1$	$164.8 \pm 3.9$	$187.9 \pm 5.8$
$P/P_{Jupiter}$	$8.424 \pm 0.048$	$8.787 \pm 0.057$	$9.84 \pm 0.11$	$8.55 \pm 0.20$	$9.74 \pm 0.30$

**Notes.** Column 1 specifies seven parameters for each sample. For example, seventh strongest “(7)” signal  $S_{8y}$  for Rmonthly ( $K_2 = 1$ ) has period  $P \pm \sigma_P = 8.1087 \pm 0.0076$  in Earth years. Primary minima and maxima of this signal are at years  $t_{\min,1} = 1751.29 \pm 0.14$  and  $t_{\max,1} = 1755.34 \pm 0.14$ . Rounds  $P \pm \sigma_P$  values are  $(P \pm \sigma_P)/P_{Mercury} = 33.674 \pm 0.032$ ,  $(P \pm \sigma_P)/P_{Venus} = 13.180 \pm 0.012$  and  $(P \pm \sigma_P)/P_{Jupiter} = 0.68359 \pm 0.00064$ .

Do the planets cause the starspot cycles?

**Table 16.** Detected planetary signal candidates. (1) Sample ( $K_2 = 1 \equiv$  pure sine model,  $K_2 = 2 \equiv$  double wave model), (2) Time span. (3) Period. (4) Rounds (Equations 49 and 50). (5) Rounds deviation (Equation 51). (6) Relative rounds deviation (Equation 52). (7) Mean anomaly migration  $\Delta M/360^\circ$  (Equation 57). (8) Planet revolutions during  $\Delta T$ . (9) Relative mean anomaly migration  $\Delta M/360^\circ$  (Equation 58). (10) Displaying figure and symbol colour.

(1) Sample ( $K_2$ )	(2) $\Delta T$ (y)	(3) $P \pm \sigma_P$ (y)	(4) $\mathcal{P} \pm \sigma_{\mathcal{P}}$ (-)	(5) $\Delta \mathcal{P}$ (-)	(6) $\Delta \mathcal{P}_{\text{rel}}$ (-)	(7) $\frac{\Delta M}{360^\circ}$ (-)	(8) $\frac{\Delta T}{P_{\text{Planet}}}$ (-)	(9) $\frac{\Delta M_{\text{rel}}}{360^\circ}$ (-)	(10) Figure
Signal $S_{8y}: \cong 13 \times P_{\text{Venus}}$									
Rmonthly( $K_2 = 1$ )	273.8	$8.1087 \pm 0.0076$	$13.180 \pm 0.012$	0.180	15.0	6.1	445	0.014	12a: red
Rmonthly( $K_2 = 2$ )	273.8	$8.169 \pm 0.014$	$13.279 \pm 0.023$	0.279	12.1	9.4	445	0.021	12a: blue
Cmonthly( $K_2 = 1$ )	204.8	$8.009 \pm 0.017$	$13.018 \pm 0.028$	0.018	0.90	0.46	333	0.0014	12a: green
Cyearly( $K_2 = 1$ )	203.0	$8.005 \pm 0.058$	$13.012 \pm 0.094$	0.012	0.13	0.30	330	0.00092	12a: cyan
Signal $S_{8y}: \cong 8 \times P_{\text{Earth}}$									
Rmonthly( $K_2 = 1$ )	273.8	$8.1087 \pm 0.0076$	$8.1087 \pm 0.0076$	0.1087	14.3	3.7	273.8	0.013	12b: red
Rmonthly( $K_2 = 2$ )	273.8	$8.169 \pm 0.014$	$8.169 \pm 0.014$	0.169	12.1	5.7	273.8	0.021	12b: blue
Cmonthly( $K_2 = 1$ )	204.8	$8.009 \pm 0.017$	$8.009 \pm 0.017$	0.009	0.53	0.23	204.8	0.0011	12b: green
b Cyearly( $K_2 = 1$ )	203.0	$8.005 \pm 0.058$	$8.005 \pm 0.058$	0.005	0.086	0.13	203.0	0.00062	12b: cyan
Signal $S_{8,y4}: \cong 35 \times P_{\text{Mercury}}$									
Ryearly( $K_1 = 1$ )	321.0	$8.466 \pm 0.016$	$35.158 \pm 0.066$	0.158	2.4	6.0	1333	0.0045	None
Signal $S_{10y}: 41.5 \times P_{\text{Mercury}}$									
Rmonthly( $K_2 = 1$ )	273.8	$10.0001 \pm 0.0081$	$41.529 \pm 0.034$	0.029	0.85	0.79	1137	0.00070	12c: red
Cmonthly( $K_2 = 1$ )	204.8	$10.0659 \pm 0.0077$	$41.802 \pm 0.032$	0.302	9.4	6.2	851	0.0072	12c: green
Ryearly( $K_2 = 1$ )	321.0	$9.975 \pm 0.017$	$41.424 \pm 0.070$	-0.076	1.1	-2.4	1333	0.0018	12c: yellow
Cyearly( $K_2 = 1$ )	203.0	$10.058 \pm 0.026$	$41.77 \pm 0.11$	0.27	2.4	5.4	843	0.0065	12c: cyan
Signal $S_{10y}: \cong 10.0 \times P_{\text{Earth}}$									
Rmonthly( $K_2 = 1$ )	273.8	$10.0001 \pm 0.0081$	$10.0001 \pm 0.0081$	0.0001	0.012	0.0027	273.8	0.000010	12d: red
Cmonthly( $K_2 = 1$ )	204.8	$10.0659 \pm 0.0077$	$10.0659 \pm 0.0077$	0.0659	8.6	1.3	204.8	0.0065	12d: green
Ryearly( $K_2 = 1$ )	321.0	$9.975 \pm 0.017$	$9.975 \pm 0.017$	-0.025	1.5	-0.80	321	0.0025	12d: yellow
Cyearly( $K_2 = 1$ )	203.0	$10.058 \pm 0.026$	$10.058 \pm 0.026$	0.058	2.3	1.2	203	0.0058	12d: cyan
Signal $S_{10,y6}: \cong 44 \times P_{\text{Mercury}}$									
Rmonthly( $K_2 = 1$ )	273.8	$10.569 \pm 0.020$	$43.891 \pm 0.083$	-0.109	1.3	-2.8	1137	0.0025	13a: red
Rmonthly( $K_2 = 2$ )	273.8	$10.5407 \pm 0.0060$	$43.774 \pm 0.025$	-0.226	9.0	-5.9	1137	0.0052	13a: blue
Ryearly( $K_2 = 1$ )	321.0	$10.659 \pm 0.031$	$44.26 \pm 0.13$	0.26	2.0	7.8	1333	0.0059	13a: yellow
Signal $S_{11y}: \cong 11.0 \times P_{\text{Earth}}$									
Rmonthly( $K_2 = 1$ )	273.8	$11.0033 \pm 0.0064$	$11.0033 \pm 0.0064$	0.0033	0.52	0.082	273.8	0.00030	13b: red
Rmonthly( $K_2 = 2$ )	273.8	$10.9878 \pm 0.0051$	$10.9878 \pm 0.0051$	-0.0122	2.4	-0.30	273.8	0.0011	13b: blue
Cmonthly( $K_2 = 1$ )	204.8	$10.8585 \pm 0.0048$	$10.8585 \pm 0.0048$	-0.1415	29	-2.7	204.8	0.013	13b: green
Ryearly( $K_2 = 1$ )	321.0	$10.981 \pm 0.020$	$10.981 \pm 0.020$	-0.019	0.95	0.56	321.0	0.0017	13b: yellow
Cyearly( $K_2 = 1$ )	203.0	$10.863 \pm 0.022$	$10.863 \pm 0.022$	-0.137	6.2	-2.6	203.0	0.013	13b: cyan
Signal $S_{11,y86}: \cong 49.0 \times P_{\text{Mercury}}$									
Rmonthly( $K_2 = 1$ )	273.8	$11.806 \pm 0.012$	$49.028 \pm 0.050$	0.028	0.56	0.65	1137	0.00057	13c: red
Rmonthly( $K_2 = 2$ )	273.8	$11.770 \pm 0.011$	$48.879 \pm 0.046$	-0.121	2.6	-2.8	1137	0.0025	13c: blue
Cmonthly( $K_2 = 1$ )	204.8	$11.863 \pm 0.021$	$49.265 \pm 0.087$	0.265	3.0	4.6	850	0.0054	13c: green
Ryearly( $K_2 = 1$ )	321.0	$11.820 \pm 0.027$	$49.09 \pm 0.11$	0.09	0.82	2.4	1333	0.0018	13c: yellow
Cyearly( $K_2 = 1$ )	203.0	$11.856 \pm 0.068$	$49.24 \pm 0.28$	0.24	0.86	4.1	843	0.0049	13c: cyan
Signal $S_{11,y86}: \cong 1.0 \times P_{\text{Jupiter}}$									
Rmonthly( $K_2 = 1$ )	273.8	$11.806 \pm 0.012$	$0.9953 \pm 0.0010$	-0.0047	4.7	-0.11	23	0.0047	13d: red
Rmonthly( $K_2 = 2$ )	273.8	$11.770 \pm 0.011$	$0.99224 \pm 0.00093$	-0.0078	8.3	-0.18	23	0.0078	13d: blue
Cmonthly( $K_2 = 1$ )	204.8	$11.863 \pm 0.021$	$1.0001 \pm 0.0018$	0.00010	0.056	0.0017	17	0.00010	13d: green
Ryearly( $K_2 = 1$ )	321.0	$11.820 \pm 0.027$	$0.9964 \pm 0.0023$	-0.0036	1.6	-0.098	27	0.0036	13d: yellow
Cyearly( $K_2 = 1$ )	203.0	$11.856 \pm 0.068$	$0.9995 \pm 0.0057$	-0.00050	0.088	-0.0086	17	0.00050	13d: cyan
Signal $S_{53y}: \cong 4.5 \times P_{\text{Jupiter}}$									
Rmonthly( $K_2 = 1$ )	273.8	$52.66 \pm 0.27$	$4.439 \pm 0.023$	-0.061	2.6	-0.32	23	0.014	None
Ryearly( $K_2 = 1$ )	321.0	$53.83 \pm 0.76$	$4.538 \pm 0.064$	0.038	0.59	0.23	27	0.0084	None
Signal $S_{66y}: \cong 5.5 \times P_{\text{Jupiter}}$									
Ryearly( $K_2 = 1$ )	321.0	$66.7 \pm 1.4$	$5.62 \pm 0.12$	0.12	1.0	0.57	27	0.021	None

The primary minima and the primary maxima of the signals in Table 15 occur at multiples

$$T_{\min,k} = t_{\min,1} + kP \quad (54)$$

$$T_{\max,k} = t_{\max,1} + kP, \quad (55)$$

where  $k = 1, 2, \dots$  are integers. The units of  $P$ ,  $t_{\min,1}$  and  $t_{\max,1}$  are Earth years. The relation  $P = (\mathcal{P}_0 + \Delta\mathcal{P})P_{\text{Planet}}$  gives

$$T_{\min,k} = t_{\min,1} + kP = t_{\min,1} + k(\mathcal{P}_0 + \Delta\mathcal{P})P_{\text{Planet}} = t_{\min,1} + k\mathcal{P}_0P_{\text{Planet}} + k\Delta\mathcal{P}P_{\text{Planet}}$$

$$T_{\max,k} = t_{\max,1} + kP = t_{\max,1} + k(\mathcal{P}_0 + \Delta\mathcal{P})P_{\text{Planet}} = t_{\max,1} + k\mathcal{P}_0P_{\text{Planet}} + k\Delta\mathcal{P}P_{\text{Planet}}$$

The last term

$$\Delta t = k\Delta\mathcal{P}P_{\text{Planet}} \quad (56)$$

is the time difference between the multiples  $t_{\min,1} + kP$  and  $t_{\min,1} + k\mathcal{P}_0P_{\text{Planet}}$ , and between the multiples  $t_{\max,1} + kP$  and  $t_{\max,1} + k\mathcal{P}_0P_{\text{Planet}}$ .

The data time span  $\Delta T$  contains  $\Delta T/P$  multiples of  $P$ . Using  $k = \Delta T/P$  in Equation 56 gives

$$\Delta t = \frac{\Delta\mathcal{P}\Delta T}{P}P_{\text{Planet}}$$

time difference during  $\Delta T$ . We convert time difference  $\Delta t$  into planet “mean anomaly migration”

$$\Delta M = \frac{\Delta t}{P_{\text{Planet}}} \times 360^\circ = \frac{\Delta\mathcal{P}\Delta T}{P} \times 360^\circ, \quad (57)$$

where the units of  $\Delta M$  are degrees. For all  $\Delta T$  and  $P$  combinations, this relation shows that larger mean anomaly  $\Delta M$  migration occurs for larger  $\Delta\mathcal{P}$  values, which are most probable for Mercury and Venus (Equation 53). The “relative mean anomaly migration” during each  $P_{\text{Planet}}$  revolution is

$$\Delta M_{\text{rel}} = |\Delta M| / \left( \frac{\Delta T}{P_{\text{Planet}}} \right) \times 360^\circ = |\Delta\mathcal{P}| \frac{P_{\text{Planet}}}{P} \times 360^\circ. \quad (58)$$

For any particular signal, the period  $P$  detected in each sample determines the linear mean anomaly migration  $\Delta M$  during the  $\Delta T$  time span of the data (Equation 57). The slope of this linear  $M(t)$  mean anomaly migration is  $(\Delta\mathcal{P}/P) \times 360^\circ$  (Equation 57). Let us assume that these mean anomaly migration lines

$$\frac{\Delta\mathcal{P}}{P}(t - t_C) \times 360^\circ = M(t) - M_C \quad (59)$$

of different samples intersect close to a “convergence point”  $(t_C, M_C)$ . This means that the mean anomaly value of each line is  $M(t) \approx M_C$  at epoch  $t = t_C$ . The slope of all these  $M(t)$  lines approaches zero, if  $\Delta\mathcal{P} \rightarrow 0 \equiv \mathcal{P} \rightarrow \mathcal{P}_0 \equiv P \rightarrow P_{\text{planet}}$ . In this case, all lines fulfil

$$M(t) \approx M_C \quad (60)$$

for all  $t$  values. If the mean anomaly  $M(t)$  lines for the same signal are detected in different samples, and these lines show a convergence point  $(t_C, M_C)$ , then the periods  $P$ , the minimum epochs  $t_{\min,1}$  and the maximum epochs  $t_{\max,1}$  of all these signals can be connected to each other. The presence of this convergence point confirms that the individual signals detected in

different samples can represent the same real signal having the same period, and the same phase. The statistical fluctuation of  $|\Delta\mathcal{P}|$  rounds deviations (Equation 53) complicate the detection of this “convergence point connection”. We have already shown that the probability for larger  $|\Delta\mathcal{P}|$  values increases when  $\sigma_{\mathcal{P}}$  increases for smaller  $P_{\text{Planet}}$  periods. These  $|\Delta\mathcal{P}|$  fluctuations are largest for Mercury and Venus. Therefore, the mean anomaly migration  $\Delta M$  lines of these inner planets are “messier”, and their convergence point locations are more difficult to detect. Hence, the detection of Jupiter and the Earth from the *same* sunspot data is easier than the detection of Venus and Mercury.

The relations of Equations 57 - 60 are formulated for the mean anomaly  $M$ , because this parameter has a linear connection to time. We compute the true anomaly  $\nu_{\min}$  and  $\nu_{\max}$  values from the mean anomaly values  $M$  for the minimum epochs  $t_{\min,1}$  and the maximum epochs  $t_{\max,1}$  (Equations 54 and 55) given in Table 15. The mean anomaly  $M$  and the true anomaly  $\nu$  value differences are small for Venus, the Earth and Jupiter, which have nearly circular orbits. The large Mercury’s orbit eccentricity  $e = 0.20$  can cause clear  $\nu$  deviations from the linear  $M$  trend (e.g. Figure 13c).

We search for signatures of Mercury, Venus, the Earth and Jupiter from the  $S_{8y}$ ,  $S_{8,y4}$ ,  $S_{10y}$ ,  $S_{10,y6}$ ,  $S_{11y}$ ,  $S_{11,y86}$ ,  $S_{53y}$ ,  $S_{66y}$  and  $S_{110y}$  signals. The results for this “wide search” of 36 alternatives are given in Table 15. We summarise the most promising planetary signal candidate detections in Table 16. The three double sinusoid signals “ $2\times$ ” are given in Table 15. We exclude these double sinusoids from Table 16, because the minor asymmetries of these double sinusoid  $2 \times P$  period curves can mislead the identification of convergence points (Equation 59).

In our next figures, we plot the  $\nu_{\min}$  and  $\nu_{\max}$  values for numerous sample, signal and planet combinations. In every figure, we use the same symbol colour for the signals detected in the same sample. All samples end in the same year 2022, but they begin at different years between 1700 and 1815. This complicates the detection of convergence points, if they are located outside some sample(s). We solve this problem by computing the  $\nu_{\min}$  and  $\nu_{\max}$  values of all samples for the whole time interval between the years 1700 and 2022. The symbols for the  $\nu_{\min}$  and  $\nu_{\max}$  values *inside* each sample are highlighted with a black circle around the coloured symbol. This black circle is missing from the symbols representing  $\nu_{\min}$  and  $\nu_{\max}$  values *outside* each sample. We can use these outside values to check, if the signals detected in each sample can predict the presence of a convergence point before the beginning of this sample.

The detected signals are the  $h_i(t)$  functions (Equation 7) in the sum  $h(t)$  of all signals (Equation 6). For the symmetric pure sine model  $h_i(t)$  functions, the separation between the primary minimum epoch  $t_{\min,1}$  and the primary maximum epoch  $t_{\max,1}$  is exactly  $P/2$ . If the period of the detected signal  $P$  is an *even* multiple of the planet’s period  $P_{\text{Planet}}$ , the mean anomaly  $M$  values are equal at all minima  $T_{\min,k}$  and maxima  $T_{\max,k}$  (Equations 54 and 55). Except for the possible deviations caused by the planetary orbit eccentricity, the  $\nu_{\min}$  and  $\nu_{\max}$  values will also be equal. This “overlapping effect” occurs in Figures 12b, 12d and 13a. If the detected period  $P$  is an *uneven*  $P_{\text{Planet}}$  multiple, the differences between the mean anomaly  $M$  values of all minima  $T_{\min,k}$  and maxima  $T_{\max,k}$  are equal to 180 degrees. The planetary orbit eccentricity can, again, cause deviations from this 180 degrees difference between the true anomalies  $\nu_{\min}$  and  $\nu_{\max}$ . This 180 degrees “separation effect” occurs in Figures 12a, 13b, 13c and 13d. The asymmetries of double wave models can also cause deviations from the overlapping effect and 180 degrees separation effect, like those seen in the blue circles of Figures 12b, 13a, 13b and 13d.

### A.1. Signal $S_{8y}$

The shortest period  $S_{8y}$  signal is close to  $13 \times P_{\text{Venus}}$  and  $8 \times P_{\text{Earth}}$  (Tables 15 and 16). The known period ratio is  $8 \times P_{\text{Earth}}/P_{\text{Venus}} = 13.0039$ . Due to statistical  $\Delta\mathcal{P}$  fluctuations (Equations 53 and 57), the true anomaly migration curves of Venus in Figure 12a should appear less regular than those of Earth in Figure 12b. This is indeed the case.

### A.1.1. Signal $S_{8y} \cong 13 \times P_{\text{Venus}}$

The two rounds  $\mathcal{P} = 13.018 \pm 0.028$  and  $13.012 \pm 0.094$  values for the **Cmonthly** and **Cyearly** samples differ  $\Delta\mathcal{P}_{\text{rel}} = 0.90$  and  $0.13$  from  $13 \times P_{\text{Venus}}$  (Table 16: Signal  $S_{8y}$ ). The mean anomaly migration is  $\Delta M/360^\circ = 0.46$  and  $0.30$  revolutions during 205 and 203 years, respectively. The green and cyan circles highlighted with black circles show this weak positive upwards  $\nu_{\min}$  and  $\nu_{\max}$  true anomaly migration of Venus inside these **Cmonthly** and **Cyearly** samples (Figure 12a).

The other two rounds values for sample **Rmonthly** (pure sine and double wave models) are  $\mathcal{P} = 13.180 \pm 0.012$  and  $13.279 \pm 0.023$ . They differ  $\Delta\mathcal{P}_{\text{rel}} = 15.0$  and  $12.1$  from  $13 \times P_{\text{Venus}}$  (Table 16: Signal  $S_{8y}$ ). For these two  $\mathcal{P}$  rounds values, the strong positive upwards mean anomaly migration  $\Delta M/360^\circ$  is  $6.1$  and  $9.4$  revolutions during 274 years  $\equiv 445$  Venus revolutions. These values are equal to the relative mean anomaly migration  $\Delta M_{\text{rel}}/360^\circ = 0.014$  and  $0.021$  during one revolution of Venus. We show the respective true anomaly  $\nu_{\min}$  and  $\nu_{\max}$  migration in Figure 12a (red and blue circles).

The uneven  $13 \times P_{\text{Venus}}$  multiple causes the 180 degree separation effect of  $\nu_{\min}$  and  $\nu_{\max}$ . The migration lines of large circles denoting the  $\nu_{\max}$  values show a convergence point (Equation 59), which is highlighted with a large dotted blue circle at  $t_C = 1820$  years and  $\nu_C = 315$  degrees. The migration lines of smaller circles denoting the  $\nu_{\min}$  values converge at  $t_C = 1820$  years and  $\nu_C = 135$  degrees in the centre of the red large dotted circle. These two convergence points are at the beginning of **Cmonthly** and **Cyearly** samples, where the black circles begin to highlight the green and cyan circles. The detection of the two convergence points confirms that all four  $S_{8y}$  signals in Table 16 can be connected, regardless of the large true anomaly  $\nu$  migration of the two signals detected in **Rmonthly** (pure sine and double wave models). The apparently messy migration of red and blue circles in Figure 12a can arise, as expected, from the statistical  $\Delta\mathcal{P}$  fluctuations caused by the short orbital period of Venus (Equation 53).

### A.1.2. Signal $S_{8y} \cong 8 \times P_{\text{Earth}}$

The two  $P \pm \sigma_P = 8.009 \pm 0.017$  and  $8.005 \pm 0.058$  Earth year periods detected in the **Cmonthly** and **Cyearly** samples are equal to  $8 \times P_{\text{Earth}}$  comfortably within  $\pm 1\sigma_P$  (Table 16: Signal  $S_{8y}$ ). The mean anomaly migration  $\Delta M/360^\circ$  is only  $0.23$  and  $0.13$  revolutions in over two centuries (Figure 12b: green and cyan highlighted circles).

For the other two periods (**Rmonthly**: pure sine and double wave models), the rounds values  $\mathcal{P} = 8.1087 \pm 0.0076$  and  $8.169 \pm 0.014$  differ  $\Delta\mathcal{P}_{\text{rel}} = 14.3$  and  $12.1$  from  $8 \times P_{\text{Earth}}$  (Table 16: Signal  $S_{8y}$ ). The respective  $\Delta M_{\text{rel}}$  relative mean anomaly migration values are  $0.013$  and  $0.021$  during one revolution of Earth. Hence, these true anomaly  $\nu_{\min}$  and  $\nu_{\max}$  values of Earth migrate about  $3.7$  and  $5.7$  revolutions during 274 years (Figure 12b: red and blue highlighted circles).

For the three symmetric pure sine models, the true anomaly  $\nu_{\min}$  and  $\nu_{\max}$  lines show the overlapping effect, because  $8 \times P_{\text{Earth}}$  in an even number multiple (Figure 12b: red, green and cyan symbols). Due to the asymmetric signal  $S_{8y}$  shape of the double wave model for sample **Rmonthly**, the lines of small and large blue circles do not overlap.

The true anomaly  $\nu_{\min}$  and  $\nu_{\max}$  migration curves of Earth converge in the centre of the blue and red dotted circles at  $t_C = 1815$  years and  $\nu = 25$  degrees (Figure 12b). Due to the aforementioned double wave signal asymmetry, the line of large blue circles deviates from the converging line of small blue circles. Although the convergence point is *outside* samples **Cmonthly** and **Cyearly**, it is nicely covered by the “predictive” green and cyan symbols not highlighted with black circles. We can identify this convergence point regardless of the large true anomaly migration of the pure sine model and the double wave model for sample **Rmonthly**. This means that all four  $S_{8y}$  signals’ period ( $P$ ), primary minimum ( $t_{\min,1}$ ) and primary maximum ( $t_{\max,1}$ ) values for different samples in Table 15 can be connected to the same signal.

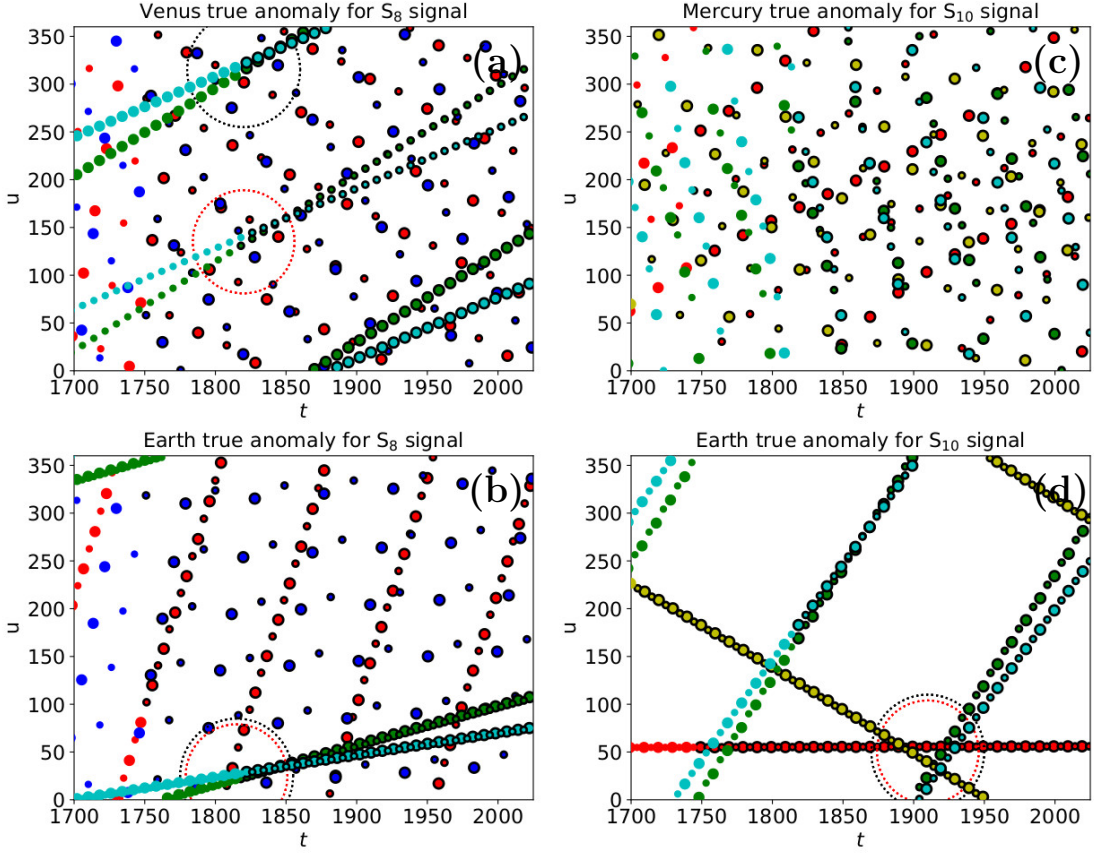


**Figure 12.** True anomalies  $\nu_{\min}$  (small circles) and  $\nu_{\max}$  (large circles) for time point multiples  $T_{\min,k}$  and  $T_{\max,k}$  (Equations 54 and 55). We compute these multiples from periods ( $P$ ), primary minimum epochs ( $t_{\min,1}$ ) and primary maximum epochs ( $t_{\max,1}$ ) given in Table 15. Symbol colours for different samples are red ( $R_{\text{monthly}}$ : pure sines), blue ( $R_{\text{monthly}}$ : double waves), green ( $C_{\text{monthly}}$ : pure sines), yellow ( $R_{\text{yearly}}$ : pure sines), and cyan ( $C_{\text{yearly}}$ : pure sines). Symbols for  $\nu_{\min}$  and  $\nu_{\max}$  values inside each sample are highlighted with a black circle. (a) Venus' true anomalies for signal  $S_{8y}$ . (b) Earth's true anomalies for signal  $S_{8y}$ . (c) Mercury's true anomalies for signal  $S_{10y}$ . (d) Earth's true anomalies for signal  $S_{10y}$ . Units of X-axis and Y-axis are years and degrees, respectively.

We detect the convergence points for the signal candidates of both Venus and the Earth. This indicates that the repetitive relative motions of these two planets may cause this  $S_{8y}$  signal.

### A.2. Signal $S_{8,y4} \cong 35 \times P_{\text{Mercury}}$

This sixth-strongest signal is detected only in sample  $R_{\text{yearly}}$  (Table 16: Signal  $S_{8,y4}$ ). The rounds value  $P = 35.158 \pm 0.066$  deviates  $\Delta P_{\text{rel}} = 2.4$  from  $35 \times P_{\text{Mercury}}$ . We want to draw attention to this  $S_{8,y4}$  signal, because the  $P = 69.57 \pm 0.11$  rounds value of another signal, the double sinusoid signal for sample  $R_{\text{monthly}}$  ( $K_2 = 2$ ), is quite close to  $2 \times 35 \times P_{\text{Mercury}}$  (Table 15: Signal  $S_{8,y4}$ ). We show no figure for this  $S_{8,y4}$  signal candidate of Mercury, because one migration line can not have a convergence point.

### A.3. Signal $S_{10^y}$

The second-strongest signal  $S_{10^y}$  period is approximately  $41.5 \times P_{\text{Mercury}}$  and  $10 \times P_{\text{Earth}}$ . The known ratio is  $10 \times P_{\text{Earth}}/P_{\text{Mercury}} = 45.528$ . Considering the statistical  $|\Delta\mathcal{P}|$  fluctuations (Equations 53 and 57), the expected migration curves of Mercury should be much messier than those of the Earth. These expectations are “amply rewarded” when Figures 12c and 12d are compared.

#### A.3.1. Signal $S_{10^y} \cong 41.5 \times P_{\text{Mercury}}$

For clarity, as well as to avoid possible misunderstandings, we define  $\mathcal{P}_0$  in Equation 51 as the integer closest to  $\mathcal{P}$ . The combined tidal forces of two planets are strongest when they are aligned to the same line with respect to the Sun. This can happen when these planets are at the same side, or at opposite sides, of the Sun. Therefore, the connection  $\mathcal{P}_0 \cong 41.5 \times P_{\text{Mercury}}$  draws our attention.

The true anomaly  $\nu_{\min}$  and  $\nu_{\max}$  migration curves for Mercury appear truly messy (Figure 12c). These true anomaly migration curves are not fully linear due to the large eccentricity of Mercury’s orbit. However, the reason for the messy impression is not eccentricity or strong migration, because even the largest relative mean anomaly migration is only  $\Delta M_{\text{rel}} = 6.2$  revolutions in a total of 851 revolutions during over two centuries (Table 16: Sample **Cmonthly**). The  $41.5 \times P_{\text{Mercury}}$  value divides all  $\nu_{\min}$  and  $\nu_{\max}$  true anomaly curves into two parts. First part contains uneven multiples of  $41.5 \times P_{\text{Mercury}}$  revolutions, and the second part contains even multiples of  $83 = 2 \times 41.5 \times P_{\text{Mercury}}$  revolutions. The true anomaly difference between these two parts is about half a revolution. This division effect causes the messy impression in Figure 12c. It would make no sense to search for a convergence point (Equation 59) from this mixture of true anomaly lines.

For one sample **Cmonthly**, this planetary signal candidate can be questioned, because the rounds  $\mathcal{P} = 41.802 \pm 0.032$  value having  $\Delta\mathcal{P}_{\text{rel}} = 9.4$  differs strongly from  $41.5 \times P_{\text{Mercury}}$  (Table 16: Signal  $S_{10^y}$ ). However, the relative rounds deviation values for the other three samples,  $0.85 \leq \Delta\mathcal{P}_{\text{rel}} \leq 2.4$ , support the  $41.5 \times P_{\text{Mercury}}$  relation. The signal detection  $\mathcal{P} = 41.529 \pm 0.034$  for sample **Rmonthly** is extremely accurate, only  $\Delta M_{\text{rel}} = 0.00070$  during one revolution of Mercury. The mean anomaly migration of the respective highlighted red circles is only 0.79 revolutions during 1137 revolutions (Figure 12c).

#### A.3.2. Signal $S_{10^y} \cong 10 \times P_{\text{Earth}}$

The relative rounds deviation  $\Delta\mathcal{P}_{\text{rel}} = 0.012, 1.5$  and  $2.3$  values of three samples support the  $10 \times P_{\text{Earth}}$  relation for  $S_{10^y}$  signal (Table 16: **Rmonthly**, **Ryearly**, **Cyearly**). For the fourth sample **Cmonthly**, the rounds  $\mathcal{P} = 10.0659 \pm 0.0077$  value has a large relative rounds deviation  $\Delta\mathcal{P}_{\text{rel}} = 8.6$ . However, the mean anomaly migration  $|\Delta M/360^\circ|$  values for all four samples are smaller than 1.3 revolutions during two, or even three, centuries.

The true anomaly  $\nu_{\min}$  and  $\nu_{\max}$  migration curves of Earth are exceptionally clear (Figure 12d). The lines of small and large circles of every sample show the overlapping effect caused by the even number  $10 \times P_{\text{Earth}}$  multiple. This overlapping effect is even more pronounced than in Figure 12b, because the results for all four samples are based on pure sine models. The true anomaly  $\nu_{\min}$  and  $\nu_{\max}$  migration convergence point of all four signals is at  $t_C = 1910$  years and  $\nu \approx M_C = 50$  degrees (Figure 12d: centre of blue and red dotted circles). This convergence point is *inside* all four samples. All these four  $S_{10^y}$  signals in different samples can undoubtedly originate from one and the same signal.

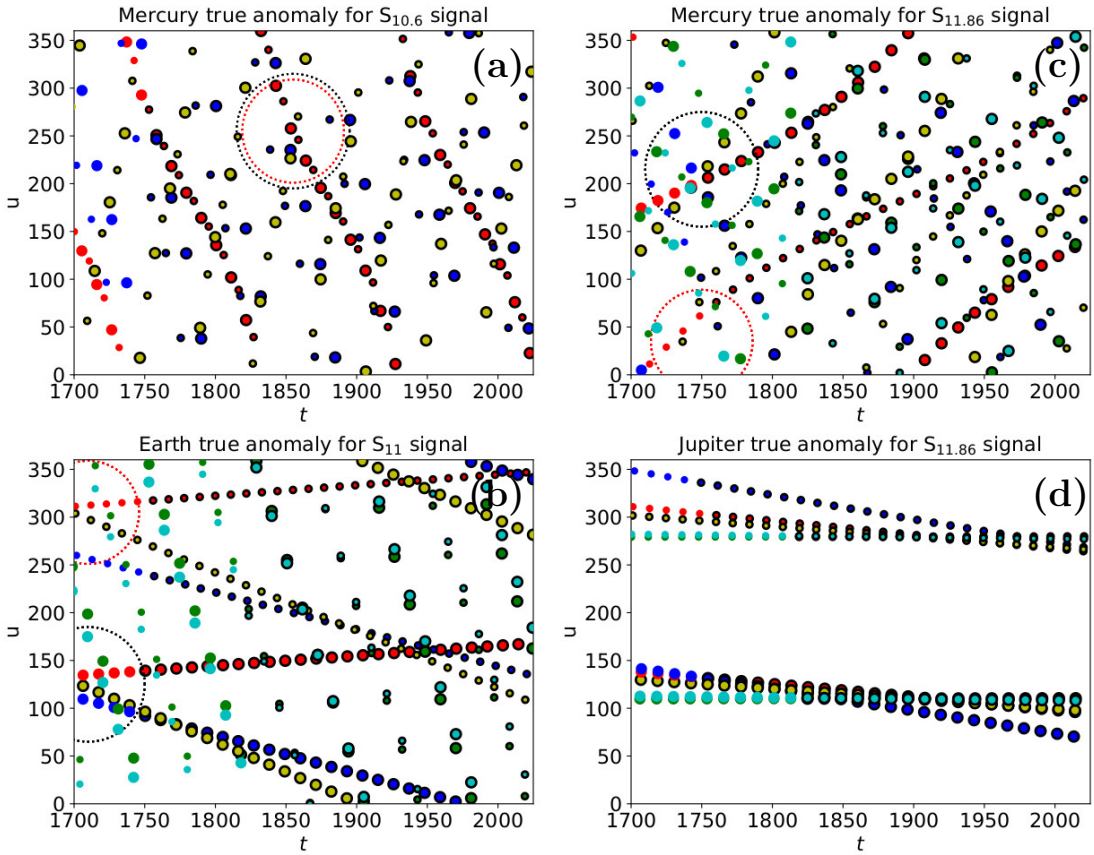


**Figure 13.** (a) Mercury's true anomalies for signal  $S_{10.6}$ . (b) Earth's true anomalies for signal  $S_{11y}$ . (c) Mercury's true anomalies for signal  $S_{11.86}$ . (d) Jupiter's true anomalies for signal  $S_{11.86}$ . Otherwise as in Figure 12.

#### A.4. Signal $S_{10.6} \cong 44 \times P_{\text{Mercury}}$

The signal  $S_{10.6}$  period is close to  $44 \times P_{\text{Mercury}} = 10.595$  years. The identification of the convergence point of this signal is quite complicated. It is not easy to perceive the correct true anomaly migration directions of the signals detected in three different samples (Figure 13a). The mean anomaly migration values  $\Delta M/360^\circ = -2.8, -5.9$  and  $7.8$  reveal that the red and the blue circles migrate downwards, and the yellow circles migrate upwards (Table 16, Signal  $S_{10.6}$ ). The large and small circles of each sample show the overlapping effect, because this signal is an even number multiple  $44 \times P_{\text{Mercury}}$ . The red and yellow circles of the symmetric pure sine model for samples  $\text{Rmonthly}$  and  $\text{Ryearly}$  follow this regularity. However, the blue small circles for the asymmetric double wave model of sample  $\text{Rmonthly}$  break this regularity. Using all the above-mentioned information, we identify the convergence points of both  $\nu_{\min}$  and  $\nu_{\max}$  true anomalies at  $t_C = 1855$  years and  $\nu \approx M_C = 255$  degrees (Figure 13a: centre of blue and red dotted lines). Due to the strong migration, the same pattern is repeated at the approximate year and degree coordinates (1760, 220) and (1940, 280).

The rounds values  $\mathcal{P} = 43.891 \pm 0.083$  and  $44.26 \pm 0.13$  differ only  $\Delta \mathcal{P}_{\text{rel}} = 1.3$  and  $2.0$  from  $44 \times P_{\text{Mercury}}$  (Table 16: Signal  $S_{10.6}$ ). The  $\mathcal{P} = 43.774 \pm 0.0824$  value for sample  $\text{Rmonthly}$  double wave model has a large  $\Delta \mathcal{P}_{\text{rel}} = 9.0$  relative rounds deviation. However, all three relative mean anomaly migration  $\Delta M_{\text{rel}}$  values  $0.0025, 0.0052$  and  $0.0059$  are nearly the same.

### A.5. Signal $S_{11y} \cong 11 \times P_{\text{Earth}}$

This strongest  $S_{11y}$  signal is close to  $11 \times P_{\text{Earth}}$ . The non-weighted DCM analysis gives the rounds values  $\mathcal{P} = 11.0033 \pm 0.0064$ ,  $10.9878 \pm 0.0051$  and  $10.981 \pm 0.021$  (Table 16: **Rmonthly**, **Ryearly**). The respective relative rounds deviation  $\Delta\mathcal{P}_{\text{rel}} = 0.52$ ,  $0.24$  and  $0.95$  values support the  $11 \times P_{\text{Earth}}$  relation. The rounds values  $\mathcal{P} = 10.8585 \pm 0.0048$  and  $10.863 \pm 0.022$  obtained from the weighted DCM analysis, however, show large  $\Delta\mathcal{P}_{\text{rel}} = 29$  and  $6.2$  relative rounds deviations (Table 16: **Cmonthly**, **Cyearly**).

The uneven  $11 \times P_{\text{Earth}}$  multiple causes the 180 degrees separation effect of the  $\nu_{\min}$  and  $\nu_{\max}$  true anomalies. Regardless of the above-mentioned large  $\Delta\mathcal{P}_{\text{rel}}$  values for samples **Cmonthly** and **Cyearly**, we obtain very convincing estimates for the convergence points of the true anomaly  $\nu_{\min}$  and  $\nu_{\max}$  migration curves (Figure 13b). The maxima converge at  $t_C = 1710$  years and  $\nu \approx M_C = 125$  degrees. Only the highlighted yellow circles of **Ryearly** reach this convergence point, because it is *outside* samples **Rmonthly**, **Cmonthly** and **Cyearly**. Yet, the large “predictive” red, blue, green and cyan circles migrate through the large dotted blue circle surrounding this convergence point (Figure 13b). The small circles show that the minima  $\nu_{\min}$  converge at  $t_C = 1710$  and  $\nu \approx M_C = 305$  degrees. The small blue circles denoting the asymmetric **Rmonthly** double wave model, represents the only migration curve that deviates from this convergence point. Both convergence points in the year 1710 are located about 50 years before the beginning of **Rmonthly** and **Cmonthly** samples (the highlighted red and blue circles) and about 100 years before the beginning of **Cmonthly** and **Cyearly** samples (the highlighted green and cyan circles). The successful convergence of the “predictive” red, blue, green and cyan circles (not highlighted with black circles) indicates that all five detected  $S_{11y}$  signals can represent one and the same real signal.

### A.6. Signal $S_{11.y86}$

The  $S_{11.y86}$  signal period is close to  $49.0 \times P_{\text{Mercury}}$  and  $1.0 \times P_{\text{Jupiter}}$ . The known period ratio is  $P_{\text{Jupiter}}/P_{\text{Mercury}} = 49.2608$ . This pair of  $S_{11.y86}$  signal multiples displays the most dramatic statistical  $|\Delta\mathcal{P}|$  fluctuation effect (Equations 53 and 57). The messy Mercury’s migration curves (Figure 13c) have exceptionally regular Jupiter’s migration curve counterparts (Figure 13d).

#### A.6.1. Signal $S_{11.y86} \cong 49.0 \times P_{\text{Mercury}}$

None of the five  $\mathcal{P}$  rounds values differs more than  $3\Delta\mathcal{P}_{\text{rel}}$  from  $49.0 \times P_{\text{Mercury}}$  (Table 16: Signal  $S_{11.y86}$ ). No other planetary signal candidate shows this degree of regularity. All relative mean anomaly migration values fulfil  $\Delta M_{\text{rel}} \leq 0.0054$ . For this particular  $\Delta M_{\text{rel}}$  parameter, this is also the best result among all planetary signal candidates. Even the largest mean anomaly migration  $\Delta M/360^\circ$  is only 4.6 revolutions during 850 revolutions of Mercury. The smallest mean anomaly migration for sample **Rmonthly** ( $K_2 = 1$ ) is only  $\Delta M/360^\circ = 0.65$  during 1137 revolutions. The twisted large and small red circle curves of this sample nicely illustrate Mercury’s orbit eccentricity effect (Figure 13c).

The uneven  $49 \times P_{\text{Mercury}}$  multiple causes the 180 degrees separation effect of  $\nu_{\min}$  and  $\nu_{\max}$  values (Figure 13c). The red, green, yellow and cyan circles of four samples show positive upwards migration. The blue circles denoting the double wave model results for sample **Rmonthly** show the only negative downwards migration. The curves of the large highlighted red and yellow circles denoting the  $\nu_{\max}$  values *inside* samples **Rmonthly** ( $K_2 = 1$ ) and **Ryearly** intersect at the convergence point  $t_C = 1750$  and  $\nu \approx M_C = 215$  degrees. The respective large “predictive” blue, green and cyan circle curves, which are *outside* samples **Rmonthly** ( $K_2 = 2$ ), **Cmonthly** and

Cyearly, also intersect at the centre of the large blue dotted circle surrounding this convergence point. The respective  $\nu_{\min}$  convergence point is at  $t_C = 1750$  and  $\nu \approx M_C = 35$  degrees. The two detected convergence points indicate that all five  $S_{11,y86}$  signals detected in different samples can represent one and the same signal.

#### A.6.2. Signal $S_{11,y86} \cong 1.0 \times P_{\text{Jupiter}}$

Three rounds  $\mathcal{P} = 1.0001 \pm 0.0018$ ,  $0.9964 \pm 0.0023$  and  $0.9995 \pm 0.0057$  values support the  $1 \times P_{\text{Jupiter}}$  relation (Table 16: Signal  $S_{11,y86}$ ). Two rounds values for Rmonthly,  $\mathcal{P} = 0.9953 \pm 0.0010$  and  $0.99224 \pm 0.00093$ , differ  $\Delta\mathcal{P}_{\text{rel}} = 4.7$  and  $8.3$  from this relation. However, all mean anomaly migration values fulfil  $|\Delta M| \leq 0.18$  revolutions.

The uneven  $1 \times P_{\text{Jupiter}}$  multiple causes the 180 degree separation effect between Jupiter's true anomaly  $\nu_{\min}$  and  $\nu_{\max}$  values (Figure 13b). All true anomaly migration curves are so regular that there is no need to search for convergence points. The small blue circles, which denote the  $\nu_{\min}$  values of the asymmetric double wave model for sample Rmonthly, show the largest deviation from the general migration trends. The regular convergence of Jupiter's true anomalies definitely indicates that one and the same signal is detected in all five different samples. The strongest amplification of the  $S_{11,y86}$  sunspot signal occurs close to true anomaly  $\nu = \nu_{\max} = 120^\circ$ . The damping of this signal occurs about 6 years ( $11.86/2$ ) later, close to true anomaly  $\nu = \nu_{\min} = 300^\circ$ .

The detection of the convergence points for the signal candidates of Mercury and Jupiter indicates that the relative motions of these two planets can cause this  $S_{11,y86}$  signal.

The maxima of all five  $S_{11,y86}$  signals in Table 16 occur between Jupiter's perihelion and aphelion, which are denoted with dotted and continuous vertical lines in Figure 14. All  $S_{11,y86}$  signal minima are between Jupiter's aphelion and perihelion. The phases of all five  $S_{11,y86}$  signals are stable, and stay in phase with Jupiter's orbital motion. The signal amplitudes in the monthly and the yearly samples are nearly the same. This  $S_{11,y86}$  signal is clearly connected to the orbital motion of Jupiter. The distance between the Sun and Jupiter modulates the number of sunspots.

All these results confirm an irrefutable deterministic connection between the sunspot cycle and Jupiter's orbital motion. If these results do not represent the *direct* detection of Jupiter from the sunspot data, then, what have we detected? It would be quite a coincidence if we had managed to formulate a flawed statistical method that would accidentally detect Jupiter's period from the sunspot data. We can ask, quite rightly, has anyone else ever made this kind of a direct detection of Jupiter from the sunspot data?

#### A.7. Signal $S_{53y} \cong 4.5P_{\text{Jupiter}}$

The two rounds  $\mathcal{P} = 4.439 \pm 0.023$  and  $4.538 \pm 0.064$  differ only  $\Delta\mathcal{P}_{\text{rel}} = 2.6$  and  $0.59$  from  $4.5 \times P_{\text{Jupiter}}$  (Table 16:  $S_{53y}$ ). We merely mention this regularity, but we do not search for converge points from the migration of only two curves.

#### A.8. Signal $S_{66y} \cong 5.5 \times P_{\text{Jupiter}}$ or $\cong 6.0 \times P_{\text{Jupiter}}$

This weakest one of all detected signals has a rounds value  $\mathcal{P} = 5.62 \pm 0.12$  (Table 16: Signal  $S_{66y}$ ). We mention this  $S_{66y}$  signal because the double sinusoid signal period  $P = 143.30 \pm 0.99$  (Table 15: Signal  $S_{66y}$ ) has a rounds value  $\mathcal{P} = 12.088 \pm 0.083$ , which is close to  $2 \times 6 \times P_{\text{Jupiter}}$ .

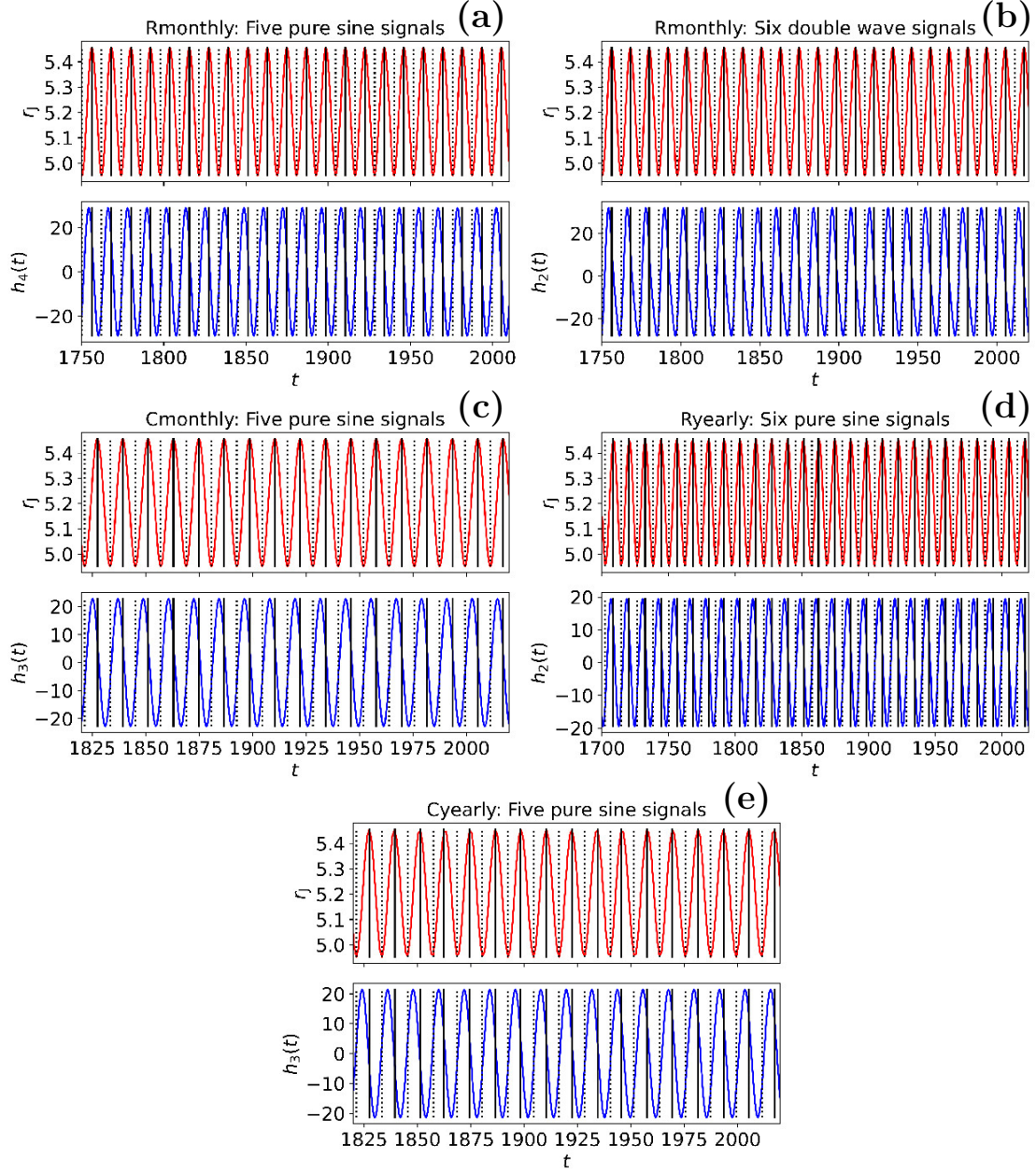


**Figure 14.** Signal S11,y86 connection to Jupiter's distance  $r_J$  from the Sun. (a) Upper panel: Red curve shows distance between the Sun and Jupiter. Aphelion and perihelion epochs are denoted with vertical black continuous and dotted lines, respectively. Units are x-axis  $[t]$  = years and y-axis  $[r_J]$  = AU. Lower panel: Blue curve shows simultaneous  $h_4(t)$  pure sine 11.807 year signal in Rmonthly (DCM-manual: Table 7). Aphelion and perihelion notations are as in upper panel. Units are x-axis  $[t]$  = years and y-axis  $[h_4(t)]$  = dimensionless. (b)  $h_2(t)$  double wave 11.770 year signal in Rmonthly (DCM-manual: Table 9). Otherwise as in “a”. (c)  $h_3(t)$  pure sine 11.863 year signal in Cmonthly (DCM-manual: Table 11). Otherwise as in “a”. (d)  $h_2(t)$  pure sine 11.826 year signal in Ryearly (DCM-manual: Table 15). Otherwise as in “a”. (e)  $h_3(t)$  pure sine 11.856 year signal in Cyearly (DCM-manual: Table 17). Otherwise as in “a”.

**Acknowledgements** We thank the Finnish Computing Competence Infrastructure (FCCI) for supporting this project with computational resources. We thank Juha Helin, Jani Jaakkola, Sami Maisala and Pasi Vettentranta who helped us utilise parallel computation resources in the High Performance Computing (HPC) platform. Veijo Niinikoski is acknowledged for pointing out that the Earth's and Jupiter's magnetic fields are much stronger than those of Venus and Mercury. We also thank Stefan Ahmala for drawing our attention to the possible electromagnetic interactions between the magnetic fields of solar system bodies. We thank professor Alexis Finoguenov for his insightful comments, as well as for recommending the use of grammar packages. This work has made use of NASA's Astrophysics Data System (ADS) services.

## B. Additional statements

**Author Contribution** L.J. analysed the data, prepared the figures and the tables, wrote the manuscript, as well as revised the manuscript.

**Data Availability** All analysed data are stored in Zenodo database <https://zenodo.org/uploads/11503698>.

**Code Availability** The Zenodo database <https://zenodo.org/uploads/11503698> also supplies our Discrete Chi-square Method (DCM) Python code. Our DCM-manual gives full instructions for repeating the DCM analysis.

## Declarations

**Conflict of interest** The author declares no competing interests.

## References

Aguilar, L.M., Robledo-Sánchez, C., Carrasco, M.L., Otero, M.M.: 2012, The principle of superposition for waves: The amplitude and phase modulation phenomena. *Applied Mathematics and Information Sciences* **6**, 307.

Akhavan-Tafti, M., Slavin, J.A., Le, G., Eastwood, J.P., Strangeway, R.J., Russell, C.T., Nakamura, R., Baumjohann, W., Torbert, R.B., Giles, B.L., Gershman, D.J., Burch, J.L.: 2018, MMS Examination of FTEs at the Earth's Subsolar Magnetopause. *Journal of Geophysical Research (Space Physics)* **123**, 1224. [DOI](#). [ADS](#).

Alfvén, H.: 1942, On the cosmogony of the solar system. *Stockholms Observatoriums Annaler* **14**, 2.1. [ADS](#).

Allen, M.P.: 2004, *Understanding Regression Analysis*, Springer US, 113. ISBN 9780306484339. [URL](#).

Asikainen, T., Mantere, J.: 2023, Prediction of even and odd sunspot cycles. *arXiv e-prints*, arXiv:2309.04208. [DOI](#). [ADS](#).

Babcock, H.W.: 1961, The Topology of the Sun's Magnetic Field and the 22-Year Cycle. *Astrophys. J.* **133**, 572. [DOI](#). [ADS](#).

Bai, T.: 1987, Distribution of Flares on the Sun: Superactive Regions and Active Zones of 1980–1985. *Astrophys. J.* **314**, 795. [DOI](#). [ADS](#).

Baliunas, S.L., Vaughan, A.H.: 1985, Stellar activity cycles. *ARA&A* **23**, 379. [DOI](#). [ADS](#).

Bhowmik, P., Jiang, J., Upton, L., Lemerle, A., Nandy, D.: 2023, Physical Models for Solar Cycle Predictions. *Space Sci. Rev.* **219**, 40. [DOI](#). [ADS](#).

Birch, M.J., Bromage, B.J.I.: 2022, Sunspot numbers and proton events in solar cycles 19 to 24. *Journal of Atmospheric and Solar-Terrestrial Physics* **236**, 105891. [DOI](#). [ADS](#).

Biswas, A., Karak, B.B., Usoskin, I., Weisshaar, E.: 2023, Long-Term Modulation of Solar Cycles. *Space Sci. Rev.* **219**, 19. [DOI](#). [ADS](#).

Breger, M., Garrido, R., Handler, G., Wood, M.A., Shobbrook, R.R., Bischof, K.M., Rodler, F., Gray, R.O., Stankov, A., Martinez, P., O'Donoghue, D., Szabó, R., Zima, W., Kaye, A.B., Barban, C., Heiter, U.: 2002, 29 frequencies for the  $\delta$  Scuti variable BI CMi: the 1997-2000 multisite campaigns. *Mon. Not. R. Astron. Soc.* **329**, 531. [DOI](#). [ADS](#).

Charbonneau, P.: 2010, Dynamo Models of the Solar Cycle. *Living Reviews in Solar Physics* **7**, 3. [DOI](#). [ADS](#).

Charbonneau, P.: 2022, External Forcing of the Solar Dynamo. *Frontiers in Astronomy and Space Sciences* **9**, 853676. [DOI](#). [ADS](#).

Cionco, R.G., Kudryavtsev, S.M., Soon, W.W.-H.: 2023, Tidal Forcing on the Sun and the 11-Year Solar-Activity Cycle. *Sol. Phys.* **298**, 70. [DOI](#). [ADS](#).

Cranmer, S.R., Saar, S.H.: 2007, Exoplanet-Induced Chromospheric Activity: Realistic Light Curves from Solar-type Magnetic Fields. *arXiv e-prints*, astro. [DOI](#). [ADS](#).

Cuntz, M., Saar, S.H., Musielak, Z.E.: 2000, On Stellar Activity Enhancement Due to Interactions with Extrasolar Giant Planets. *Astrophys. J. Lett.* **533**, L151. [DOI](#). [ADS](#).

DiBraccio, G.A., Slavin, J.A., Imber, S.M., Gershman, D.J., Raines, J.M., Jackman, C.M., Boardsen, S.A., Anderson, B.J., Korth, H., Zurbuchen, T.H., McNutt, R.L., Solomon, S.C.: 2015, MESSENGER observations of flux ropes in Mercury's magnetotail. *Planetary and Space Science* **115**, 77. [DOI](#). [ADS](#).

Dimitropoulou, M., Moussas, X., Strintzi, D.: 2008, Enhanced Rieger type periodicities' detection in X-ray solar flares and statistical validation of Rossby waves' existence. *Proceedings of the International Astronomical Union* **4**, 159–163. [DOI](#).

Draper, N.R., Smith, H.: 1998, *Applied Regression Analysis*, John Wiley & Sons, Inc. [DOI](#).

Dungey, J.W.: 1961, Interplanetary Magnetic Field and the Auroral Zones. *Phys. Rev. Lett.* **6**, 47. [DOI](#). [URL](#).

Efron, B., Tibshirani, R.: 1986, Bootstrap Methods for Standard Errors, Confidence Intervals, and Other Measures of Statistical Accuracy. *Statistical Science* **1**, 54.

Fear, R.C., Palmroth, M., Milan, S.E.: 2012, Seasonal and clock angle control of the location of flux transfer event signatures at the magnetopause. *Journal of Geophysical Research (Space Physics)* **117**, A04202. [DOI](#). [ADS](#).

Feth, L.L.: 1974, Frequency discrimination of complex periodic tones. *Perception & Psychophysics* **15**, 375.

Gillies, G.T.: 1997, The Newtonian gravitational constant: recent measurements and related studies. *Reports on Progress in Physics* **60**, 151. [DOI](#). [ADS](#).

Gleissberg, W.: 1945, Evidence for a long solar cycle. *The Observatory* **66**, 123. [ADS](#).

Glenn, G.S.: 2019, Mysterious High Energy Gamma Rays Might Help Explain What Drives Solar Cycles. *arXiv e-prints*, arXiv:1901.10574. [DOI](#). [ADS](#).

Gnevyshev, M.N., Ohl, A.I.: 1948, On the 22-year cycle of solar activity. *Astron. Zh.* **25**, 18.

Gurgenashvili, E., Zaqrashvili, T.V., Kukhianidze, V., Oliver, R., Ballester, J.L., Dikpati, M., McIntosh, S.W.: 2017, North-South Asymmetry in Rieger-type Periodicity during Solar Cycles 19-23. *Astrophys. J.* **845**, 137. [DOI](#). [ADS](#).

Hale, G.E., Ellerman, F., Nicholson, S.B., Joy, A.H.: 1919, The Magnetic Polarity of Sun-Spots. *Astrophys. J.* **49**, 153. [DOI](#). [ADS](#).

Handler, G.: 2003, Merging Data from Large and Small Telescopes – Good or Bad? And: How Useful is the Application of Statistical Weights to Time-Series Photometric Measurements? *Baltic Astronomy* **12**, 253. [DOI](#). [ADS](#).

Hansson, J.: 2022, The 11-Year Magnetic Solar Cycle: Chaos Control Due to Jupiter. *Solar System Research* **56**, 191. [DOI](#). [ADS](#).

Hantzsche, E.: 1978, On the Tidal Theory of Solar Activity. *Astronomische Nachrichten* **299**, 259. [DOI](#). [ADS](#).

Hasegawa, H., Sonnerup, B.U.Ö., Eriksson, S., Nakamura, T.K.M., Kawano, H.: 2015, Dual-spacecraft reconstruction of a three-dimensional magnetic flux rope at the Earth's magnetopause. *Annales Geophysicae* **33**, 169. [DOI](#). [ADS](#).

Horne, J.H., Baliunas, S.L.: 1986, A Prescription for Period Analysis of Unevenly Sampled Time Series. *Astrophys. J.* **302**, 757. [DOI](#). [ADS](#).

Ip, W.-H., Kopp, A., Hu, J.-H.: 2004, On the Star-Magnetosphere Interaction of Close-in Exoplanets. *Astrophys. J. Lett.* **602**, L53. [DOI](#). [ADS](#).

Javaraiah, J.: 2023, Prediction for the amplitude and second maximum of Solar Cycle 25 and a comparison of the predictions based on strength of polar magnetic field and low-latitude sunspot area. *Mon. Not. R. Astron. Soc.* **520**, 5586. [DOI](#). [ADS](#).

Jayalekshmi, G.L., Pant, T.K., Prince, P.R.: 2022, Sunspot-Cycle Evolution of Major Periodicities of Solar Activity. *Sol. Phys.* **297**, 85. [DOI](#). [ADS](#).

Jenkins, J.M., Twicken, J.D., Batalha, N.M., Caldwell, D.A., Cochran, W.D., Endl, M., Latham, D.W., Esquerdo, G.A., Seader, S., Bieryla, A., Petigura, E., Ciardi, D.R., Marcy, G.W., Isaacson, H., Huber, D., Rowe, J.F., Torres, G., Bryson, S.T., Buchhave, L., Ramirez, I., Wolfgang, A., Li, J., Campbell, J.R., Tenenbaum, P., Sanderfer, D., Henze, C.E., Catanzarite, J.H., Gilliland, R.L., Borucki, W.J.: 2015, Discovery and Validation of Kepler-452b: A 1.6  $R_{\oplus}$  Super Earth Exoplanet in the Habitable Zone of a G2 Star. *Astron. J.* **150**, 56. [DOI](#). [ADS](#).

Jephcoat, A., Olson, P.: 1987, Is the inner core of the Earth pure iron? *Nature* **325**, 332. [DOI](#). [ADS](#).

Jetsu, L.: 2020, Discrete Chi-square Method for Detecting Many Signals. *The Open Journal of Astrophysics* **3**, 4. [DOI](#). [ADS](#).

Jetsu, L.: 2021, Say Hello to Algol's New Companion Candidates. *Astrophys. J.* **920**, 137. [DOI](#). [ADS](#).

Jetsu, L., Pelt, J.: 1999, Three stage period analysis and complementary methods. *Astron. Astrophys. Suppl.* **139**, 629. [DOI](#). [ADS](#).

Jetsu, L., Pohjolainen, S., Pelt, J., Tuominen, I.: 1997, Is the longitudinal distribution of solar flares nonuniform? *Astron. Astrophys.* **318**, 293. [ADS](#).

Khomenko, E., Vitas, N., Collados, M., de Vicente, A.: 2017, Numerical simulations of quiet Sun magnetic fields seeded by the Biermann battery. *Astron. Astrophys.* **604**, A66. [DOI](#). [ADS](#).

Kivelson, M.G., Bagenal, F.: 2007, Planetary Magnetospheres. In: McFadden, L.-A.A., Weissman, P.R., Johnson, T.V. (eds.) *Encyclopedia of the Solar System*, 519. [DOI](#). [ADS](#).

Komitov, B., Kaftan, V.: 2004, The Sunspot Activity in the Last Two Millenia on the Basis of Indirect and Instrumental Indexes: Time Series Models and Their Extrapolations for the 21st Century. In: Stepanov, A.V.,

Benevolenskaya, E.E., Kosovichev, A.G. (eds.) *Multi-Wavelength Investigations of Solar Activity* **223**, 113. [DOI](#). [ADS](#).

Korhonen, H., Andersen, J.M., Piskunov, N., Hackman, T., Juncker, D., Järvinen, S.P., Jørgensen, U.G.: 2015, Stellar activity as noise in exoplanet detection - I. Methods and application to solar-like stars and activity cycles. *Mon. Not. R. Astron. Soc.* **448**, 3038. [DOI](#). [ADS](#).

Krasheninnikov, I.V., Chumakov, S.O.: 2023, Predicting the Functional Dependence of the Sunspot Number in the Solar Activity Cycle Based on Elman Artificial Neural Network. *Geomagnetism and Aeronomy* **63**, 215. [DOI](#). [ADS](#).

Ku, J.G., Liu, X.Y., Chen, H.H., Deng, R.D., Yan, Q.X.: 2016, Interaction between two magnetic dipoles in a uniform magnetic field. *AIP Advances* **6**, 025004. [DOI](#). [URL](#).

Lassen, K., Friis-Christensen, E.: 1995, Variability of the solar cycle length during the past five centuries and the apparent association with terrestrial climate. *Journal of Atmospheric and Terrestrial Physics* **57**, 835. [DOI](#). [ADS](#).

Lehtinen, J., Jetsu, L., Hackman, T., Kajatkari, P., Henry, G.W.: 2011, The continuous period search method and its application to the young solar analogue HD 116956. *Astron. Astrophys.* **527**, A136. [DOI](#). [ADS](#).

Leighton, R.B.: 1969, A Magneto-Kinematic Model of the Solar Cycle. *Astrophys. J.* **156**, 1. [DOI](#). [ADS](#).

Li, J.: 2018, A Systematic Study of Hale and Anti-Hale Sunspot Physical Parameters. *Astrophys. J.* **867**, 89. [DOI](#). [ADS](#).

Lockwood, M., Wild, M.N.: 1993, On the quasi-periodic nature of magnetopause flux transfer events. *J. Geophys. Res.* **98**, 5935. [DOI](#). [ADS](#).

Loumos, G.L., Deeming, T.J.: 1978, Spurious results from Fourier analysis of data with closely spaced frequencies. *Astrophys. Space Sci.* **56**, 285. [DOI](#). [ADS](#).

Luminița, D., Laurențiu, N.E., Constantina, F.: 2023, The use of Ap geomagnetic indices for the characterization and ranking of major geomagnetic disturbances from 1932 to 2022. *Oltenia, Studii si Comunicari Seria Stiintele Naturii* **39**.

Macdonald, L.: 2012, *How to Observe the Sun Safely*. [DOI](#). [ADS](#).

Muñoz, J.M., Wagemakers, A., Sanjuán, M.A.F.: 2023, Planetary influences on the solar cycle: A nonlinear dynamics approach. *Chaos* **33**, 123102. [DOI](#). [ADS](#).

Murphy, S.J.: 2012, Kepler Fourier concepts: The performance of the Kepler data pipeline. *Astronomische Nachrichten* **333**, 1057. [DOI](#). [ADS](#).

Nakariakov, V.M., Pilipenko, V., Heilig, B., Jelínek, P., Karlický, M., Klimushkin, D.Y., Kolotkov, D.Y., Lee, D.-H., Nisticò, G., Van Doorsselaere, T., Verth, G., Zimovets, I.V.: 2016, Magnetohydrodynamic Oscillations in the Solar Corona and Earth's Magnetosphere: Towards Consolidated Understanding. *Space Sci. Rev.* **200**, 75. [DOI](#). [ADS](#).

Ohtomo, N., Terachi, S., Tanaka, Y., Tokiwa, K., Kaneko, N.: 1994, New Method of Time Series Analysis and Its Application to Wolf's Sunspot Number Data. *Japanese Journal of Applied Physics* **33**, 2821. [DOI](#). [ADS](#).

Parker, E.N.: 1955, Hydromagnetic Dynamo Models. *Astrophys. J.* **122**, 293. [DOI](#). [ADS](#).

Parker, E.N.: 1958, Dynamics of the Interplanetary Gas and Magnetic Fields. *Astrophys. J.* **128**, 664. [DOI](#). [ADS](#).

Paul, A., Vaidya, B., Strugarek, A.: 2022, A Volumetric Study of Flux Transfer Events at the Dayside Magnetopause. *Astrophys. J.* **938**, 130. [DOI](#). [ADS](#).

Pease, G.E., Glenn, G.S.: 2016, Long Term Sunspot Cycle Phase Coherence with Periodic Phase Disruptions. *arXiv e-prints*, arXiv:1610.03553. [DOI](#). [ADS](#).

Petrovay, K.: 2020, Solar cycle prediction. *Living Reviews in Solar Physics* **17**, 2. [DOI](#). [ADS](#).

Phan, T.-D., Paschmann, G., Baumjohann, W., Sckopke, N., Luehr, H.: 1994, The magnetosheath region adjacent to the dayside magnetopause: AMPTE/IRM observations. *J. Geophys. Res.* **99**, 121. [DOI](#). [ADS](#).

Raeder, J.: 2006, Flux Transfer Events: 1. generation mechanism for strong southward IMF. *Annales Geophysicae* **24**, 381. [DOI](#). [ADS](#).

Reegen, P.: 2007, SigSpec. I. Frequency- and phase-resolved significance in Fourier space. *Astron. Astrophys.* **467**, 1353. [DOI](#). [ADS](#).

Rieger, E., Kanbach, G., Reppin, C., Share, G.H., Forrest, D.J., Chupp, E.L.: 1984, A 154-day periodicity in the occurrence of hard solar flares? *Nature* **312**, 623. [DOI](#). [ADS](#).

Rijnbeek, R.P., Cowley, S.W.H., Southwood, D.J., Russell, C.T.: 1984, A survey of dayside transfer events observed by ISEE 1 and 2 magnetometers. *J. Geophys. Res.* **89**, 786. [DOI](#). [ADS](#).

Rodríguez, E., Costa, V., Handler, G., García, J.M.: 2003, Simultaneous uvby photometry of the new delta Sct-type variable HD 205. *Astron. Astrophys.* **399**, 253. [DOI](#). [ADS](#).

Russell, C.T.: 1995, A study of flux transfer events at different planets. *Advances in Space Research* **16**, 159. [DOI](#). [ADS](#).

Russell, C.T.: 2003, The structure of the magnetopause. *Planetary and Space Science* **51**, 731. [DOI](#). [ADS](#).

Rutkowski, L.: 2014, Symmetry and asymmetry as a physical and perceptual feature of the complementary pair of bearing sinusoids. Part I. Amplitude and frequency envelope relations. *Archives of Acoustics* **23**, 51.

Sarkango, Y., Slavin, J.A., Jia, X., DiBraccio, G.A., Gershman, D.J., Connerney, J.E.P., Kurth, W.S., Hospodarsky, G.B.: 2021, Juno Observations of Ion-Inertial Scale Flux Ropes in the Jovian Magnetotail. *Geophys. Res. Lett.* **48**, e89721. [DOI](#). [ADS](#).

Sarkango, Y., Slavin, J.A., Jia, X., DiBraccio, G.A., Clark, G.B., Sun, W., Mauk, B.H., Kurth, W.S., Hospodarsky, G.B.: 2022, Properties of Ion-Inertial Scale Plasmoids Observed by the Juno Spacecraft in the Jovian Magnetotail. *Journal of Geophysical Research (Space Physics)* **127**, e30181. [DOI](#) [ADS](#).

Scafetta, N., Bianchini, A.: 2022, The Planetary Theory of Solar Activity Variability: A Review. *Frontiers in Astronomy and Space Sciences* **9**, 937930. [DOI](#) [ADS](#).

Scargle, J.D.: 1982, Studies in astronomical time series analysis. II - Statistical aspects of spectral analysis of unevenly spaced data. *Astrophys. J.* **263**, 835. [DOI](#) [ADS](#).

Schubert, G., Soderlund, K.M.: 2011, Planetary magnetic fields: Observations and models. *Physics of the Earth and Planetary Interiors* **187**, 92. [DOI](#) [ADS](#).

Schuster, A.: 1911, The Influence of Planets on the Formation of Sun-Spots. *Proceedings of the Royal Society of London Series A* **85**, 309. [DOI](#) [ADS](#).

Schwabe, M.: 1844, Sonnenbeobachtungen im Jahre 1843. Von Herrn Hofrat Schwabe in Dessau. *Astronomische Nachrichten* **21**, 233. [ADS](#).

Schwär, S., Müller, M., Schlecht, S.: 2023, Modifying Partials for Minimum-Roughness Sound Synthesis. In: *Proceedings of Timbre 2023, 3rd International Conference on Timbre, Thessaloniki, Greece*, 1.

Scurry, L., Russell, C.T., Gosling, J.T.: 1994, A statistical study of accelerated flow events at the dayside magnetopause. *J. Geophys. Res.* **99**, 14,815. [DOI](#) [ADS](#).

Slavin, J.A., Lepping, R.P., Wu, C.-C., Anderson, B.J., Baker, D.N., Benna, M., Boardsen, S.A., Killen, R.M., Korth, H., Krimigis, S.M., McClintock, W.E., McNutt, R.L., Sarantos, M., Schriver, D., Solomon, S.C., Trávníček, P., Zurbuchen, T.H.: 2010, MESSENGER observations of large flux transfer events at Mercury. *Geophys. Res. Lett.* **37**, L02105. [DOI](#) [ADS](#).

Slavin, J.A., Anderson, B.J., Baker, D.N., Benna, M., Boardsen, S.A., Gold, R.E., Ho, G.C., Imber, S.M., Korth, H., Krimigis, S.M., McNutt, J., Ralph L., Raines, J.M., Sarantos, M., Schriver, D., Solomon, S.C., Trávníček, P., Zurbuchen, T.H.: 2012, MESSENGER and Mariner 10 flyby observations of magnetotail structure and dynamics at Mercury. *Journal of Geophysical Research (Space Physics)* **117**, A01215. [DOI](#) [ADS](#).

Stefani, F., Giesecke, A., Weier, T.: 2019, A Model of a Tidally Synchronized Solar Dynamo. *Sol. Phys.* **294**, 60. [DOI](#) [ADS](#).

Sun, W., Slavin, J.A., Nakamura, R., Heyner, D., Trattner, K.J., Mieth, J.Z.D., Zhao, J., Zong, Q.-G., Aizawa, S., Andre, N., Saito, Y.: 2022, Dayside magnetopause reconnection and flux transfer events under radial interplanetary magnetic field (IMF): BepiColombo Earth-flyby observations. *Annales Geophysicae* **40**, 217. [DOI](#) [ADS](#).

Tzeferacos, P., Rigby, A., Bott, A.F.A., Bell, A.R., Bingham, R., Casner, A., Cattaneo, F., Churazov, E.M., Emig, J., Fiuzza, F., Forest, C.B., Foster, J., Graziani, C., Katz, J., Koenig, M., Li, C.-K., Meinecke, J., Petrasso, R., Park, H.-S., Remington, B.A., Ross, J.S., Ryu, D., Ryutov, D., White, T.G., Reville, B., Miniati, F., Schekochihin, A.A., Lamb, D.Q., Froula, D.H., Gregori, G.: 2018, Laboratory evidence of dynamo amplification of magnetic fields in a turbulent plasma. *Nature Communications* **9**, 591. [DOI](#) [ADS](#).

Usoskin, I.G., Solanki, S.K., Kovaltsov, G.A.: 2007, Grand minima and maxima of solar activity: new observational constraints. *Astron. Astrophys.* **471**, 301. [DOI](#) [ADS](#).

Van Geel, B., Raspovov, O., Renssen, H., Van der Plicht, J., Dergachev, V., Meijer, H.: 1999, The role of solar forcing upon climate change. *Quaternary Science Reviews* **18**, 331.

Vasil, G., Lecoanet, D., Augustson, K., Burns, K., Oishi, J., Brown, B., Brummell, N., Julien, K.: 2024, The solar dynamo begins near the surface. *Nature* **629**, 769. [DOI](#).

Vaughan, S.: 2005, A simple test for periodic signals in red noise. *Astron. Astrophys.* **431**, 391. [DOI](#) [ADS](#).

Vogt, M.F., Jackman, C.M., Slavin, J.A., Bunce, E.J., Cowley, S.W.H., Kivelson, M.G., Khurana, K.K.: 2014, Structure and statistical properties of plasmoids in Jupiter's magnetotail. *Journal of Geophysical Research (Space Physics)* **119**, 821. [DOI](#) [ADS](#).

Wagner, G., Beer, J., Masarik, J., Muscheler, R., Kubik, P.W., Mende, W., Laj, C., Raisbeck, G.M., Yiou, F.: 2001, Presence of the Solar de Vries Cycle ( $\sim$ 205 years) during the Last Ice Age. *Geophys. Res. Lett.* **28**, 303. [DOI](#) [ADS](#).

Weisshaar, E., Cameron, R.H., Schüssler, M.: 2023, No evidence for synchronization of the solar cycle by a "clock". *Astron. Astrophys.* **671**, A87. [DOI](#) [ADS](#).

Wolf, R.: 1852, Bericht über neue Untersuchungen über die Periode der Sonnenflecken und ihrer Bedeutung von Herrn Prof. Wolf. *Astronomische Nachrichten* **35**, 369. [DOI](#) [ADS](#).

Wolf, R.: 1859, Extract of a Letter to Mr. Carrington. *Mon. Not. R. Astron. Soc.* **19**, 85. [DOI](#) [ADS](#).

Xiang, N.B., Ning, Z.J., Li, F.Y.: 2020, Temporal Evolution of the Rotation of the Interplanetary Magnetic Field  $B_X$ ,  $B_y$ , and  $B_z$  Components. *Astrophys. J.* **896**, 12. [DOI](#) [ADS](#).

Zhang, H., Zong, Q., Connor, H., Delamere, P., Fácskó, G., Han, D., Hasegawa, H., Kallio, E., Kis, Á., Le, G., Lembége, B., Lin, Y., Liu, T., Oksavik, K., Omidi, N., Otto, A., Ren, J., Shi, Q., Sibeck, D., Yao, S.: 2022, Dayside Transient Phenomena and Their Impact on the Magnetosphere and Ionosphere. *Space Sci. Rev.* **218**, 40. [DOI](#) [ADS](#).

Zhu, F.R., Jia, H.Y.: 2018, Lomb-Scargle periodogram analysis of the periods around 5.5 year and 11 year in the international sunspot numbers. *Astrophys. Space Sci.* **363**, 138. [DOI](#) [ADS](#).